

# Study of $\Lambda$ hyperon production in C+C collisions at 2 AGeV beam energy with the HADES spectrometer

Kalliopi Kanaki

März 2007

Wissenschaftlich-Technische Berichte  
**FZD-467**  
März 2007

Kalliopi Kanaki

**Study of  $\Lambda$  hyperon production  
in C+C collisions at 2 AGeV beam energy  
with the HADES spectrometer**



**Forschungszentrum  
Dresden** Rossendorf

Institut für Kern- und Teilchenphysik  
Fakultät Mathematik und Naturwissenschaften  
Technische Universität Dresden

**Study of  $\Lambda$  hyperon production  
in C+C collisions at 2 AGeV beam energy  
with the HADES spectrometer**

Dissertation  
zur Erlangung des  
akademischen Grades

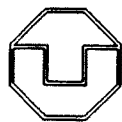
Dr. rer. nat.

vorgelegt von

Kalliopi Kanaki

geboren in Athen, Griechenland

Dresden 2007





eingereicht am 15.08.2006

1. Gutachter : Prof. Dr. Eckart Grosse
2. Gutachter : Prof. Dr. Wolfgang Enhardt
3. Gutachter : Prof. Dr. Norbert Herrmann

verteidigt am 17.01.2007

ΠΕΡΚΡΟΣ: ... ες γην ενδικαν Κύπρον ου μ' εὐεστισεν

οικειν Απολλων, δυνατα νησιωτικόν

Σαλαμίνα θέμενον της εκει χάρην πάτρας.

ΕΛΕΝΗ: Ουκ ἔστιν ες γην Τρωάδ' , ἀλλ' εἰδῶλον ἦν.

ΑΙΤΕΛΟΣ: Τι φης;

Νεφέλης ἀφ' ἁλλῶς εἶχονεν πόλους πέρι;

ΕΥΡΥΠΙΔΗΣ, ΕΛΕΝΗ

“Τ’ ἀρόνια δεν σ’ ἀρήνοννε να κοιμηθεις στις Πλάτες”.

Αρόνι ντροπαλό, μες στον ανασασμό των γυλιών

ού που θωπίζεις τη μουσική θρονα του δάσους

στα χωριότητα σάματα και στις ψυχές

αυτῶν που ἔφρουν πως δε να γυρίσων.

Τυράη φωνή, που ψηλάχρες μεσα στη νυχτωμένη μνήμη

βήματα και χερσονομιές. δε να τομάσῃσῃ να πω γιάνηματα

και το πικρό ερικυμπίσμα της ἔαγρειμένης σκαλάδας.

“Τ’ ἀρόνια δεν σ’ ἀρήνοννε να κοιμηθεις στις Πλάτες”.

Ποιες είναι οι Πλάτες; Ποιος το γωρίζει τόστο το νησι;

Εἴησα τη ζωή μου ακούγοντας ονόματα πωτάκονοστα:

καινούργιους τόπους, καινούργιες τρέδες των ανιρώπων

ἢ των θείων.

ἢ μοῖρα μου που κτυπιτίζει

ανήμερα στο στερνό σπασί ενός Αἰντα

και μιαν ἄλλη Σαλαμίνα

ἢ ἔφερε εἰς σ’ αὐτό το γυρογιάι.

Το γεγάρι

βγήκε απ’ το πέλαγο σαν Ἀφροδίτη.

σέπασε τ’ ἄστρα του Τροῶδ’ , τώρα πάλι να βρει

την καρδιά του Σχορπιοῦ, κι ὅλα τ’ ἀλάξει.

Πού είναι ἡ ἀλήθεια;

Ἦσουν κι ἐγώ στον πόλεμο τῶζότ’;

το βιζικό μου ενός ανιρώπου που ἔσπτόχησε.

Αρόνι ποιητάρη,

σαν και μια τέτοια νύχτα στ’ ακροθαλάσσι του Πρωτέα

σ’ ἀκουσαν οι σκαλάδες Σπαρτιάτισσες κι ἔσπραν το βήνο.

κι ἀνήμερό τους - ποιος να το ἄγει - ἢ Ελένη;

Ἦταν εκει, στα χεῖρα της ερῆνον. τὴν ἀγγίζα, μου μίλαρε:

“Δεν είν’ αλήθεια, δεν είν’ αλήθεια” ρώναζε.

“Δεν μπήκα στο γαλαζόπλωρο καράβι.  
Ποτέ δεν πάτησα την αντριομένη Τροία”.

Με το βαιθύ στηθόδεσμο, τον ήλιο στα μαλλιά, κι αυτό  
το ανάστημα  
ίσκιοι και χαμόγελα παντού  
στους ώμους στους μηρούς στα γόνατα  
ζωντανό δέρμα, και τα μάτια  
με τα μεγάλα βλέφαρα,  
ήταν εκεί, στην όχθη ενός Δέλτα.

Και στην Τροία;

Τίποτε στην Τροία - ένα είδωλο.  
Έτσι το θέλαν οι θεοί.  
Κι ο Πάρης, μ’ έναν ίσκιο πλάγιαζε σα να ήταν πλάσμα  
απόριο  
κι εμείς στραζόμασταν για την Ελένη δέκα χρόνια.

Μεγάλος πόνος είχε πέσει στην Ελλάδα.  
Τόσα κορμιά ριγμένα  
στα σαγόνια της θάλασσας στα σαγόνια της γης  
τόσες ψυχές  
δοσμένες στις μυλόπετρες σαν το σιτάρι.  
Κι οι ποταμοί φουσκώναν μες στη λάσπη το αίμα  
για ένα λινό κυμάτισμα για μια νεφέλη  
μιας πεταλούδας τίνιγμα το πούμπουλο ενός κύκνου  
για ένα πουκάμισο αδειανό, για μιαν Ελένη.  
Κι ο αδερφός μου;

Αηδόνι αηδόνι αηδόνι  
τ’ είναι θεός; τι μη θεός; και τι τ’ ανάμεσό τους;

“Τ’ αηδόνια δεν σ’ αφήνουνε να κοιμηθείς στις Πλάτρες”.

Δακρυσμένο πουλί.

στην Κύπρο τη θάλασσοφιλήτη  
που έταξαν για να μου θυμίζει την πατρίδα.  
άραξα μοναχός μ’ αυτό το παραμύθι,  
αν είναι αλήθεια πως αυτό είναι παραμύθι,  
αν είναι αλήθεια πως οι άνθρωποι δεν θα ξαναπιάσουν  
τον παλιό δόλο των θεών.

αν είναι αλήθεια  
πως κάποιος άλλος Τεύχος, ύστερα από χρόνια,  
ή κάποιος Αίαντας ή Πρίαμος ή Εκάβη

---

ή κάποιος άγνωστος ανώνυμος που ωστόσο  
είδε ένα Σκάμαντρο να ξεχειλάει κουράρια.  
δεν το 'χει μες στη μοίρα του ν' ακούσει  
μαντατοφόρους που έρχονται να πούνε  
πως τόσος πόνος τόση ζωή  
πήγαν στην άβυσσο  
για ένα πουκάμισο αδειανό για μιαν Ελένη.

ΕΛΕΝΗ, Γιώργος Σεφέρης (Νομπέλ Λογοτεχνίας 1963)

TEUKROS: ...zur Meeresinsel Kypros, wo Apollon mir befahl  
zu wohnen und dem Ort den Namen Salamis zu  
geben, der alten Heimat gedenkend...

HELENA: Nicht ich, mein Abbild war es, das nach Troja kam.

BOTE: Was sagst du? Für eine Wolke kämpften wir umsonst uns ab?

(EURIPIDES, HELENA 148-150;582;706)

"Auf Platres schläfst du nicht vor Nachtigallen."

Schüchterne Nachtigall im Atem der Blätter,  
du schenkst Musik und Waldesfrische allen  
in Leib und Seele Zwiegespaltenen,  
die wissen, dass sie nie heimkommen.  
Du blinde Stimme, rührst im nächtlichen Erinnern  
Gebärden, Schritte - Küsse wagte ich nicht sagen,  
und den bitteren Sturm der zornigen Sklavin auf...

"Auf Platres schläfst du nicht vor Nachtigallen."

Was ist denn Platres? Wer kennt diese Insel?  
Ich hatte so dahin gelebt,  
auf einmal neue Orte, neue Narreteien  
des Menschen und der Götter hörend.

Mein Geschick, das sich  
zwischen Aias' Schwerttod  
und einer neuen Salamis abspielte,  
hat mich hierher gebracht, in diese Bucht.

Der Mond  
stieg aus dem Meer gleich Aphrodite.  
Er schob sich vor den Bogenschützen, jetzt zieht er voran,  
das Herz des Skorpions zu finden und er verändert alles.

Wo ist die Wahrheit?  
Auch ich war Bogenschütze einst, im Krieg;  
mein Schicksal: eines Menschen, der sein Ziel verfehlte.  
Du Dichter-Nachtigall,  
in einer solchen Nacht am Strand des Proteus lauschten dir  
die Sklavinnen aus Sparta und wehklagten laut.  
Eine von ihnen war - wer sagte es - Helena!  
Wir hatten sie jahrelang im Skamandertal verfolgt,  
nun war sie da, am Rand der Wüste;  
ich legte meine Hand auf sie, sie sprach mich an:

*"Es ist nicht wahr, es ist nicht wahr", rief sie.  
 "Ich bin nicht in das Schiff mit dem quartzblauen Bug gestiegen,  
 ich habe nie den Boden Trojas, dieser Männerstadt, betreten.*

*Mit dem tiefen Schnürleib, Sonne in den Haaren,  
 und dieser Gestalt  
 Schatten und Lächeln überall  
 an Schultern Schenkeln Knien,  
 lebendige Haut - und die Augen  
 mit den üppigen Lidern,  
 da stand sie nun am Ufer eines Deltas.*

*Und in Troja?*

*Nichts in Troja - ein Trugbild.  
 So wollten es die Götter.  
 Mit einem Schatten schlief Paris wie mit einem Lebewesen;  
 und wir zerfleischten uns zehn Jahre lang für Helena.*

*Schweres Leid ist über Griechenland gekommen.  
 So viele Leichen wurden  
 ins Meer geworfen, von der Erde verschlungen  
 so viele Seelen wie Weizen  
 von Mahlsteinen zerrieben.  
 Und die Flüsse haben ihren Schlamm mit Blut gesättigt  
 für einen Leinenbausch für ein Gewölk,  
 einen Falter-Flügelschlag eine Schwanenfeder,  
 für ein bloßes Kleid, für eine Helena.  
 Und mein Bruder?*

*Nachtigall, Nachtigall, Nachtigall*

*Was ist Gott? Was ist nicht Gott? Was ist dazwischen?*

*"Auf Platres schläfst du nicht vor Nachtigallen."*

*Weinender Vogel,*

*Hier auf Zypern, meerumschlungen,  
 das mich, so wurde mir versprochen, an meine Heimat erinnern sollte,  
 hab ich geankert, ganz allein mit dieser Sage  
 - wenn es denn eine Sage ist,  
 wenn es denn stimmt, dass nun die Menschen nimmermehr  
 den alten Götter-Täuschungen verfallen,*

*wenn es stimmt,*

*dass heutzutage so ein Teukros,  
 ein Aias oder Priamos, so eine Hekabe,  
 so ein niemand, der vorzeiten*

*den Fluss gesehen hat, aus dem Gebeine ragten,  
nicht schicksalhaft den Boten lauschen muss,  
die kommen, um zu sagen  
dass so viel Leid, so viel Leben  
so abgrundtief dahingesunken ist  
für ein bloßes Kleid für eine Helena.*

*HELENA, Giorgos Seferis (Nobelpreis für Literatur 1963)*

# Contents

<b>1</b>	<b>Introduction</b> .....	<b>17</b>
<b>2</b>	<b>The HADES Spectrometer</b> .....	<b>23</b>
2.1	Aim and Requirements . . . . .	23
2.2	General Overview of the HADES Setup . . . . .	26
2.3	The Start and Veto Detectors . . . . .	27
2.4	The Ring Imaging Cherenkov Detector . . . . .	27
2.5	The Tracking System . . . . .	28
2.5.1	The Multiwire Drift Chambers . . . . .	28
2.5.2	The Superconducting Magnet . . . . .	30
2.6	The Time of Flight Walls . . . . .	30
2.7	The Pre-Shower Detector . . . . .	30
2.8	The HADES Trigger Concept . . . . .	32
2.8.1	First Level Trigger (LVL1) . . . . .	32
2.8.2	Second Level Trigger (LVL2) . . . . .	32
2.8.3	Third Level Trigger (LVL3) . . . . .	33
<b>3</b>	<b>The Multiwire Drift Chambers</b> .....	<b>35</b>
3.1	Principles of MDC Operation . . . . .	35
3.2	Gas Amplification . . . . .	36
3.3	Choice of the Gas Filling . . . . .	38
3.4	Drift Velocity . . . . .	38
3.5	Construction of the HADES third MDC Plane . . . . .	39
3.6	Mechanical Tension Force Measurements . . . . .	41
3.7	Wire Displacements due to Gravitational and Electrostatic Forces . . . . .	44
3.8	Numerical Calculation of Wire Sagittas . . . . .	46
3.9	Examination of the Wire Deflections for the MDC III . . . . .	47
3.10	Malfunction Symptoms of the MDC and Repair . . . . .	49
<b>4</b>	<b>Reconstruction of <math>\Lambda</math> Hyperons</b> .....	<b>53</b>
4.1	Properties of $\Lambda$ Hyperons . . . . .	53
4.2	Detector Acceptance and Resolution . . . . .	54
4.3	Particle Identification . . . . .	60
4.4	Particle Correlations and Signal Enhancement . . . . .	61
4.5	Signal-to-Background Studies . . . . .	64

4.6	The $\Lambda$ Signal in Real Data . . . . .	71
<b>5</b>	<b>The <math>\Lambda</math> Cross Section</b> . . . . .	<b>75</b>
5.1	Data Corrections . . . . .	75
5.2	Geometrical Acceptance and Total Reconstruction Efficiency . . . . .	76
5.3	Reconstruction Efficiency in Experiment . . . . .	78
5.4	Trigger Efficiency . . . . .	80
5.5	Minimum Bias Normalization . . . . .	81
5.6	Discussion . . . . .	82
5.6.1	Particle Ratios and Relative Strangeness Content . . . . .	82
5.6.2	Centrality Dependence . . . . .	86
5.6.3	Beam Energy Dependence . . . . .	88
<b>6</b>	<b>Summary</b> . . . . .	<b>89</b>
	<b>Appendix A Models for the Description of Heavy-ion Collision</b> . . . . .	<b>91</b>
A.1	BUU-type models . . . . .	92
A.2	QMD models . . . . .	92
	<b>Appendix B Calculation of Distance between two Trajectories</b> . . . . .	<b>95</b>
	<b>Appendix C Calculation of Distance from a Point to a Trajectory</b> . . . . .	<b>97</b>
	<b>Bibliography</b> . . . . .	<b>99</b>

# List of Figures

1.1	Schematic phase-diagram of strongly interacting matter on the $T - \mu_B$ plane . . . . .	18
1.2	Schematic illustration of the equation of state for $T=0$ . . . . .	19
1.3	Quark condensate dependence on $T$ and $\rho$ . . . . .	20
2.1	Schematic illustration of a few processes of dielectron production . .	23
2.2	Example of simulated invariant mass spectrum of $e^+e^-$ pairs for C+C	25
2.3	View of the HADES spectrometer . . . . .	26
2.4	Start and Veto detectors . . . . .	27
2.5	Schematic view of the RICH detector . . . . .	28
2.6	MDC and toroidal magnet . . . . .	29
2.7	View of the TOF system . . . . .	31
2.8	View of the Pre-Shower detector . . . . .	31
2.9	Schematic illustration of the second level trigger functions . . . . .	32
3.1	Energy loss rate in liquid (bubble chamber) H, gaseous He, C, Al, Sn and Pb . . . . .	36
3.2	Time development of an avalanche in a gaseous counter . . . . .	37
3.3	Potential distribution in an MDC drift cell . . . . .	39
3.4	Anode wires orientation . . . . .	40
3.5	Position accuracy for cathode wires . . . . .	41
3.6	Wire tension force for field and anode wires . . . . .	42
3.7	Wire tension force for cathode wires . . . . .	42
3.8	Simulations of the expected deformation of Stesalit frames due to wire tension . . . . .	43
3.9	Comparison of wire tension forces under different conditions . . . . .	43
3.10	Amplification factor of the gravitational sagitta . . . . .	45
3.11	Scheme of extrapolation of the solution . . . . .	47
3.12	Scheme of the zero search of $\Delta f$ and $\Delta f'$ . . . . .	47
3.13	Deflection of sense wires as a function of their tension . . . . .	48
3.14	Deflection of field wires as a function of their tension . . . . .	48
3.15	Deflection of cathode wires as a function of their tension . . . . .	49
3.16	Photo of a filament taken with microscope . . . . .	50
4.1	Feynman diagrams for $\Lambda$ production and decay . . . . .	54

4.2	Enumeration of the HADES sectors with corresponding momentum resolution . . . . .	55
4.3	$p_t$ vs. $y$ distributions for $p$ , $\pi^-$ and $\Lambda$ . . . . .	56
4.4	Hit distribution of reconstructed $p$ and $\pi^-$ tracks from $\Lambda$ decays in sectors 0, 2, 3 (SIM) . . . . .	57
4.5	Momentum resolution for $\pi^-$ and $p$ . . . . .	58
4.6	Secondary vertex distributions of $\Lambda$ decays in HGeant and Hydra . .	59
4.7	Distribution of velocity $\beta$ vs. momentum $p$ in real data . . . . .	60
4.8	Graphical cut efficiency for $\pi^-$ and $p$ . . . . .	61
4.9	Distribution of $p\pi^-$ invariant mass of all pair combinations for simulation and experiment . . . . .	62
4.10	Momentum distributions in simulation and experiment . . . . .	62
4.11	Opening angle distribution in simulation and experiment . . . . .	63
4.12	Variables used for the $\Lambda$ signal enhancement . . . . .	63
4.13	Distribution of the $\Lambda$ decay points . . . . .	64
4.14	Invariant mass distribution and S/B ratio as a function of the off-vertex distance . . . . .	65
4.15	Invariant mass distribution and S/B ratio as a function of $p\pi^-$ distance $d$ . . . . .	67
4.16	S/B ratio as a function of impact parameter $s$ . . . . .	68
4.17	Correlation of off-vertex distance cut with the parameters $d$ and $s$ . .	68
4.18	Invariant mass distribution and S/B ratio as a function of inner segment $\chi^2$ . . . . .	69
4.19	Invariant mass distribution and S/B ratio as a function of outer segment $\chi^2$ . . . . .	69
4.20	Invariant mass distribution and S/B ratio as a function of $\chi_{RK}^2$ . . . .	70
4.21	Simulated invariant mass distribution after application of cuts . . . .	71
4.22	Experimental invariant mass distribution without and with the enhancement cut . . . . .	72
4.23	Extraction of the experimental signal . . . . .	73
5.1	Distribution of the $z$ coordinate for $p$ and $\pi^-$ tracks . . . . .	77
5.2	Reconstruction difference for tracks . . . . .	78
5.3	Comparison of reconstruction efficiencies between simulation and experiment . . . . .	79
5.4	The Wróblewski factor $\lambda_s$ . . . . .	84
5.5	Contributions to the Wróblewski factor . . . . .	85
5.6	The $(\Lambda + \Sigma^0)/\langle\pi\rangle$ ratio as a function of $\sqrt{s}$ . . . . .	85
5.7	Measured multiplicities $\mathcal{M}$ normalized to the mean number of participants $\langle A_{part} \rangle$ as a function of $\langle A_{part} \rangle$ for $\Lambda + \Sigma^0$ and $K^+$ particles at beam kinetic energy 2 AGeV . . . . .	87
5.8	Beam energy dependence of $\mathcal{M}_{\Lambda+\Sigma^0} / \langle A_{part} \rangle$ . . . . .	88
B.1	Distance vector $\vec{w}_l$ between two lines. . . . .	95

---

C.1 Distance from a point to a line. . . . .	97
--	----

# List of Tables

2.1	Characteristic quantities of light vector meson . . . . .	24
3.1	Critical tension values for different wires of MDC III . . . . .	46
4.1	Main properties of $\Lambda$ hyperons . . . . .	54
4.2	S/B ratio and corresponding efficiency for the off-vertex distance . .	66
4.3	S/B ratio and corresponding efficiency for the $p\pi^-$ distance $d$ . . . .	67
4.4	S/B ratio and corresponding efficiency for the impact parameter $s$ . .	67
4.5	S/B ratio for the inner segment $\chi_{seg}^2$ . . . . .	69
4.6	S/B ratio for the outer segment $\chi_{seg}^2$ . . . . .	70
4.7	S/B ratio and corresponding efficiency for $\chi_{RK}^2$ . . . . .	70
4.8	Summary of enhancement conditions applied in simulation and ex- perimental data . . . . .	72
5.1	Geometrical acceptance and efficiencies at different stages of the anal- ysis for different temperatures . . . . .	76
5.2	Adjusted simulation cuts for the experimental data correction . . . .	78
5.3	Comparison of tracking efficiencies between simulation and experiment	79
5.4	LVL1 trigger effect on the number of reconstructed $\Lambda$ . . . . .	80
5.5	LVL1 trigger effect on $\pi^+$ . . . . .	81
5.6	Particle ratios in experiment and UrQMD . . . . .	83

# Abstract

The HADES spectrometer is a high resolution detector installed at the SIS/GSI, Darmstadt. It was primarily designed for studying dielectron decay channels of vector mesons. However, its high accuracy capabilities make it an attractive tool for investigating other rare probes at these beam energies, like strange baryons. Development and investigation of Multiwire Drift Chambers for high spatial resolution have been provided. One of the early experimental runs of HADES was analyzed and the  $\Lambda$  hyperon signal was successfully reconstructed for the first time in C+C collisions at 2 AGeV beam kinetic energy. The total  $\Lambda$  production cross section is contrasted with expectations from simulations and compared with measurements of the  $\Lambda$  yield in heavier systems at the same energy. In addition, the result is considered in the context of strangeness balance and the relative strangeness content of the reaction products is determined.

Beim HADES-Spektrometer handelt es sich um ein hochauflösendes Spektrometer, welches am SIS an der GSI, Darmstadt installiert wurde. Es wurde in erster Linie zur Untersuchung von dielektronischen Zerfällen von Vektormesonen entwickelt. Seine hohe Genauigkeit macht es jedoch bei diesen Energien auch zur Untersuchung anderer seltener Sonden wie z. B. seltsamer Baryonen attraktiv. In dieser Arbeit wird die Entwicklung und Untersuchung von Vieldrahtdriftkammern mit hoher Ortsauflösung vorgestellt und eines der frühen Experimente von HADES analysiert. Dabei wird das  $\Lambda$  Hyperon Signal zum ersten Mal für C+C Stöße bei einer Energie von 2 AGeV erfolgreich rekonstruiert. Der experimentell ermittelte totale Wirkungsquerschnitt für die Erzeugung von  $\Lambda$  Hyperonen wird dem Ergebnis von Simulationen gegenübergestellt und mit Messungen der  $\Lambda$ -Ausbeute in schwereren Systemen bei derselben Energie verglichen. Darüber hinaus wird das Ergebnis im Kontext der Erhaltung der Quantenzahl der Seltsamkeit diskutiert und der relative Gehalt seltsamer Quarks in den Reaktionsprodukten bestimmt.

# 1 Introduction

A major topic of contemporary fundamental physics research is the study of the first moments of the universe after the Big Bang, the processes and the environment that determined the context for the creation of matter with the characteristics observed today. Valuable information has been collected through astrophysical observations over the past decades (see e. g. [Mao91, Fei04, Pie05, Vau04]). But in order to acquire a more elaborate picture, it is of great importance to comprehend the dynamics of astrophysical objects [Web06a, Web06b, Web01] and to obtain insight into the chain of processes that gave the structure and objects of the cosmos their current shape.

For this purpose, the matter conditions at the outburst of the universe need to be reproduced in the controlled environment of a scientific laboratory. The means to create such hot and/or dense nuclear matter is to use heavy-ion collisions induced by accelerators of different projectiles and kinetic energies, covering thus a wide range of temperatures  $T$  and densities  $\rho$ . The collision systems and the energies are selected in such a way that the achieved states correspond, e. g. to the conditions of a certain stage in the evolution of the matter creation after Big Bang or represent the state of matter inside a star.

Key questions related to this sort of investigations have been the existence of new phases of nuclear matter, the description of the latter with an equation of state (EOS), as well as the appearance of in-medium effects that manifest in the change of hadron properties in a strongly interacting environment. The answers to the above questions will set under test the predictions of the fundamental theory of strong interactions, quantum chromodynamics (QCD).

QCD attempts to describe nuclear matter as the interaction of quarks through the exchange of colour force carriers called gluons. It leads to the conclusion that isolated single free quarks or gluons cannot be observed. Quarks and gluons appear only in colourless hadronic bound states, such as baryons and mesons. This expectation is enclosed in the notion "confinement". The situation changes at very high densities and temperatures ( $\rho \geq 5\rho_0^*$  or  $T \geq 170 \text{ MeV}$ ), where one expects the transition of nuclear matter to the quark-gluon plasma, a state at which quarks and gluons become deconfined.

The various states of matter that can be accessed with proper selection of collision system and energy are schematically illustrated in Fig. 1.1. The baryonic chemical potential  $\mu_B$  is a measure of the antimatter-matter balance and is related to the

---

\* $\rho_0 = 0.17 \text{ fm}^{-3}$  is the saturation density of symmetric nuclear matter.

density  $\rho$ ; the lower it is, the more antimatter is produced. The cross-hatched area indicates where the transition from confined to deconfined strongly interacting matter is expected, with the dashed curve representing a possible phase border line. At SIS<sup>†</sup> energies, i. e. from a few hundred MeV until 2 AGeV for heavy ions, the chemical and thermal freeze-out curves merge [Bra00]. The corresponding matter state is clearly within the confinement region. In this energy regime, the achieved states of strongly interacting matter consist of nucleons, which are excited into baryonic resonance states (e. g.  $\Delta$  and  $N^*$ ) to a substantial fraction, along with accompanying meson production, mainly pions. The corresponding region in the phase diagram is therefore often referred to as region of hadronic resonance matter. The importance of studying hadronic matter is evident, as it is the final state before freeze-out of resonance matter and any possibly produced quark-gluon plasma state.

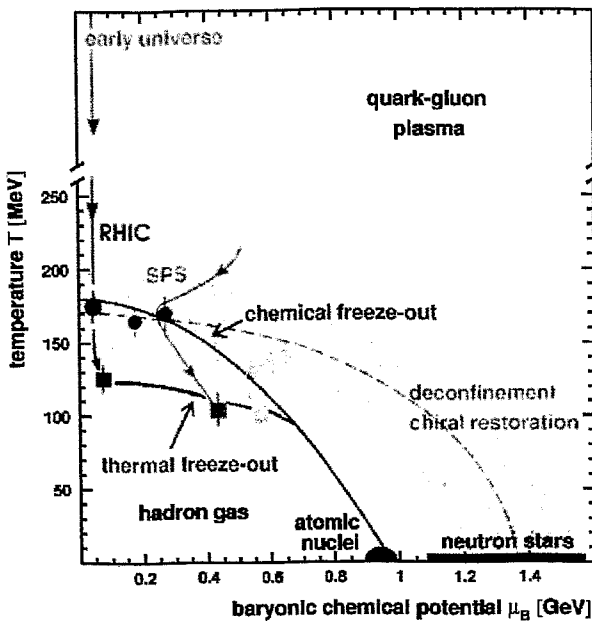


Figure 1.1: Schematic phase-diagram of strongly interacting matter on the  $T - \mu_B$  plane. Depicted are lines of chemical and thermal (kinetic) freeze-out [Bra02] within the framework of a statistical model, together with corresponding results from various collision energies available at existing accelerators [Bra95, Bra96, Bra98, Bra99, Bra02]. The chemical freeze-out parameters are deduced from hadron yields, while the thermal freeze-out parameters result from analysis of transverse momentum spectra. The cross-hatched area indicates the region of the onset of deconfinement and chiral symmetry restoration.

An important characteristic of strongly interacting matter is the equation of state [Stö86]. In case of an achieved equilibrium during a heavy-ion collision, the system can be described by a relation between three thermodynamic variables like energy  $E$ , temperature  $T$  and density  $\rho$ . One way to sketch such a dependence is depicted in Fig. 1.2. In the centre-of-mass system of the reaction there is a certain amount of internal energy available  $E_{cm}$ . This amount of energy can be split in two components, a thermal one  $E_{th}$  that is used for thermal excitations and particle production, and a part  $E_c$  that is needed to compress the system:

$$E(\rho, T) = E_{th}(\rho, T) + E_c(\rho, T = 0) + E_0, \quad (1.1)$$

where the compression component is defined at zero temperature and  $E_0$  is the ground state energy. From Fig. 1.2 it is becoming obvious that the shape of the curve

<sup>†</sup>Schwer-Ionen Synchrotron

determines how much energy is used for compressing the nuclei and how much is transformed to particle production. The amount of energy required to compress the

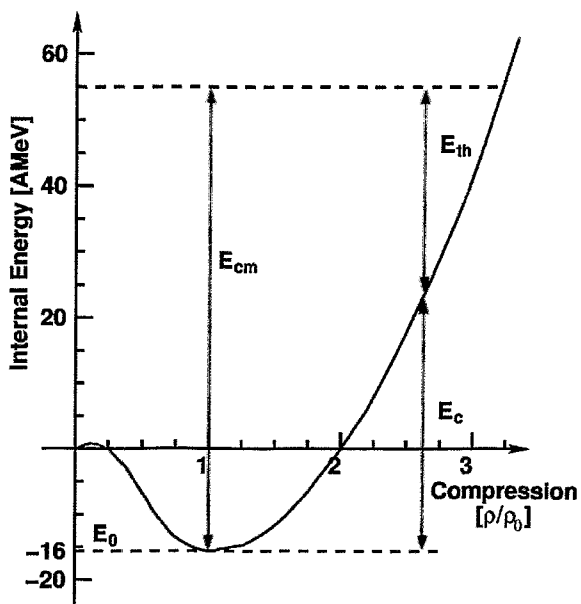


Figure 1.2: Schematic illustration of the equation of state for  $T = 0$ . In a collision with available energy  $E_{cm}$ , the curve shows how this amount can be distributed to thermal and compression components. The figure is taken from [Mer04].

system is determined by the incompressibility  $K_\infty$  and is defined as

$$K_\infty = 9\rho_0^2 \left[ \frac{d^2 E_c}{d\rho^2} \right]_{\rho=\rho_0}. \quad (1.2)$$

For  $K_\infty \approx 200$  MeV the EOS is called soft, while for values around 380 MeV it is called stiff. A soft or stiff EOS can have a different impact on a neutron star, determining its mass and thus the way of its astrophysical evolution [Aic85].

Another feature related to the phase diagram of Fig. 1.1 is the so-called spontaneous breaking of chiral symmetry in the ground state [Rap00]. This results in a non-vanishing scalar quark condensate,  $\langle q\bar{q} \rangle \neq 0$ , in the hadron gas region, while in the QGP region  $\langle q\bar{q} \rangle = 0$ . Lattice QCD calculations predict indeed a partial restoration of chiral symmetry with increasing density  $\rho$  and temperature  $T$  (see Fig. 1.3). With such a scenario valid, the effective masses of the quarks are reduced to their current masses, i. e. in the order of a few MeV for  $u$  and  $d$  quarks and around 150 MeV for the  $s$  quark. This makes the production of quark-antiquark pairs energetically more favourable.

A change in the value of the quark condensate is also thought to indirectly affect the hadron properties [Gel68]. Similar effects have been predicted for vector mesons whose effective masses in the medium can be described by scaling laws. A change in the effective mass affects the production and propagation of particles in hot and dense nuclear matter. Such consequences of chiral symmetry restoration are summarized under the concept of in-medium effects, a term which, however, has a much broader scope.

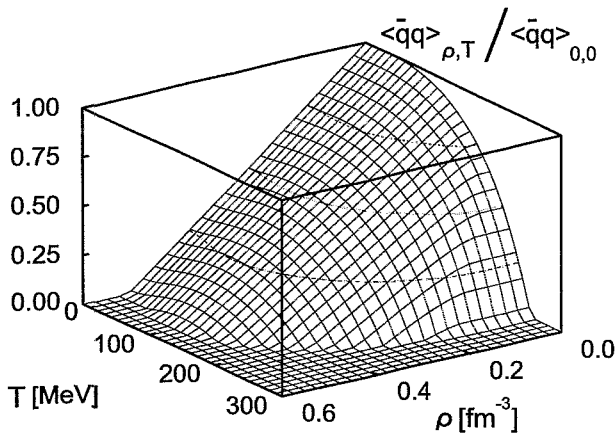


Figure 1.3: Dependence of the quark condensate  $\langle \bar{q}q \rangle$  on temperature  $T$  and nuclear matter density  $\rho$  according to the calculations in [Zsc02], in agreement with previous predictions from [Lut92]. The plot is quantitatively correct for small  $T, \rho$  and should be understood as a qualitative guidance at larger values of  $T$  and  $\rho$ .

Various experimental approaches have been applied in order to probe such phenomena. One way is to study vector meson decays into pairs of leptons, as the decay products do not interact strongly with the hadronic environment. Another way is to study strangeness production. It is less probable for strange mesons to be reabsorbed in nuclear matter in comparison with the antistrange or non-strange particles. The strong interaction conserves strangeness, which means that the production of an  $s$  quark is always associated with that of an  $\bar{s}$ . At SIS energies this is not very likely to happen because strange particles are rather rare. In this energy regime strange particles are mostly produced in sub- or near threshold reactions where in-medium effects have a pronounced effect on the particle yields. Such effects have been documented so far for kaons [För03, Men00, Cro00, Wis00, Dev02]. Moreover, the comparison of  $K^+$  under threshold production at light and heavy collision systems has provided evidence for a soft nuclear EOS [Stu01].

Apart from strange mesons, strange baryons (hyperons) produced in heavy-ion collisions need to be studied as well, in order to have a complete picture of the strangeness production. Of additional interest are phase space distributions, commonly parameterized by inverse slope parameters, the strange-antistrange particle ratios, as well as the Wroblewski factor  $\lambda_s$  [Wro85], which is a common way of comparing strangeness yields and enhancement across different systems.

In this thesis the focus is on the  $\Lambda(1116)$  production in C+C collisions at 2 AGeV beam kinetic energy.  $\Lambda$  hyperons are very important for the physics of neutron stars. The  $s$  quark is likely to play a significant role for the composition of neutron star matter, since several potential building blocks of such matter contain strange quarks as one of their constituents. At the densities that exist in the interior of neutron stars, the neutron chemical potential easily exceeds the mass of the  $\Lambda$ , so that neutrons would be replaced with  $\Lambda$  hyperons, accompanied with smaller populations of  $\Sigma$  and multi-strange baryons  $\Xi$ . According to predictions, this can already take place for densities of just  $\sim 2\rho_0$  and the total hyperon population may be as large as 20% [Gle85]. A modification of the strange matter properties due to the higher density would lead to alterations of masses, radii, cooling behaviour and surface composition of neutron stars, and may even give rise to new classes of com-

pact stars, such as strange stars and strange dwarfs. In the same context, there exist theoretical studies predicting in-medium modifications of  $\Lambda$  [Jin94, Yag02] but without offering directly measurable observables for experimentalists so far.

$\Lambda$  hyperons are produced together with a  $K^+$  or a  $K^0$  because of strangeness conservation in strong interactions. In the free nucleon-nucleon reaction the process  $NN \rightarrow K\Lambda N$  needs a kinetic beam energy of around 1.6 GeV for a fixed target experiment. Nevertheless, in a heavy-ion reaction it is still possible to produce particles at energies below threshold, either because the effective mass of the particle in the medium has changed and/or because collective effects are at work.  $\Lambda$  particles decay weakly at a timescale of about  $10^{-10}$  s, almost twelve orders of magnitude larger than the timescale of a hadron or heavy-ion reaction itself. This means they decay out of the fireball with their products not being influenced by hadronic interactions. As a consequence, a possible in-medium modification of their mass cannot be accessed in this way. Only their total production yield may reflect the existence of such a possibility and/or the impact of collective effects. To address all these phenomena, there is need to study hyperons at a variety of beam energies from light to heavy collisions systems.

Many of the  $\Lambda$  properties have been extensively studied, particularly in high energy heavy-ion reactions [Lam02, Sim05, Tak05, Van05, Alt06]. Elementary proton-proton reactions have also been investigated [Kow04, Sew99], close to the production threshold up to higher energies. However, in the regime of medium energies, the available database can still be completed. Heavy systems have been covered by the FOPI collaboration [Lop04, Mer05], as well as the EOS collaboration [Chu02, Pin02], while lighter systems have so far been addressed by experiments performed at JINR in Dubna [Gas85, Ani84] and Bevalac [Har81].

Now with the High Acceptance DiElectron Spectrometer (HADES) the opportunity is given to get an insight into the light system of C+C. The available high resolution tracking can serve for the reconstruction of rare probes like the  $\Lambda$  hyperons and lead to the first measurement of the total production cross section for the specific system and energy. Apart from the physics motivation though, the analysis of such a challenging probe can contribute valuable experience to the dilepton reconstruction methods, as the data under study belong to the first physics runs of the HADES experiment.

In the next chapter the reader is guided through the HADES spectrometer, with a more elaborate presentation of parts of the hardware, their properties and characteristics in chapter 3. Chapter 4 is dedicated to the  $\Lambda$  analysis techniques in simulation and their application on the experimental data. The thesis concludes with the results of this effort in chapter 5, comparisons with other experiments and discussion of the result.

## 2 The HADES Spectrometer

### 2.1 Aim and Requirements

The HADES spectrometer at GSI, Darmstadt, is designed for electron-positron pair spectroscopy at incident beam energies up to 2 AGeV for heavy ions, and up to 4 GeV for protons. These energies together with a proper choice of the collision system allow access to a certain region of the nuclear matter phase diagram (see Fig. 1.1) ranging from ground state matter density  $\rho_0$  up to  $3\rho_0$ , and temperatures  $T$  up to 100 MeV.

The dielectron pairs produced by the decay of vector mesons or other processes are used for the construction of the invariant mass spectrum, allowing a direct access to the vector mesons spectral function. Fig. 2.1 depicts some of the processes that lead to dielectron production. All four processes include the production of an intermediate virtual photon  $\gamma^*$ , which decays into the dielectrons that are measured.

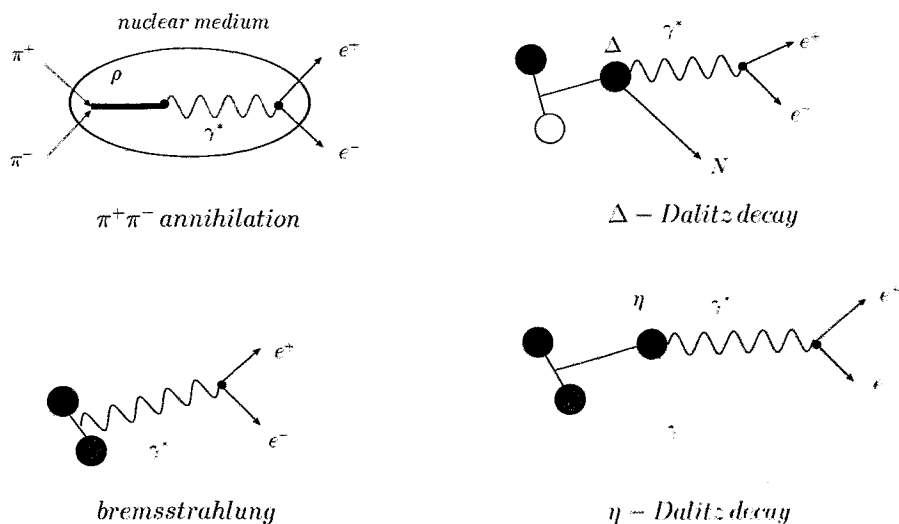


Figure 2.1: Schematic illustration of a few processes of dielectron production.

According to the Vector Dominance Model (VDM), the virtual photon couples directly to the vector mesons. This is particularly important for the pion annihila-

tion process  $\pi^+\pi^- \rightarrow \rho \rightarrow \gamma^* \rightarrow e^+e^-$ . Therefore, a change of the properties of the  $\rho$  meson becomes directly accessible through the  $e^+e^-$  pair. Similar considerations hold for the  $\omega$  and  $\phi$  mesons which are, however, produced in other processes. While such pure  $s$  channel processes refer directly to the strength ("mass") distribution of the original  $\rho$ ,  $\omega$  and  $\phi$  mesons, the other processes depicted in Fig. 2.1 cause broad continuum distributions of the resulting  $e^+e^-$  pairs, constituting background.

Considering the case of the  $\rho$  decay,  $\rho \rightarrow e^+e^-$ , the knowledge of the four-momenta of  $e^+$  and  $e^-$  provides the possibility to calculate the original  $\rho$  mass. The invariant mass  $m_{inv}$  of a  $e^+e^-$  pair is defined as

$$m_{inv} = \sqrt{P_\mu(e^+ + e^-)P^\mu(e^+ + e^-)} \approx 2\sqrt{p_{e^+}p_{e^-}} \sin(\alpha/2), \quad (2.1)$$

where  $P^\mu(e^+ + e^-) = p^\mu(e^+) + p^\mu(e^-)$  is the four-vector for the  $e^+e^-$  pair,  $p_{e^\pm} = |p_{e^\pm}|$  and  $\alpha$  is the opening angle between the two three-momentum vectors,  $\vec{p}_{e^\pm}$ . The last relation emerges when the  $e^\pm$  masses are neglected, which is justified for energies above some hundred MeV. So, in order to determine the invariant mass of the dielectrons, the momenta  $p_{e^\pm}$  of the electrons and positrons, as well as their opening angle  $\alpha$  are required, both of which are measured in a common reference frame, i. e. the laboratory system.

Generally, a dielectron invariant mass spectrum consists of a smooth background, with several peaks sitting on it. As an illustrative example, we depict model calculations from the HADES proposal [pro01] (see Fig. 2.2). The first steps of the HADES operation have been exactly devoted in identifying the contributions from  $\rho$ ,  $\omega$  and  $\phi$  decays [Ebe05, Prz06].

For the identification of the different mesons in the mass spectra the relative  $e^+e^-$  mass resolution  $\Delta m_{inv}/m_{inv}$  must be optimized. Especially in the mass region of  $\rho$  and  $\omega$  (700-800 MeV),  $\Delta m_{inv}/m_{inv}$  must be appropriate to resolve the resonance width of  $\omega$ , i. e. it should be approximately 1%. Some characteristic features of light vector mesons are listed in Tab. 2.1.

meson	mass (MeV/c <sup>2</sup> )	width (MeV/c <sup>2</sup> )	lifetime $\tau$ (fm/c)	$e^+e^-$ branching ratios
$\rho$	768	152	1.3	$4.4 \times 10^{-5}$
$\omega$	782	8.43	23.4	$7.2 \times 10^{-5}$
$\phi$	1019	4.43	44.4	$3.1 \times 10^{-4}$

Table 2.1: Characteristic quantities of light vector mesons.

In order to solve the puzzling results of the first generation experiments posed by DLS [Por97], the resolution and statistical significance must be substantially improved. The resulting requirements of the HADES spectrometer are:

⇒ Large geometrical acceptance

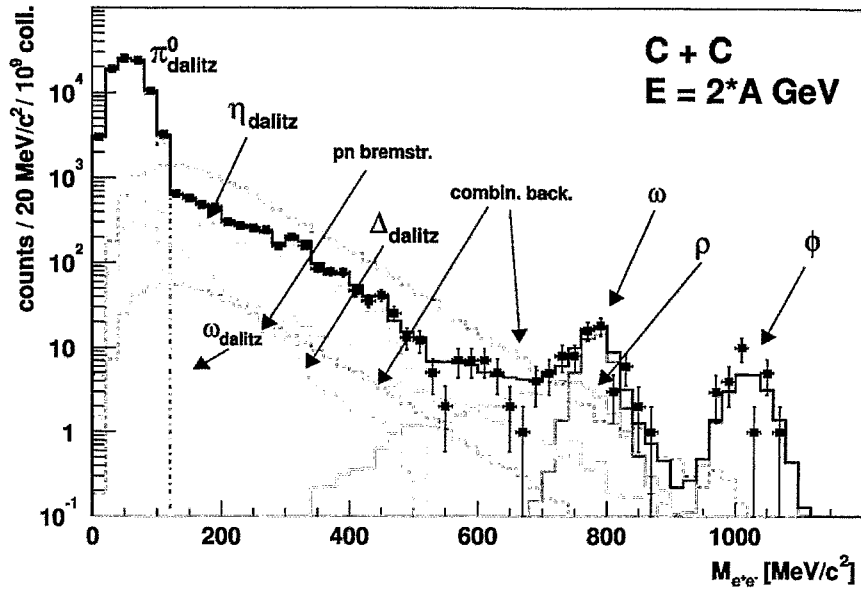


Figure 2.2: Example of simulated invariant mass spectrum of  $e^+e^-$  pairs for the reaction  $C+C$  at  $E_{kin} = 2 A \text{ GeV}$ . Various individual contributions are separately depicted. A total yield (squares and solid histogram) of approximately 180,000 pairs is expected for  $2 \cdot 10^9$  semi-central collisions ( $\approx 40\%$  of the total cross section). In the  $\rho/\omega$  mass region about 180 counts are expected. The picture is taken from [pro01].

To detect the maximum number of dielectrons a large geometrical acceptance is necessary. This is realized via the concept of nearly full azimuthal coverage with rotational symmetry. The spectrometer covers around 80% of the azimuthal angle and  $15^\circ - 85^\circ$  of the polar angles. This results to a geometrical acceptance of around 40% for  $e^+e^-$  pairs.

#### ⇒ Count rate stability

The vector mesons  $\rho$ ,  $\omega$  and  $\phi$  decay into dielectrons with branching ratios with an order of magnitude  $10^{-4}$  (see Tab. 2.1). In order to detect such pairs with good statistics, a high reaction rate is required. As a consequence, the HADES spectrometer should be able to handle beam intensities up to  $10^8 \text{ Hz}$ , with corresponding requirements on the detectors and the data acquisition.

#### ⇒ Mass resolution

As mentioned above, the relative mass resolution should be  $\Delta m_{inv}/m_{inv} \simeq 1\%$ , so as to be able to detect possible modifications in the  $\rho/\omega$  region.

#### ⇒ Track resolution

Electron-positron pairs are not only created by the decay of vector mesons but also by many other processes. Pairs could even stem from an electron and a positron from different conversion processes, e. g. a positron from an external conversion and an electron from a  $\pi^0$  Dalitz decay, or a positron from a  $\pi^0$  Dalitz decay and an electron from Compton scattering of a  $\gamma$  quantum. In order to suppress this combinatoric leptonic background, it is necessary to reconstruct all the trajectories of dielectrons. This requires a high track resolution of the detector system, in combination with the use of a low material quantity to diminish the scattering and the secondary reactions of the  $e^+e^-$  pairs.

#### ⇒ Dedicated lepton trigger

As the dielectron decays of vector mesons are rare, an efficient trigger is mandatory for the selection of those events that contain leptons. For this purpose, a three-level trigger is developed and applied, enriching the sample of data with the events of interest (see section 2.8.3).

## 2.2 General Overview of the HADES Setup

A schematic view of the spectrometer is depicted in Fig. 2.3. From left to right visible are the Ring Imaging Cherenkov counter (RICH), the inner two planes of Multiwire Drift Chambers (MDC), the superconducting magnet coils, the outer two planes of MDC, the Time of Flight walls (TOF) and finally the Pre-Shower detector. The setup is divided into six identical sectors surrounding the beam axis.

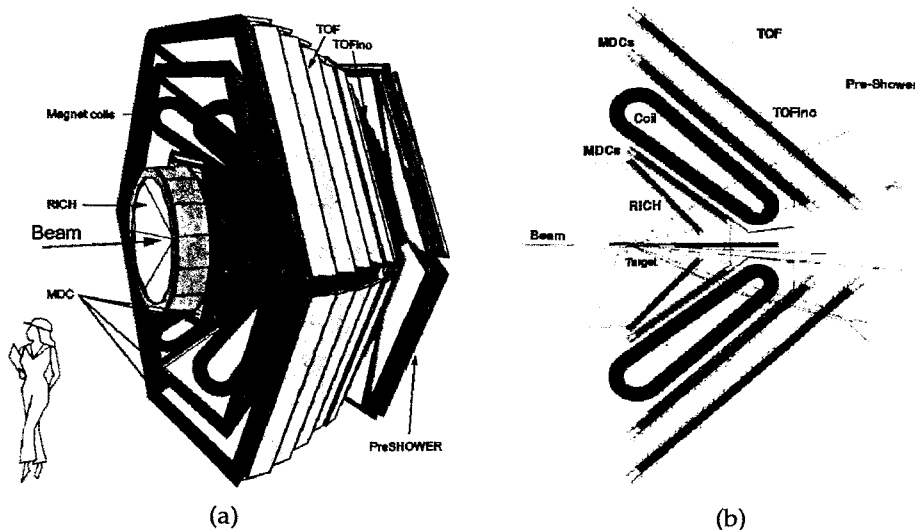


Figure 2.3: Three- (a) and two-dimensional (b) view of the HADES spectrometer. The distance between the target and the TOF walls is around 2 m.

The TOF walls are primarily used for event selection according to the charged particle multiplicity in every reaction. They also serve particle identification purposes and in combination with the magnet and the MDC, the track reconstruction takes place and the momentum calculation is performed. The RICH and the Pre-Shower detectors are used for the lepton identification, the Pre-Shower only for the forward angles. They also contribute to the lepton track reconstruction by delivering position information. In the coming sections a more elaborate description of the sub-detector units is presented following the sequence particles traverse the HADES setup with.

## 2.3 The Start and Veto Detectors

The start signal for the measurement of an event in HADES is generated by the Start and Veto detectors. The latter are two identical octagonally shaped poly-crystalline diamond counters, placed 75 cm downstream and 75 cm upstream of the target (see Fig. 2.4). Their thickness is  $100\ \mu\text{m}$  [Ber01], in order to keep the multiple scattering effect and the secondary reactions rate low. Thanks to the fast rise time and the small

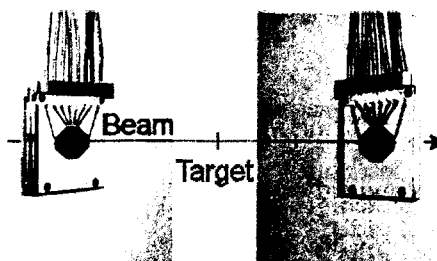


Figure 2.4: The position of the Start and Veto detectors with respect to the target.

pulse width, their time resolution is about 50 ps, allowing for primary rates up to  $10^8$  Hz. The two detectors work in anti-coincidence mode, i. e. in case both of them give a signal, the event is vetoed. Thus, events in which there was no interaction of the projectile with the target are rejected.

## 2.4 The Ring Imaging Cherenkov Detector

Cherenkov detectors serve for particle identification purposes on the basis of the particle velocity. Around the trajectory of a particle crossing a dielectric medium a time-dependent electric field is generated. This leads to a variable polarization in the neighbourhood of the particle. If the velocity of the particle is faster than that of light in the same medium, the produced wavefronts will constructively overlap with an opening angle  $\theta_c$  around the trajectory, which is connected to the refraction

index of the medium  $n_{ref}$  and the particle velocity  $\beta$  (normalized to the velocity of light  $c$ ) with the relation [Che37]

$$\cos\theta_c = \frac{1}{n_{ref}\beta}, \quad \beta = \sqrt{1 - \frac{1}{\gamma^2}}, \quad (2.2)$$

where  $\gamma$  is the Lorentz factor. For each material there is a threshold velocity  $\beta_{thr}(\gamma_{thr})$  which the particle has to exceed in order to produce Cherenkov light. This is deduced from the inequality  $\cos\theta_c \leq 1 \Rightarrow n_{ref}\beta \geq 1 \Rightarrow \beta_{thr} = 1/n_{ref}$ . In the SIS energy regime, electrons and positrons emitted in nuclear collisions have velocities  $\beta \approx 1$ , while hadrons have  $\beta < 0.95$ . The radiator gas  $C_4H_{10}$  was chosen to have a refraction index of  $n_{ref} = 1.00151$  giving  $\gamma_{thr} \approx 18.2$ , i. e.  $\gamma_{lepton} \geq \gamma_{thr}$  and  $\gamma_{hadron} \leq \gamma_{thr}$ . The Cherenkov effect can therefore be used to distinguish leptons from hadrons and to obtain a trigger signal for events containing  $e^+e^-$  pairs. Thus, the detector is hadron blind [Zei99].

A schematic view of the RICH is shown in Fig. 2.5. The leptons produced on the target travel through the radiator gas and are the only particles to emit Cherenkov radiation. The photons reflected on the spherical mirror will cross the VUV transparent  $CaF_2$  window and hit a two-dimensional photon detector forming a ring. The light collected this way allows to determine the emission angle of the leptons using the coordinates of the ring.

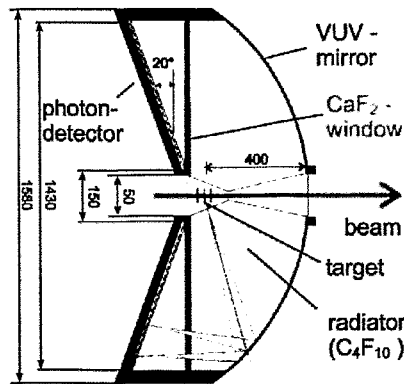


Figure 2.5: Schematic view of the RICH detector [Böh99].

## 2.5 The Tracking System

### 2.5.1 The Multiwire Drift Chambers

For the accurate reconstruction of the charged particle tracks the use of position sensitive detectors is imperative. Additionally, a strong magnetic field is required

for bending high momentum tracks and being able to reconstruct the momentum of the particles. The motion of a particle in a magnetic field  $\vec{B}$  is governed by the Lorentz force,  $\vec{F} = q\vec{v} \times \vec{B}$ , from which follows

$$\Delta\vec{p}_t = \int d\vec{p} = \int \vec{F}dt = \int q(\vec{v} \times \vec{B})dt = -q \int \vec{B} \times d\vec{s}, \quad (2.3)$$

where  $\Delta\vec{p}_t$  is the momentum transfer defined to be perpendicular to  $\vec{p}$ ,  $q$  is the charge of the particle and  $d\vec{s}$  is tangential to its trajectory. Knowing the magnetic field  $\vec{B}$ ,  $\Delta\vec{p}_t$  and the deflection angle of the track, it is possible to calculate the momentum of the particle.

The HADES tracking system consists of four MDC planes (I-IV), two before and two behind the field area of the superconducting toroid (see Fig. 2.6). Each chamber plane is composed of six trapezoidal modules and has the shape of a frustum. A module covers  $60^\circ$  of azimuthal angle and each four modules of the MDC I to IV form a sector. Module sizes range from  $88 \text{ cm} \times 80 \text{ cm}$  to  $280 \text{ cm} \times 230 \text{ cm}$  (height  $\times$  larger baseline).

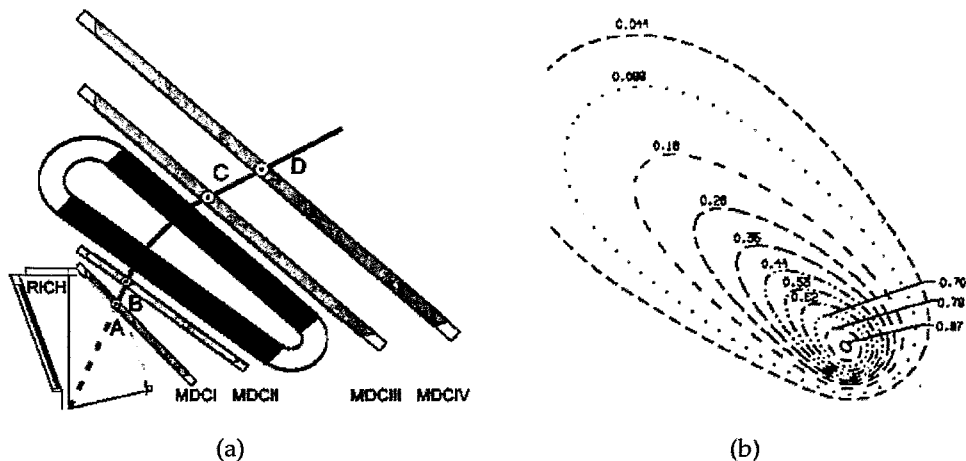


Figure 2.6: (a) Schematic view of a charged particle path. Knowing the strength of the magnetic field in space it is possible to reconstruct the momentum of the particle using the inner and outer segments  $\overrightarrow{AB}$  and  $\overrightarrow{CD}$  [Lip00]. (b) A transversal cut of the magnetic field map at  $\phi = 0$  (along the middle of a sector). The numbers label the value of the magnetic field in Tesla along the dashed and dotted lines.

A chamber module is composed out of six drift cell layers. The cell sizes vary from  $5 \times 5 \text{ mm}^2$  to  $14 \times 10 \text{ mm}^2$  from MDC I to IV to achieve a constant granularity. The cells are formed by interspersed sense and field wires and cathode wire planes. The total number of drift cells is approximately 27,000 (for the complete setup). Chapter 3 is dedicated to a more detailed description of the third layer of MDC modules.

## 2.5.2 The Superconducting Magnet

In order to achieve the strong magnetic field required for high momentum resolution with the largest radiation length and smallest size possible, a superconducting magnet is necessary. The HADES superconducting toroid consists of six coils in separate vacuum chambers [Bre99]. The coil cases are aligned with the frames of the drift chambers and all other segmented detectors to reduce dead space in the spectrometer (see Fig. 2.6). It is cooled with liquid He and the strength of the field it produces is 3.7 T inside the coil cases, 2.4 T nearby and 0.8 T in the centre of a sector.

## 2.6 The Time of Flight Walls

The scintillation TOF walls [TOF00, God02], installed behind the tracking system, provide fast determination of the charged particle multiplicity per event used for event centrality selection. Moreover, they measure the time of flight of each detected particle for the facilitation of lepton separation from heavier products. In the HADES spectrometer this detector ensemble comprises two parts: the TOFino detector covering polar angles from  $18^\circ$  to  $45^\circ$  (also called system 0) and the TOF wall from  $45^\circ$  to  $88^\circ$  (system 1).

TOFino consists of six identical sectors installed right before the Pre-Shower detectors. Each sector is made of four plastic scintillator stripes and is read out only from one side. This, in addition with the low granularity, reduces the time resolution of the detector to 400 ps. For the C+C system at 2 A GeV, 20% of the collisions induce a double hit in the TOFino region. For those events the time of flight measurement for one of the two particles is lost. For studies of heavier systems the TOFino detector is going to be replaced by Resistive Plate Chambers (RPC) [Fon01, Día03], which fulfil the requirements for a high multiplicity environment.

The TOF wall is also made of six sectors in hexagonal geometry, each one constituted by thirteen cases containing eight scintillating bars. Each bar is read out at both ends by means of fast photomultipliers. In combination with the higher granularity, the time resolution of TOF is 100-150 ps (corresponding to spatial resolution of 1.5-2.3 cm). Both detectors are illustrated in Fig. 2.7.

## 2.7 The Pre-Shower Detector

Below the angle of  $45^\circ$  the discrimination of electrons becomes less efficient due to the presence of fast pions. For this reason the information about characteristic electromagnetic showers caused by leptons in heavy material is used. The HADES Pre-Shower detectors [Sho00, Bal04] consist of two lead converters inserted between three wire chambers with pad readout (see Fig. 2.8). Shower recognition is performed by comparing the number of particles measured before and after the lead converters. In the case of hadrons this ratio is close to 1, while for leptons it is larger

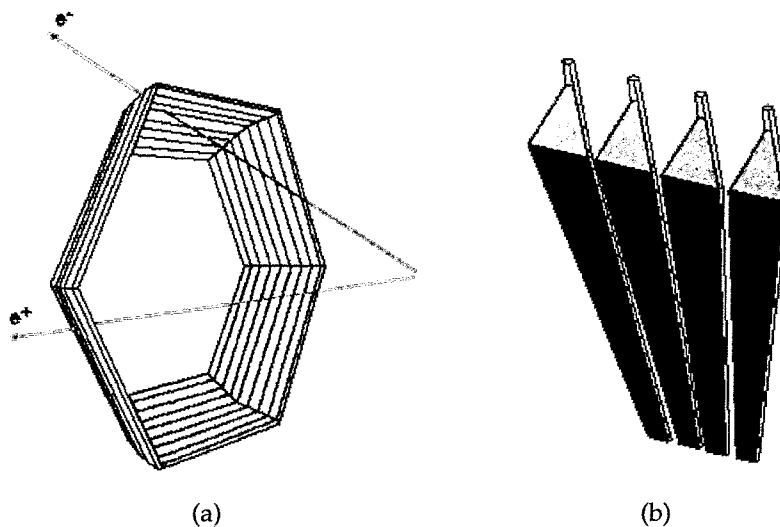


Figure 2.7: (a) View of the scintillator of the TOF detector. (b) View of the the scintillator of the TOFin detector.

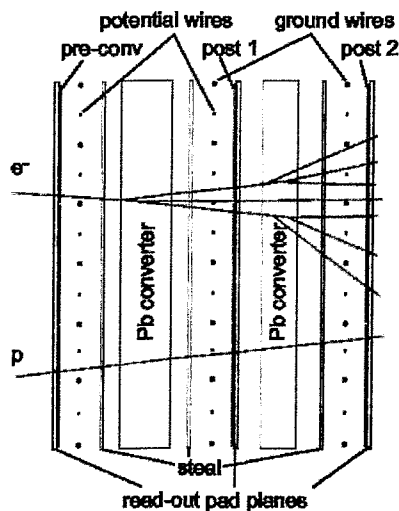


Figure 2.8: View of the Pre-Shower detector with its lead converters and the readout pad planes.

than 1. Particle hits are identified via charge produced in ionization processes in the wire chambers working in the self-quenching streamer (SQS) mode. The main advantage of the SQS mode is that the induced charge is nearly independent of the particle's specific energy loss. Therefore, low energy protons do not produce large signals in the post converter chambers with their significant energy loss and finally are not misidentified as electromagnetic showers. The Pre-Shower detector together with the TOFin and TOF walls form the Multiplicity and Electron Trigger Array

(META).

## 2.8 The HADES Trigger Concept

The reason for the existence of the HADES trigger system is the identification of dielectron events. Its main task is the on-line selection of events that contain an  $e^+e^-$  pair. There are three trigger levels which contribute to the above discrimination.

### 2.8.1 First Level Trigger (LVL1)

The first level trigger involves a fast hardware selection of central collisions, which takes place in less than 100 ns, employing the multiplicity information from the META detector. When the multiplicity exceeds a certain threshold, the collision is considered to be sufficiently central. For a beam intensity of  $10^8$  Hz and a target interaction probability of 1%, the final rate the data acquisition has to deal with is  $10^6$  Hz. The centrality selection via the LVL1 trigger can decrease the primary event rate up to a factor of 10, which leads to trigger rates of  $10^5$  Hz.

### 2.8.2 Second Level Trigger (LVL2)

The second level trigger reduces the number of accepted events without changing the primary rate. Its purpose is to enrich the recorded events with leptons. A fast identification of  $e^+e^-$  tracks ( $< 10 \mu\text{s}$ ) takes place in parallel with the readout of the detector data. The realization of the second level trigger takes place via Image

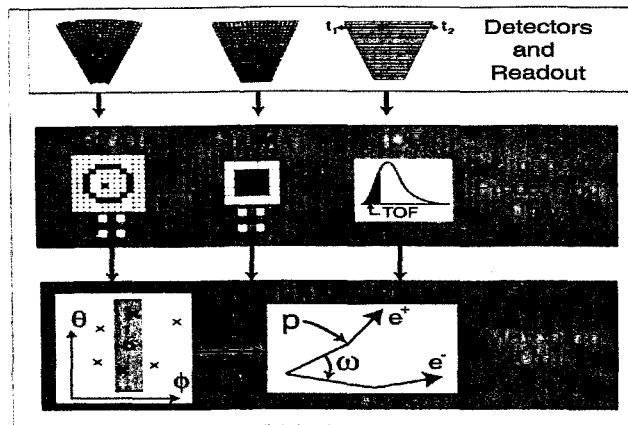


Figure 2.9: Schematic illustration of the second level trigger functions.

Processing Units (IPU) installed on the RICH [Leh99, Leh00], the TOF [Lin01] and the Pre-Shower detectors [Pet00]. As a first step, a ring position derived from fired RICH pads, a signal from the Pre-Shower and a time information from the TOF

are recorded (see Fig. 2.9). As a second step, a Matching Unit (MU) correlates the corresponding coordinates taking into account the deflection of the particle in the magnetic field. The third step is to combine the identified lepton candidates with opposite charge and calculate the invariant mass with use of a table, which defines the relation between the deflection angle of the particle and its momentum. Accepted are only pairs that lie within a specific range of invariant masses. The reduction factor for the second level trigger is 100, leading to a rate of  $10^3$  Hz. Detailed descriptions, as well as first results can be found in [Tra01, Leh03, Toi03, Toi04].

### 2.8.3 Third Level Trigger (LVL3)

The third level trigger correlates the identified tracks by RICH and META with the corresponding MDC signals. Provided they are within a certain angle window, the trigger decision is positive. So far the third level trigger works off-line and is emulated by software. The data reduction is by a factor of 10 which leaves us usually with rates of  $10^2$  Hz.

## 3 The Multiwire Drift Chambers

The MDC modules are sensitive and delicate detectors and therefore their operation and maintenance demand that some work be dedicated to the study of certain aspects of their properties. In this chapter an introduction to the MDC operation principles is presented along with some interesting details of the manufacturing procedure, operational experience, as well as the tactics followed for their repair.

### 3.1 Principles of MDC Operation

A drift chamber is a gaseous detector that allows the determination of spatial coordinates along trajectories of particles which traverse its active volume, resulting in excitation and ionization of the atoms of the medium. Of all possible interactions only the electromagnetic one is generally used as a basis for detection, being many orders of magnitude more probable than strong or weak interactions [Sau77].

On the passage of the particle a discrete number of primary ionizing collisions takes place, which liberate electron-ion pairs in the medium. The electrons ejected are accelerated by the field towards the anodes and can have enough energy (larger than the ionization potential of the medium) to further ionize, producing secondary electron-ion pairs; the sum of the two contributions is called total ionization. The total number of electron-ion pairs can be expressed by  $n_T = \Delta E/W_i$ , where  $\Delta E$  is the total energy loss in the gas volume considered and  $W_i$  is the effective average energy to produce one pair. An expression for the average energy loss per unit length due to Coulomb interactions has been obtained by Bethe and Bloch in the framework of relativistic quantum mechanics [Sau77]

$$\frac{dE}{dx} = -K \frac{Z}{A} \frac{\rho}{\beta^2} \left( \ln \frac{2mc^2 \beta^2 E_M}{I^2 (1 - \beta^2)} - 2\beta^2 \right), \quad K = \frac{2\pi N z^2 e^4}{mc^2}, \quad (3.1)$$

where  $N$  is the Avogadro number,  $m$  and  $e$  denote the electron mass and charge,  $Z$ ,  $A$ , and  $\rho$  stand for the atomic number, the mass and the density of the medium respectively,  $I$  is its effective ionizing potential,  $z$  is the charge and  $\beta$  the velocity of the projectile. The quantity  $E_M$  represents the maximum energy transfer allowed in each interaction. Inspection of the above formula shows that the differential energy loss depends only on the projectile velocity  $\beta$  and not on its mass. After a fast decrease dominated by the  $\beta^{-2}$  term, the energy loss reaches a constant value

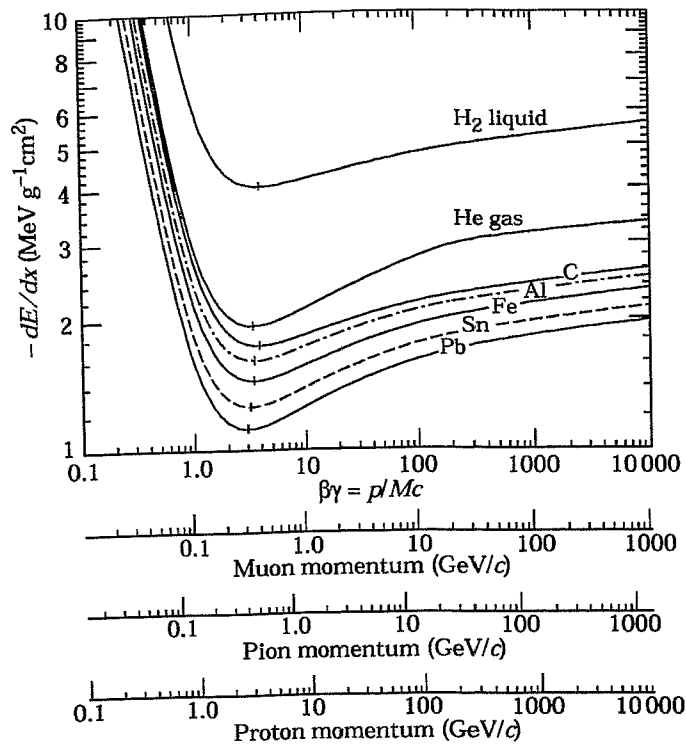


Figure 3.1: Energy loss rate in liquid (bubble chamber) hydrogen, gaseous helium, carbon, aluminum, tin and lead for muons, pions and protons, as a function of  $\beta\gamma$ . The energy loss does not depend on the mass of the ionizing particle but on its velocity. After a rapid decrease, the energy loss reaches a stable region around  $\beta \sim 0.97$  ( $\beta\gamma \sim 4.1$ ) and then starts rising again for larger values of  $\beta$  (relativistic rise) [PDG].

around  $\beta \approx 0.97$  and eventually slowly increases for  $\beta \rightarrow 1$  leading to the relativistic rise (see Fig. 3.1). As described above, along the particle trajectory the formation of localized groups of electrons, called clusters, takes place. In typical drift chamber gases they consist of 1-3 electrons. In the HADES drift chambers, the usual gas mixture used consists of 60% helium and 40% isobutane. In pure He the number of electron-ion pairs created per unit length is  $n(\text{He}) = 7.8$ , while for isobutane it is  $n(\text{iC}_4\text{H}_{10}) = 195$ . That gives a total number of electron-ion pairs per unit length for the gas mixture equal to  $n(\text{He} - \text{iC}_4\text{H}_{10}) = 0.6n(\text{He}) + 0.4n(\text{iC}_4\text{H}_{10}) = 83$ . The majority of the pairs are produced by isobutane and not by the main gas of the mixture. The criteria for the selection of the gas components are explained in section 3.3.

## 3.2 Gas Amplification

The read-out of the drift chambers [Wüs05] results in time information which corresponds to the drift time of the primary electrons from the location of their creation to

the closest sense (anode) wire. The arrival of these electrons determines the beginning of the signal. The behaviour of the drift velocity depends on the drift properties of ions and electrons in the gas medium of the chamber.

In most of the region where the charges are produced by the primary interaction processes, the electric field only makes electrons drift towards the sense wires and positive ions towards the negative electrodes. But very close to the anode, normally at a few wire radii, the field gets strong enough for charge multiplication to start. A typical drop-like avalanche develops with all electrons in the front and ions behind (see Fig. 3.2).

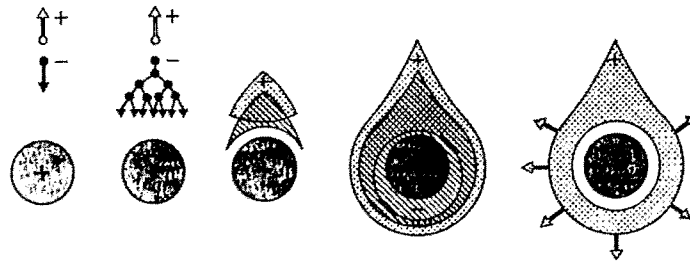


Figure 3.2: Time development of an avalanche in a gaseous counter [Sau77]. A single primary electron proceeds towards the anode, in regions of increasingly high fields, experiencing ionizing collisions; due to the lateral diffusion, a drop-like avalanche develops surrounding the wire. Electrons are collected during a very short time (1 ns or so) and a cloud of positive ions is left, slowly migrating towards the cathode.

If  $\lambda$  is the mean free path of an electron until the next ionization event, the inverse quantity,  $\alpha = 1/\lambda$ , gives the probability of such an event per unit length. The value  $\alpha$  is called Townsend coefficient and is a function of location. If  $n$  is the number of electrons, we have the creation of  $dn = n\alpha(x)dx$  new electrons per unit length  $dx$ . Thus, the multiplication factor  $M$  is given by integration as

$$M = \frac{n}{n_0} = \exp\left(\int_{r_1}^{r_2} \alpha(x)dx\right), \quad (3.2)$$

where  $n_0$  is the initial number of electrons. The multiplication factor cannot be arbitrarily increased. Secondary processes, like photon emission inducing the generation of avalanches spread over the gas volume, and space-charge deformation of the electric field (which is strongly increased near the front of the avalanche), eventually result in a spark breakdown. A phenomenological limit for multiplication before breakdown is given by the Raether condition

$$\alpha x \sim 20 \quad (3.3)$$

or  $M \sim 10^8$ ; the statistical distribution of the energy of electrons and therefore of  $M$  in general does not allow one to operate above  $\sim 10^6$  if one wants to avoid breakdowns. In the case of the HADES drift chambers, the factor  $M$  is around  $2\text{-}3 \cdot 10^5$ .

### 3.3 Choice of the Gas Filling

Since avalanche multiplication occurs in all gases, theoretically any gas or gas mixture can be used in a drift chamber. In most cases, however, the specific experimental requirements – many times conflicting – restrict the choice to several families of compounds. Some of these requirements are low working voltage, high gain operation, high rate capabilities and long detector life time.

Avalanche multiplication occurs in noble gases at much lower fields than in complex molecules; this is a consequence of the many non-ionizing energy dissipation modes available in polyatomic molecules. Therefore, the convenience of operation suggests the use of a noble gas as the main component. Addition of other components slightly increases the threshold voltage.

Polyatomic molecules have a very different behaviour, especially when they contain more than four atoms. The large amount of non-radiative excited states (rotational and vibrational) allows the absorption of photons in a wide energy range. This is a common property of most organic compounds in the hydrocarbon and alcohol families. The molecules dissipate the excess energy either by elastic collisions or by dissociation into simpler radicals. Even small amounts of a polyatomic quencher added to a noble gas changes completely the operation of a counter because of the lower ionization potential. Good photon absorption and suppression of the secondary emission allows gains in excess of  $10^6$  to be obtained before discharge.

### 3.4 Drift Velocity

As mentioned before, a drift chamber offers the possibility of measuring the electron drift time to get information about the spatial coordinates of an ionizing event. In its basic form, a single-cell drift chamber consists of a region of moderate electric field, followed by a proportional counter. Suitable field shaping electrodes, wires or strips, allow one to obtain the desired electrical configuration. Electrons produced at time  $t_0$  by the incoming charged particle migrate along the electric field lines with velocity  $v$  and reach the high field region approximately 1 mm from the anode wire where avalanche multiplication starts at a time  $t_1$ . The coordinate of the track, with respect to the anode wire, is therefore given by

$$x = \int_{t_0}^{t_1} v dt, \quad (3.4)$$

which reduces to  $x = (t_1 - t_0)v$  for a constant drift velocity  $v$ . It is obviously very convenient to have a linear space-time relationship and this can be obtained in structures with uniform electric field.

If a large surface of detection is required, a multi-cell structure can be used. In this case, the region of the anode wire becomes necessarily part of the active volume. So, it is not possible to obtain a constant drift field everywhere across the cell, as the

low field region between the anode wires would result in a strong non-linearity of the space-time relationship, especially for large wire spacings. A modification of the structure allows the elimination of low field regions between the anodes. In the HADES drift chambers the anode wires are alternated with five times thicker field-shaping cathode wires (called field wires) that reinforce the electric field in the critical region, sharpening at the same time the transition from one cell to another (see Fig. 3.3).

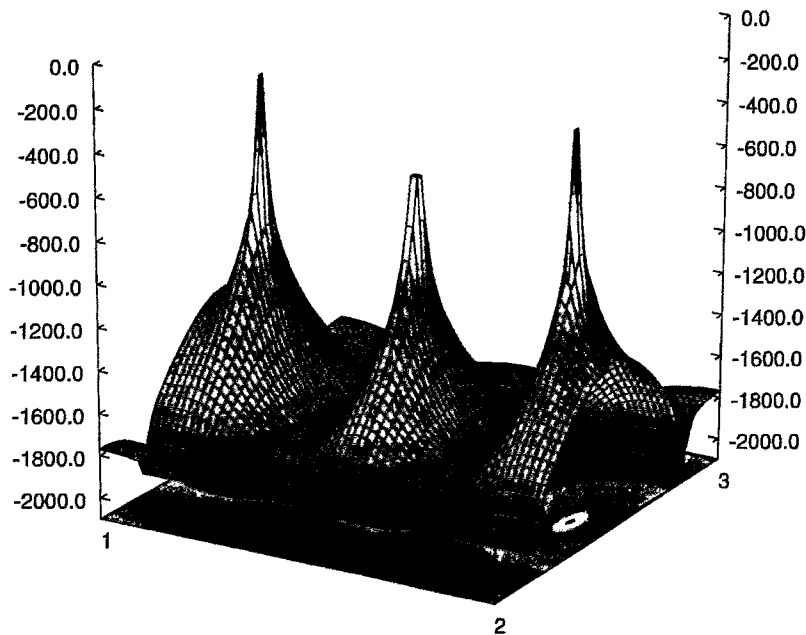


Figure 3.3: Potential distribution in an MDC drift cell. The calculation has been performed with Opera [Ope01], a commercial program for electromagnetic design. The colour code corresponds to the potential gradient. The three peaks represent the anode wires which are grounded (zero potential). The two outer peaks have higher potential due to boundary effects, as the outer drift cells are not fully included in the simulation. The valleys surrounding the three peaks are caused by the presence of field and cathode wires (-2000 V).

### 3.5 Construction of the HADES third MDC Plane

The drift chambers constructed in Forschungszentrum Rossendorf form the second largest tracking plane of the spectrometer. Since they comprise the third plane, the abbreviation MDC III is used from now on. They consist of six modules with an active area of roughly  $2.2 \text{ m}^2$  and a drift cell size of  $8 \times 12 \text{ mm}^2$ . Each module has six drift layers, i. e. six anodes and seven cathodes, consisting of wires glued on Stesalit<sup>©</sup> frames [Bou94]. The anode layers contain alternately sense wires (gold coated W,  $\varnothing = 20 \text{ }\mu\text{m}$ ) and field wires (Al,  $\varnothing = 100 \text{ }\mu\text{m}$ ) with a distance of 6 mm

from each other. The wires of the anode layers have five different orientations (see Fig. 3.4), whereas the wires of the cathode layers (Al,  $\varnothing = 80 \mu\text{m}$ ) always have the same orientation ( $+90^\circ$ ) with a distance of 3 mm from each other.

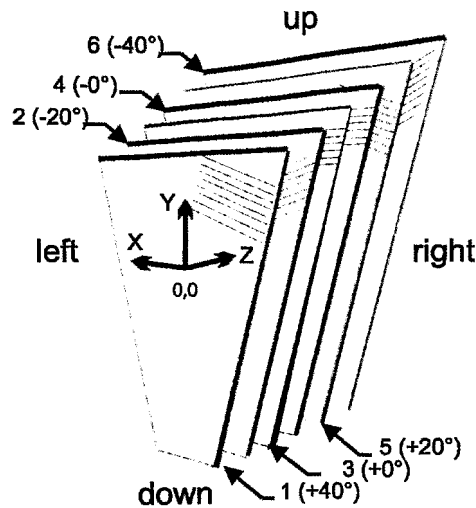


Figure 3.4: Schematic view of the anode frames inside a chamber module.

The wire planes are prepared by using an automatic winding machine, which has a high positioning precision (primarily  $\pm 2 \mu\text{m}$ ). This allows to wind sense and field wires on one frame. However, due to the big diameter of the field wires and their intrinsic tension, they roll away from their initial position. To correct this displacement for the case of anode layers, four combs have been installed at the two ends of the frame of the winding machine. These combs improve the accuracy, which reaches the value of  $\pm 10 \mu\text{m}$ . To avoid any further dislocations a mechanical tension force is applied during the winding process (0.5 N for the sense wires, 1.5 N for the field wires and 1.0 N for the cathodes). This tension force also compensates for the deformation (sagitta) of the wires due to gravitational and electrostatic forces. The wires are placed and glued with an isolating glue (Araldite<sup>®</sup> AW106) on the Stesalit frames. The process takes place in two stages because of the large size of the module. A special table, markers on the frames and cameras ensure that the wires are accurately placed, at the right distances (see Fig. 3.5) and on the same plane.

For the field and cathode wires an additional conductive glue containing silver is used for the formation of the galvanic contact. The sense wires are soldered from one side on a printed circuit connector, whose other side leads the invoked electric signal to the readout electronics via flex print cables (FPC). The whole construction is sealed with two mylar foils from both sides of the chamber.

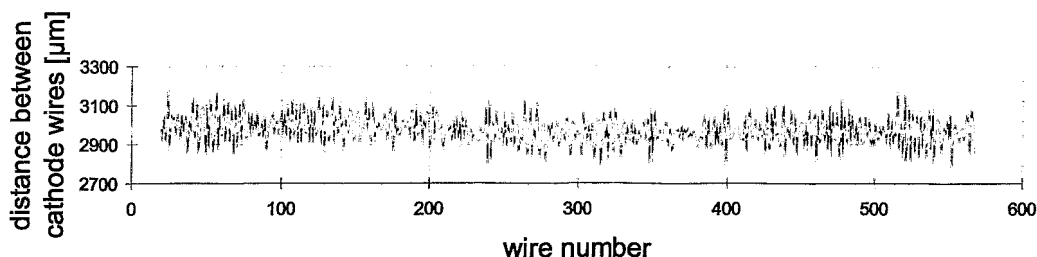


Figure 3.5: The measured position accuracy of the cathode wires of cathode plane 2, module 1 is within the acceptable value of  $\pm 100 \mu\text{m}$ .

### 3.6 Mechanical Tension Force Measurements

Before the layers are mounted together, the stretching force of every wire (especially for the anode layers) has to be measured with a tension meter. A current pulse is fed into the wire under test, connected electrically to the instrument, deflecting it from its quiescent position perpendicularly to a dipolar magnetic field (the deflecting force is produced by the interaction of the magnetic field of the current pulse with the magnet). The wire begins vibrating as a stretched string. Under the influence of the constant magnetic field, electric current is induced in the vibrating wire. The electric signal is amplified to a level necessary to drive the monostable multivibrator of the instrument at the suitable moment, providing another deflecting pulse. By appropriate regulation of the driving and deflecting signal, the wire starts vibrating continuously with nearly constant frequency.\*

In the case of a stretched wire with homogeneous cross section and density, with a diameter negligible compared to its length, and vibrating with an amplitude negligibly small in comparison to the longitudinal dimensions, the stretch  $F$  (in N) can be determined from the period  $\mathcal{T}$  of the fundamental frequency as

$$F = 100L^2d^2\rho\frac{\pi}{g\mathcal{T}^2}, \quad (3.5)$$

where  $L$  is the length of the wire in mm,  $d$  its diameter in  $\mu\text{m}$ ,  $\rho$  the density in  $\text{g}/\text{cm}^3$ ,  $\mathcal{T}$  the measured period in ms and  $g$  the gravitational acceleration of earth ( $9.81 \text{ m}/\text{s}^2$ ). Applying the above method, one obtains the results of the measurements shown in Figs. 3.6 and 3.7<sup>†</sup>.

\*The development of various wire chambers since the early 1970s and the task of manufacturing reliable, long-lived and high-quality instruments motivated many different approaches to measuring wire tensions. Usually, more indirect methods are employed in which the wire is first forced to vibrate, stimulated by the Lorentz or the Coulomb force, and then these vibrations are used to determine the tension force. A more detailed description of the available methods can be found in [Bor78, Cav75, Ste80, Bur73, Car88, Dur95].

<sup>†</sup>Measurements performed at the FZ Rossendorf detector laboratory.

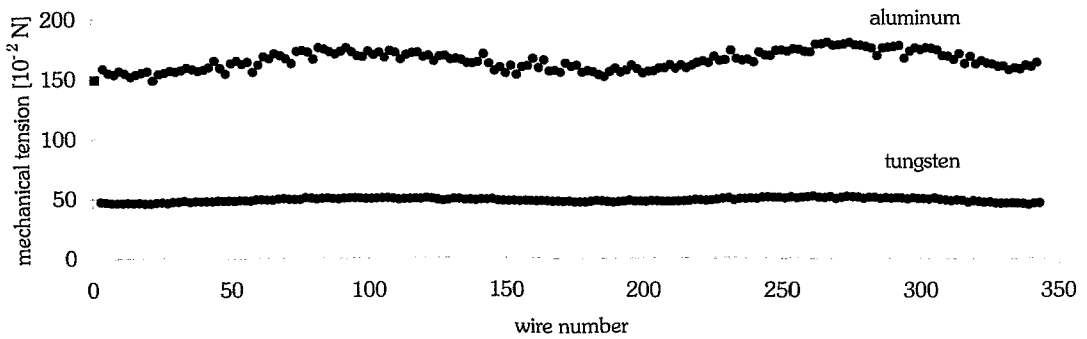


Figure 3.6: Measured wire tension force of field (Al,  $\varnothing = 100 \mu\text{m}$ ) and anode wires (W,  $\varnothing = 20 \mu\text{m}$ ) in a zero degree frame of module 3.

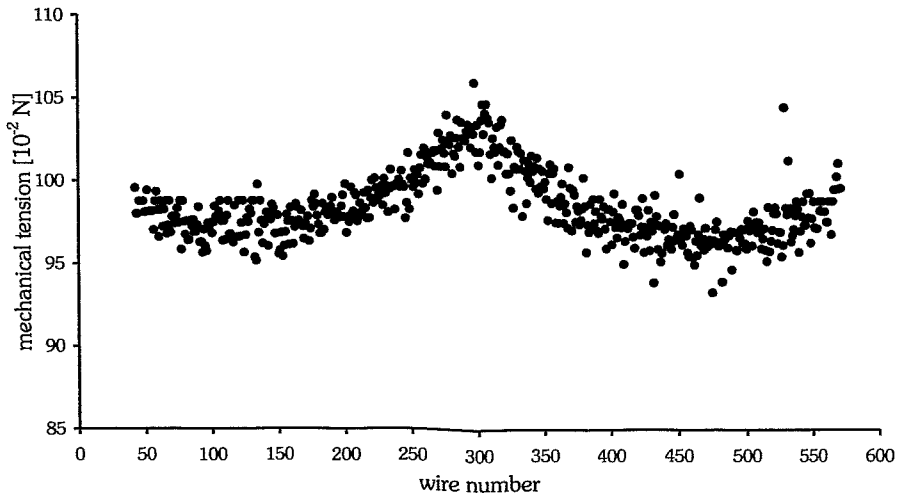


Figure 3.7: Measured wire tension force for cathode frame 2 of module 1 (Al,  $\varnothing = 80 \mu\text{m}$ ).

Although the wires are wound with a well defined constant tension force, the measurement shows that this is not longer the case, when they are fixed on the frames. The stretching force of the wires concomitantly causes a deformation of the Stesalit frames. The result is that the measured tension follows this deformation, as seen in the simulation of Fig. 3.8\*. The fluctuation is more evident for aluminum wires due to their smaller elasticity. The calculation was performed for a frame fixed on the table with four bolts in the middle of every side.

For one cathode layer the wire tension force was measured twice; first, when the frame was placed on the special table where the wires are glued. In this case,

\*Figure provided by Manfred Sobiella.

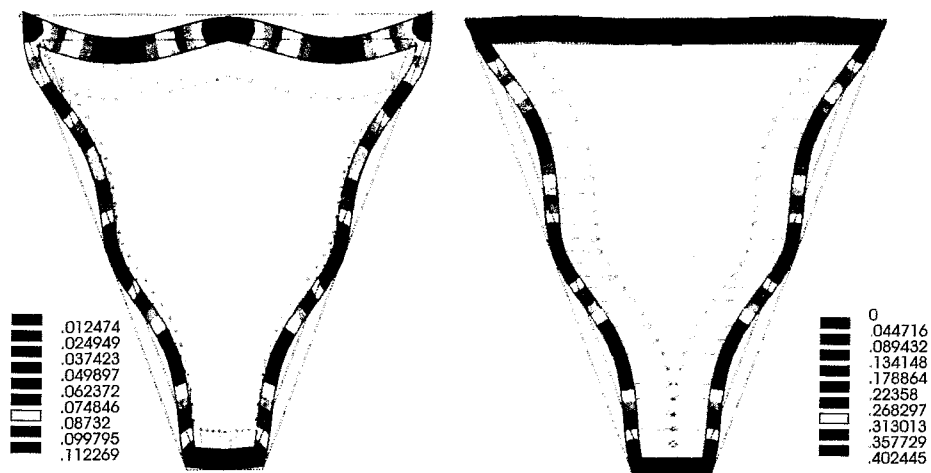


Figure 3.8: Simulations of the expected deformation in mm of Stesalit frames caused by the wire tension force (performed by Manfred Sobiella). On the left side a cathode layer is depicted, while on the right the deformation of a  $0^\circ$  anode layer is shown. The orientation of the wires determines the deformed shape of the frames.

apart from the four bolts, 29 additional holders along the sides of the detector were preventing the deformation. The measurement was repeated after the holders were removed and the plane was lying only with the support of the four bolts. The results are illustrated in Fig. 3.9. A variation of the tension in the order of 20% is not critical for the sagitta.

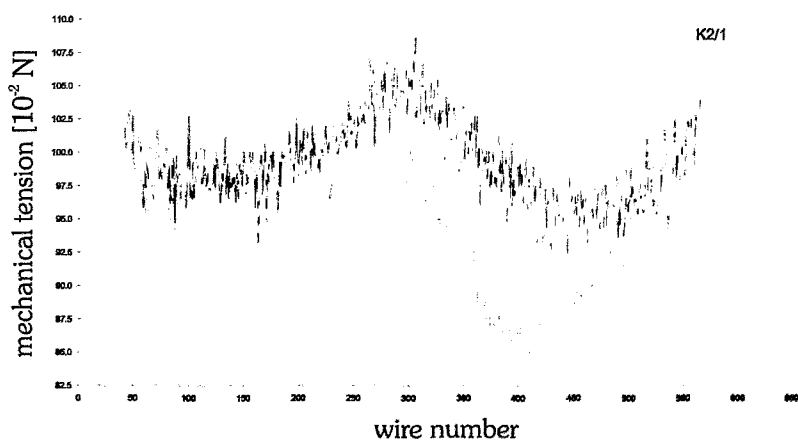


Figure 3.9: Tension force of cathode wires of cathode layer 2 of module 1. The upper curve is for the frame fixed with all the holders and the lower one for the one fixed with only four bolts.

### 3.7 Wire Displacements due to Gravitational and Electrostatic Forces

So far the wires are considered on the Stesalit frames without taking into account the behaviour of the tension under working conditions. Apart from the gravitational forces which are always present, the wires are also subject to electrostatic forces that tend to displace them, when high voltage is applied. The combined effect of these forces with the restoring mechanical tension results in an elastic deformation of the wire.

The wire deflection from the nominal position can be estimated by solving the differential equation which describes its equilibrium state. Such a calculation can be performed with the program Garfield [Gar00]. The differential equation describing the shape  $y(x)$  of a wire ( $x$  runs along its length) subject to an external force  $f(x)$  can be derived by making the following assumptions:

- ⇒ the wire deflection is small compared to the length of the wire,
- ⇒ the wire elongation is in the elastic range of Hooke's law.

If the wire is stretched under tension  $\tilde{T}$  and has a shape  $y(x)$ , the force  $F_t$  acting tangentially on an infinitesimal part of the wire between  $x$  and  $dx$  is given by:

$$\mathcal{F}_t(x)dx = \tilde{T}\left(\frac{dy}{dx}\right)_{x+dx} - \tilde{T}\left(\frac{dy}{dx}\right)_x = \tilde{T}\frac{d^2y}{dx^2}dx. \quad (3.6)$$

$\mathcal{F}_t dx$  is the force that tends to restore the wire back to its nominal position and balances any external applied force. The gravitational and electrostatic forces per unit length acting on the wire are

$$\begin{aligned} \mathcal{F}_B &= g\rho\sigma, \\ \mathcal{F}_E &= \lambda E, \end{aligned} \quad (3.7)$$

where  $\rho$  is the density of the wire,  $\sigma$  its cross section,  $\lambda$  is the charge per unit length and  $E$  the electric field generated by the surrounding electrodes. If the field is constant, it creates a constant force per unit length, similar to the gravitational one. For a wire placed in a position of electrostatic equilibrium, a small deviation from this position generates a force acting on the wire tending to displace it. This force has the form

$$\mathcal{F}_E = \frac{V^2}{2} \frac{dC}{dy}, \quad (3.8)$$

where  $V$  is the potential of the wire and  $dC/dy$  the variation of its capacitance per unit length due to displacement. It can be shown [Blu93] that

$$\mathcal{F}_E \simeq \frac{V^2}{2} \frac{4\pi\epsilon_0}{[a \ln(a/r)]^2} y = ky, \quad (3.9)$$

where  $r$  is the radius of the wire,  $a$  the typical distance of the wire from the other electrodes and  $\epsilon_0$  the permeability. Thus, the equation describing the equilibrium position of the wire is

$$\tilde{T} \frac{d^2 y}{dx^2} = -ky - g\rho\sigma = f(x), \quad (3.10)$$

with boundary conditions  $y(0) = y(L) = 0$ . For  $k = 0$  we can study separately the effect of gravity. In this case the sagitta of the wire is

$$s_g = y(L/2) = \frac{L^2 g \rho \sigma}{8 \tilde{T}} \quad (3.11)$$

and is inversely proportional to the mechanical tension  $\tilde{T}$ . If  $\tilde{T}$  is increased, the effect is reduced but it cannot be arbitrarily increased, since non-elastic deformations take place. The total sagitta of the wire under the combined effect of electrostatic and gravitational forces is

$$s = y(L/2) = \frac{8s_g \tilde{T}}{L^2 k} \left( \frac{1}{\cos \sqrt{k/\tilde{T}}(L/2)} - 1 \right) = s_g \frac{2}{q^2} \left( \frac{1}{\cos q} - 1 \right) \quad (3.12)$$

with  $q = \sqrt{k/\tilde{T}}(L/2)$ . Plotting the function  $f(q) = (2/q^2)(1/\cos q - 1)$  (see Fig. 3.10), it becomes clear that the electrostatic forces amplify the sagitta produced by the

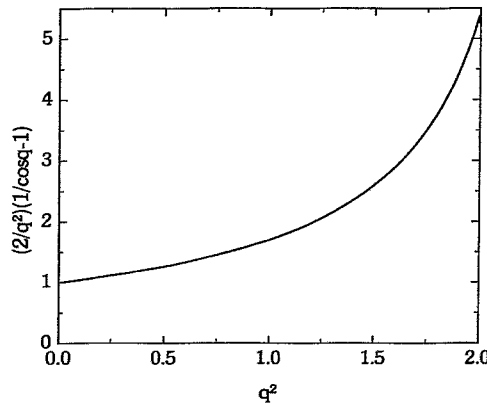


Figure 3.10: Amplification factor of the gravitational sagitta, owing to electrostatic forces.

gravitational forces. When  $q$  approaches  $\pi/2$  the amplification factor diverges and the position of the wire is no longer stable. From Eq. (3.9) the stability condition

$$q^2 = \frac{4\pi\epsilon_0}{[a \ln(a/r)]^2} \frac{V^2 L^2}{2\tilde{T} 4} \leq 1 \quad (3.13)$$

can be deduced. Using this inequality, it is possible to calculate the critical tension  $\tilde{T}_c$ , below which the wires oscillate under working conditions. Choosing, for example,  $a = 4$  mm,  $L = 2$  m and  $V = 2000$  V, we get the  $\tilde{T}_c$  values depicted in Tab. 3.1. For shorter wires the critical tension is lower.

wire	radius ( $\mu\text{m}$ )	$\tilde{T}_c$ (N)	strung $T$ (N)	material
sense	10	0.31	0.5	W
cathode	40	0.65	1.0	Al
field	50	0.72	1.5	Al

Table 3.1: Critical tension values for different wires of MDC III.

### 3.8 Numerical Calculation of Wire Sagittas

Whether the solution of the differential Eq. (3.10) is exact or not depends on the shape of  $f(x)$ . If it is chosen to have a linear or second order dependence from  $y(x)$ , simple analytic solutions can still be found. For higher order terms though, numerical methods are needed to compute the wire shape. Such a method may consist of the following steps:

- ⇒ select the sample points and compute the sagitta and its first derivative for the linear force,
- ⇒ prepare an interpolation table of the force for various shifts,
- ⇒ use the 5<sup>th</sup> order Runge-Kutta-Nyström stepping method for calculating a solution between the sampling points,
- ⇒ perform the Newton-Raphson zero search to minimize the difference between the solution on the left and the right side of the sampling points, as well as the difference between the first derivatives at the same points (see Figs. 3.11 and 3.12).

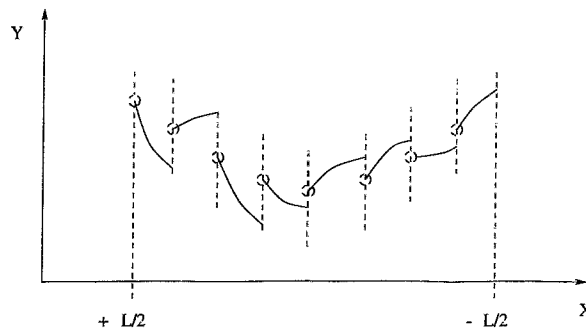


Figure 3.11: Scheme of extrapolation of the solution using a stepping method between the sampling points.

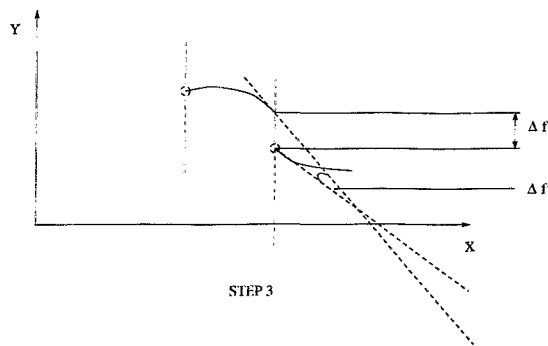


Figure 3.12: Scheme of the zero search of  $\Delta f$  and  $\Delta f'$ .

### 3.9 Examination of the Wire Deflections for the MDC III

Following the above we attempted to calculate the saggitas for the wires of MDC III as a function of their tension, without varying the potential applied on field and cathodes. The wires might lose tension by creeping out of the Araldite glue on the Stesalit frame. In case a wire is loose enough to affect the resolution of the chamber – this applies to sense wires – it is possible to make corrections by knowing the size of the deflection along the wire.

The calculation was performed for a series of tension values between the strung and the critical one and for different layers and chamber orientations. The results for operational high voltage  $V_{cathode} = V_{field} = -2000$  V are depicted in Figs. 3.13, 3.14 and 3.15. The plots show that sense and field wires of the  $0^\circ$  layer are subject to the highest deflection from the nominal position. The situation is better for inclined layers and chambers. Nevertheless, for a loss of 20% in tension the sagitta never exceeds the resolution of the modules ( $100 \mu\text{m}$ ), e. g. for 0.4 N the sagitta of  $0^\circ$  layer

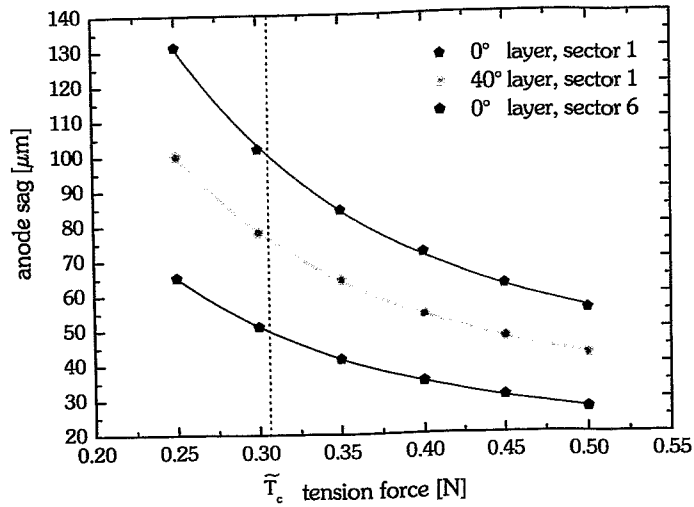


Figure 3.13: Deflection of sense wires as a function of their tension. For the nominal tension of 0.5 N, the calculated sagitta is far below the resolution of the chambers.

in sector 1 is below 80  $\mu\text{m}$ .

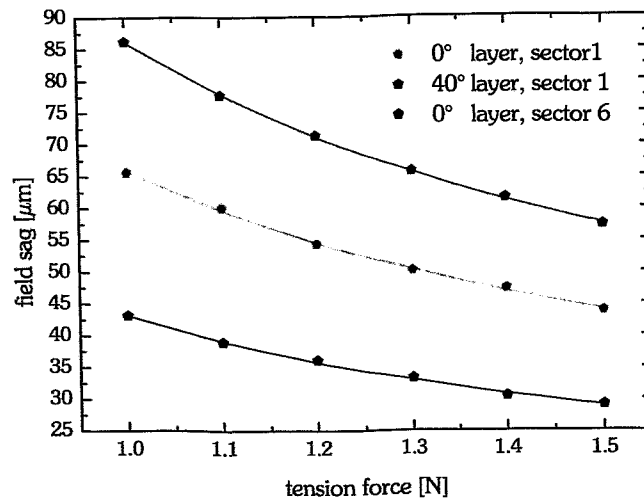


Figure 3.14: Deflection of field wires as a function of their tension. As in Fig. 3.13, the nominal tension assures that the deflection is not of great importance and does not dramatically influence the resolution of the detector.

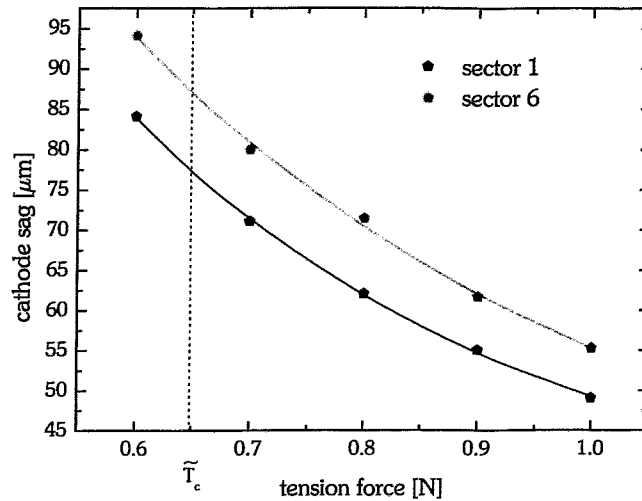


Figure 3.15: Deflection of cathode wires as a function of their tension.

### 3.10 Malfunction Symptoms of the MDC and Repair

Of specific interest in this section are observations of contamination of filament growth in one of the chambers that has been used in-beam. The module worked successfully for three weeks during data taking in November 2001 (C+C at 2 AGeV and average intensity of about  $10^6$  particles per spill), as well as during the later spring cosmics run for a few days. As a first sign of malfunction, the operating high voltage could not be applied, indicating a short-circuit to ground involving the first anode and first cathode layer.

An in-situ measurement lead to the following observations:

- ⇒ a low value of resistivity between the first field and the first cathode layer,
- ⇒ one anode wire that – via its low impedance preamplifier – connected the whole cathode plane to ground. Disconnecting this specific wire from the readout electronics lead the current in the chamber back to normal values.

A thorough investigation of both problems required the opening of the chamber. Concerning the contact of the two layers, a loose wire in the first cathode layer was found to be responsible. This wire had slipped out of the glue having a sagitta large enough to approach the neighboring anode layer (the distance between two layers is 4 mm). The tension measured was 0.14 N, far below the nominal value (1 N) and the critical one (0.65 N). While operating the chamber with high voltage, the electric field increases the displacement of the cathode wire, reducing its distance to

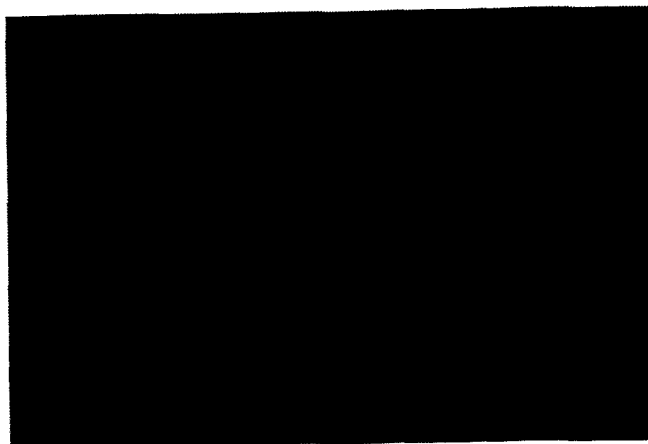


Figure 3.16: Photo of a filament taken with microscope. The straight black line is a part of an anode wire with a diameter of  $20\ \mu\text{m}$ .

the anode layer. As a result, two neighbouring layers made contact and the short-circuit appeared.

Moreover and independent of the cathode wire, white filaments were found to have spread over the surface of the first anode layer. Their diameter varied from 2 to  $50\ \mu\text{m}$  and their length could be as large as 12 cm, growing across 20 wires. One of them was strong enough to keep the aforementioned anode wire (observation 2) dislocated and connected to its neighboring field wire. A typical photograph of such a filament, taken with a microscope, is shown in Fig. 3.16. For the investigation steps that were taken to clarify the reasons for these symptoms, see the dedicated publication [Kan04].

The loose cathode wire was eventually replaced. Apart from that, the anode wire that had been found to be displaced by the filaments, showed no tension loss after removing the filaments. These two wires have no geometrical overlap and are far from each other. It is difficult to estimate the extent to which the anode wire was contributing to the short-circuit in addition to the cathode wire. No data on the conductivity of the filament could be collected, as the sample was exhausted after the spectroscopical investigation. A possible connection between the cathode layer and this wire has not been observed when inspecting the interior of the chamber.

Infrared spectra suggested that one possible source of the filaments might have been cellulose containing tissue material used in the production process, although the spectra do not fully match. In particular, silicon traces are problematic to explain. Silicon is a component in the material of the frames, as well as in the glue used to hold the wires. A possible scenario could be that some leftover of the tissue was contaminated with silicon of either source and slipped into the active area of the module. Such a mixture has low conductivity but while operating the chamber, it can be modified by local discharges. The process of carbonization can increase the surface conductivity of organic substances in plasma and arc up to 15 orders of magnitude and reach values of about  $1\ \Omega/\text{cm}$  [Odz98]. This could partially explain

the difference between the filament and the tissue spectral lines. It is very unlikely though, that these structures are dose related aging phenomena. The aging tests performed, as well as the absence of such filaments in several other modules that had to be opened, supports this claim [Gar98]. Moreover, none of these symptoms can be related to the natural tension reduction of the wires over time.

After the removal of the filaments, the replacement of the loose wire and the careful cleaning of the detector components, the module could be normally operated under beam conditions and the regular operation of the HADES experiment could be resumed.

## 4 Reconstruction of $\Lambda$ Hyperons

The stable operation of the drift chambers is an important prerequisite for a smooth data acquisition and a subsequent successful physics analysis. In this chapter the  $\Lambda$  hyperon reconstruction using HADES data is presented. The data taking under investigation took place in November 2002 and during its four weeks, approximately  $240 \cdot 10^6$  events were collected. However, the final amount of usable events was reduced to  $160 \cdot 10^6$ , as only files with high magnetic field (magnet current = 2500 A) and proper detector calibration were included in the analysis.

The system under investigation is C+C at a kinetic beam energy of 2 AGeV. The carbon target consists of two segments at a distance of 20 mm, whose diameter and thickness are 3 mm and their density  $2.15 \text{ g/cm}^3$ . A double target enables a high interaction probability (around 5%) by reducing the absorption of the reaction products in the material and the multiple scattering. The beam intensity varied between  $1\text{-}2 \cdot 10^6$  particles per spill.

The experiment was conducted with a mixed first level trigger (LVL1) requiring at least four charged particles per event on the TOF and TOFino walls for 85% of the events, and two charged particles in 15% of the events. In this way, more central collisions are selected, which correspond to about 70% of the geometrical cross section.

The second level trigger (LVL2) required at least one lepton candidate in the event and the recording of the data was done in such a way that from the total statistics, 56% were LVL1 events and 44% were LVL2 events. Moreover, a certain fraction of LVL1 events, the so-called downscaled events, were recorded regardless of the LVL2 trigger decision for trigger control and normalization purposes. In November 2002 the downscaling factor was 10, meaning that every 10<sup>th</sup> event was recorded without taking the LVL2 trigger decision into consideration. Since leptons were of no interest for this analysis, the information from the RICH and the Pre-Shower detectors was not used.

### 4.1 Properties of $\Lambda$ Hyperons

$\Lambda$  baryons are strange particles with a *uds* constituent quark content. Some of their basic properties are summarized in Tab. 4.1. Due to strangeness conservation in strong interaction processes a  $\Lambda$  is always created together with another strange particle containing an  $\bar{s}$  quark, like  $K^+$  or  $K^0$ . Such an example for an elementary

$p+p$  reaction is depicted in Fig. 4.1.

mass	$m_\Lambda = 1115.683 \pm 0.006 \text{ MeV}$
mean life	$\tau = (2.632 \pm 0.020) \times 10^{-10} \text{ s}$
decay length	$c\tau = 7.89 \text{ cm}$
baryon charge	$B = +1$
strangeness	$S = -1$
Coulomb charge	$Q = 0$
$\Lambda \rightarrow p\pi^-$	$\text{BR} = (63.9 \pm 0.5)\%$
$\Lambda \rightarrow n\pi^0$	$\text{BR} = (35.8 \pm 0.5)\%$

Table 4.1: Main properties of  $\Lambda$  hyperons [PDG].

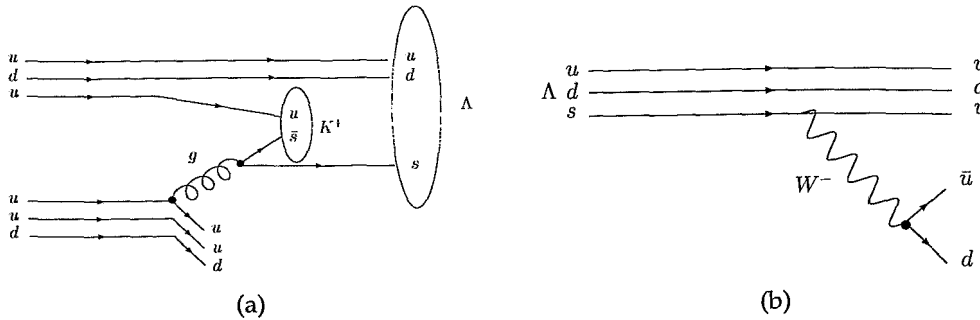


Figure 4.1: (a) Feynman diagram for  $\Lambda$  production in a  $p+p$  reaction. The total strangeness is conserved, therefore the  $\Lambda$  production is always associated with the creation of an  $\bar{s}$  containing particle, in the depicted example a  $K^+$ . (b) The decay  $\Lambda \rightarrow p\pi^-$  with a branching ratio of 64%.

The large branching ratios give good confidence that the particle can be found in the amount of available experimental data. Moreover, the weak decay with the long life time of the order of  $10^{-10} \text{ s}$  ensures that  $\Lambda$  survives long enough to create a secondary vertex outside the target area and in front of the inner tracking system, facilitating in this way the rejection of the background contributions.

## 4.2 Detector Acceptance and Resolution

Since HADES can only register signals of charged particles, the focus is on the decay  $\Lambda \rightarrow p\pi^-$  with a branching ratio of 64%. At the time of the experiment under study the spectrometer setup was the following (see Fig. 4.2):

- ⇒ two sectors fully equipped with MDC modules offering high momentum resolution,

- ⇒ two sectors equipped with one outer MDC offering middle resolution,
- ⇒ two sectors only with inner modules offering low resolution.

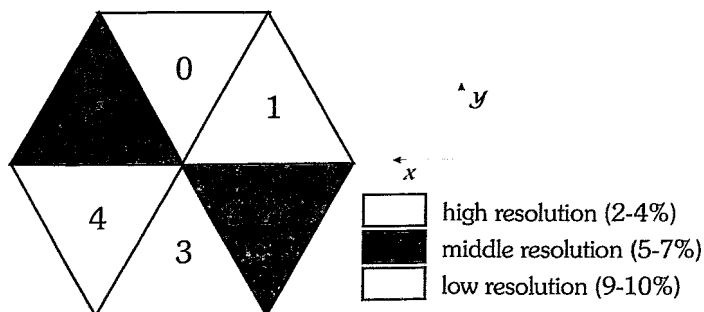


Figure 4.2: Enumeration of the HADES sectors with corresponding momentum resolution.

The  $\Lambda$  reconstruction is done via its invariant mass

$$m_{inv} = \sqrt{(E_p + E_{\pi^-})^2 - (\vec{p}_p + \vec{p}_{\pi^-})^2}. \quad (4.1)$$

The variables that contribute to the equation are the momenta of the decay products  $p$  and  $\pi^-$  and the opening angle of their direction vectors at the decay vertex. So, the parameters that set the constraints of the analysis are the detector acceptance of the  $p\pi^-$  pairs, the momentum and the angular resolution, defining the mass resolution, as well as the primary and secondary vertex reconstruction, providing the tools for background rejection.

The  $\Lambda$  has a long lifetime and a narrow width. Moreover, there is no other known physics process that can lead to the creation of a correlated  $p\pi^-$  pair outside the target area ( $\Delta$  is broad and decays strongly inside the fireball). The  $\Lambda$  signal in the invariant mass spectrum should then appear as a sharp peak sitting on a smooth background attributed to uncorrelated  $p\pi^-$  combinations. Although an off-vertex particle analysis with the low resolution sectors is feasible (see  $K^0$  results in [Zum05]), our interest is to employ the high resolution abilities of the spectrometer in order to increase the purity, which is very important for weak signals. For this reason, the two low resolution sectors (1 and 4) together with one of the medium resolution ones (5)<sup>†</sup> are excluded from the current analysis of the present work.

Reducing the full setup to three sectors, the HADES geometrical acceptance for the  $\Lambda$  decay products decreases from 22% to 7%. Within this acceptance, the transverse momentum vs. rapidity ( $p_t$  vs.  $y$ ) distributions for  $p$  and  $\pi^-$  give an idea about the phase space coverage of the spectrometer (see Fig. 4.3). The theoretical model used as event generator is UrQMD\* (see Appendix A.2). Some of the  $\Lambda$  particles are emitted with an angle below  $15^\circ$  but still can be seen by the detector, as the decay products hit one of sectors 0, 2, 3. The distribution of these  $p$  and  $\pi^-$  hits in

<sup>†</sup>In the analyzed experiment sector 5 had two drift layers switched off due to malfunction symptoms.

\*Ultra relativistic Quantum Molecular Dynamics

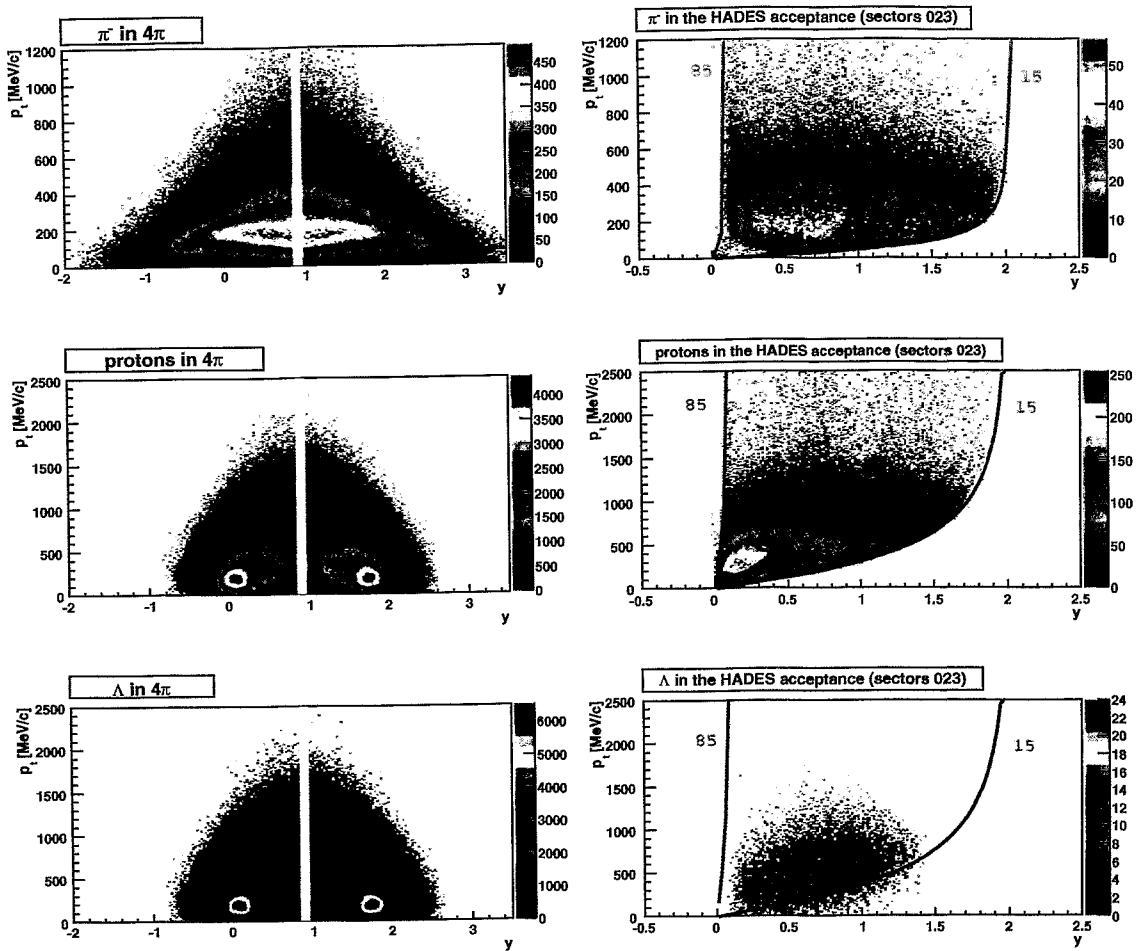


Figure 4.3: Transverse momentum vs. rapidity ( $p_t$ - $y$ ) distributions for  $p$ ,  $\pi^-$  and  $\Lambda$  in  $4\pi$  acquired with UrQMD (left column) and inside the HADES acceptance (right column). The red lines set the polar angle limits of the spectrometer between  $15^\circ$  and  $85^\circ$ . The yellow bar on the left represents the midrapidity region. In the bottom right pad some of the  $\Lambda$  particles emitted with an angle lower than  $15^\circ$  still can be seen by the detector, as their decay products hit sectors 0, 2 or 3. The opposite situation is more usual to happen; a  $\Lambda$  vector emitted within the geometrical acceptance with one or two decay products being outside.

sectors 0, 2, 3 is depicted in Fig. 4.4. Most of the combinations end up in the same sector, which explains why the opening angle distribution does not extend beyond  $100^\circ$  (right pad of Fig. 4.4).

The momentum resolution in simulations for the two particle species is depicted in Fig. 4.5. The two-dimensional plots point out that the particle momenta are underestimated in the reconstruction procedure – in particular protons – as there is no energy loss correction applied in the target, the RICH radiator and the RICH carbon shell. As a consequence, the momentum resolution worsens at low values

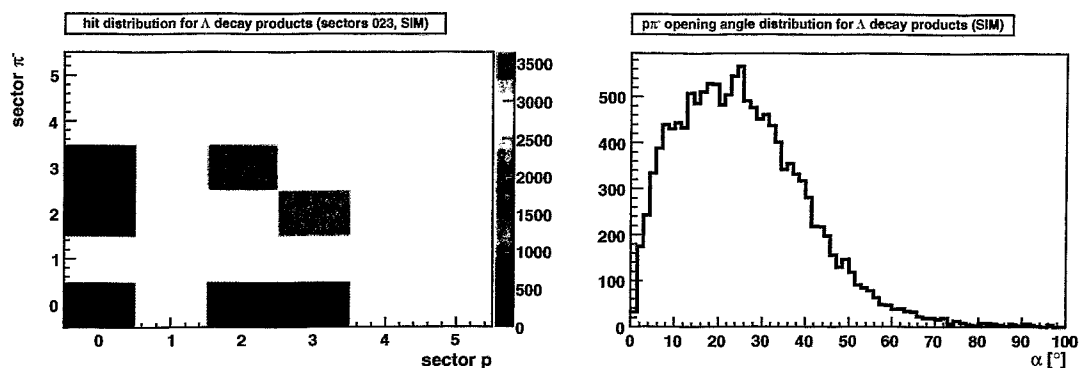


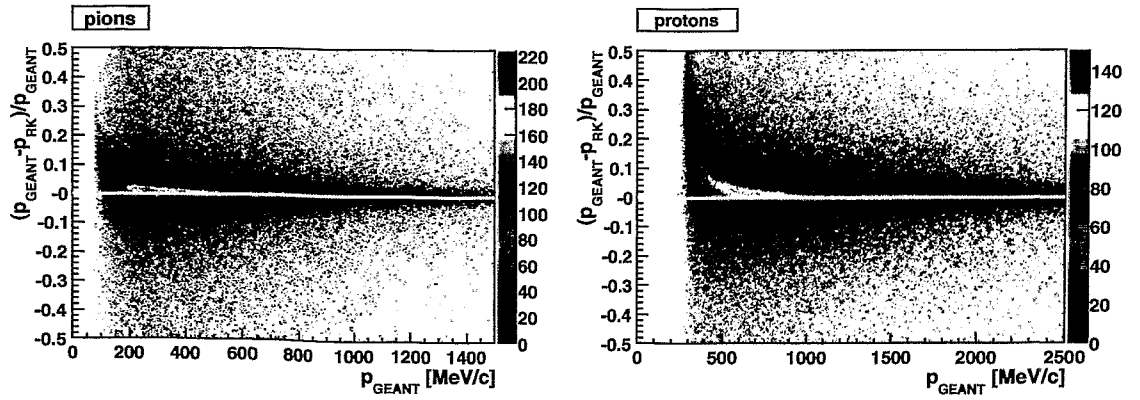
Figure 4.4: Hit distribution of reconstructed  $p$  and  $\pi^-$  tracks coming from a  $\Lambda$  decay (left). Opening angle distribution for the same pairs (right). The unit of the y-axis is counts [a.u.].

(see Fig. 4.5(c)) but at higher momenta it remains stable at the region populated by the decay products (around 2-3% for  $\pi^-$  and 2-5% for  $p$ ). Multiple scattering for protons is also important for momenta lower than 300 MeV. Multiple scattering is of statistical nature, therefore it smears the momentum resolution, an effect that cannot be corrected. In average it enlarges the opening angle of a pair, leading to small systematic errors in the reconstructed  $\Lambda$  mass.

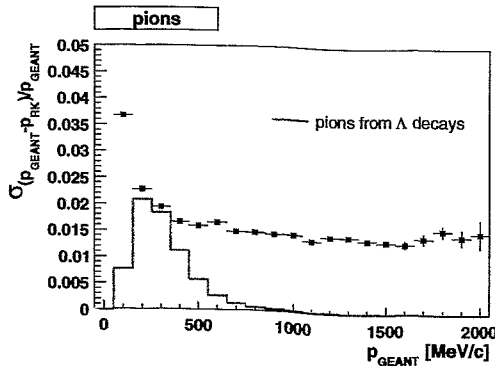
The position resolution of the primary and secondary vertices of the  $\Lambda$  is expected to influence the analysis the most, especially since there is no vertex detector involved in the analysis. The primary vertex is calculated with tracks from all sectors, for events that contain at least one  $p$  and one  $\pi^-$ . The calculation is repeated as many times as there are  $p\pi^-$  combinations. To exclude autocorrelation effects, the  $p\pi^-$  pair of interest is excluded every time from the sample of tracks used for the vertex estimate. Tukey weights [San03] are applied to all tracks, in order to reduce the impact of outliers \*, either because of scattering or because they originate from a  $\Lambda$  decay.

The  $\Lambda$  secondary vertex distributions along the  $x$  and the  $y$  axes are broad and asymmetric. Along the  $z$  coordinate the two targets are no longer visible in the reconstructed data. Plotting the distribution of the decay points taken directly from HGeant [Gea04] without applying Hydra [Hyd04], the HADES analysis software package, we conclude that this is not a bias of the reconstruction algorithm but it is rather related to the geometrical acceptance of the  $\Lambda$  in the laboratory system (see Fig. 4.6).

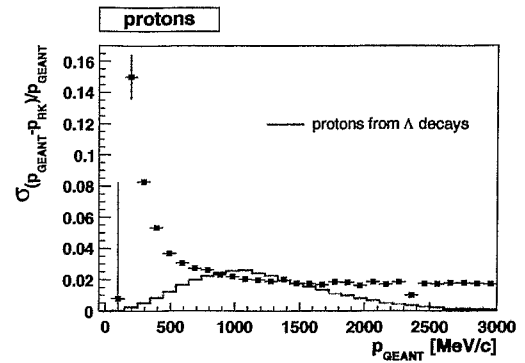
\*Particle tracks that lie far from the target.



(a) Two-dimensional view of the momentum shift for all pions and protons in simulation.  $p_{\text{GEANT}}$  stands for the momentum which the particle is produced with in simulation, while  $p_{\text{RK}}$  is the momentum reconstructed with the Runge-Kutta method of Hydra. The momentum shift in low momenta is due to the absence of the energy loss correction.



(b) Momentum resolution for  $\pi^\pm$ .



(c) Momentum resolution for  $p$ .

Figure 4.5: Momentum shift and momentum resolution for all  $\pi^\pm$  and  $p$  in simulation. In these plots only sectors 0, 2, 3 have been taken into account, i. e. two sectors with high (0, 3) and one with middle resolution (2). The momentum distributions of  $p$  and  $\pi^\pm$  are presented in arbitrary scaling.

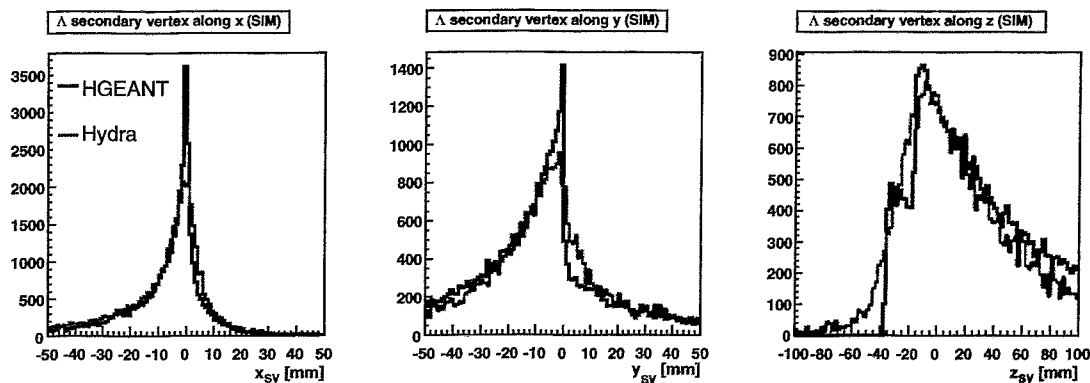


Figure 4.6: Secondary vertex distributions of  $\Lambda$  decays in HGeant and Hydra. The asymmetric shapes in  $x$  and  $y$  do not appear after the reconstruction but already at the HGeant level. The second target looks more pronounced because it is superimposed on the distribution of the first one (rightmost pad). The histograms are normalized to the same integral value. The units of the  $y$ -axes are counts [a.u.].

### 4.3 Particle Identification

There have been various tracking algorithms developed and used in the HADES analysis software for the track reconstruction [San03, Rus06]; the method employed for the following results is the Runge-Kutta numerical solution of the equation of motion for a charged particle whose trajectory traverses the HADES toroidal magnetic field [Abr64, Bug81, Sad06]. From the curvature of the track it is possible to calculate the particle momentum  $p$ , as explained in section 2.5.1. Knowing the length of the flight path and having measured the time of flight, the calculation of the particle velocity  $\beta$  follows. Plotting  $\beta$  as a function of  $p$  allows the identification of  $p$  and  $\pi^-$ . This is done by means of a graphical cut, adjusted differently for every sector and system (see Fig. 4.7).

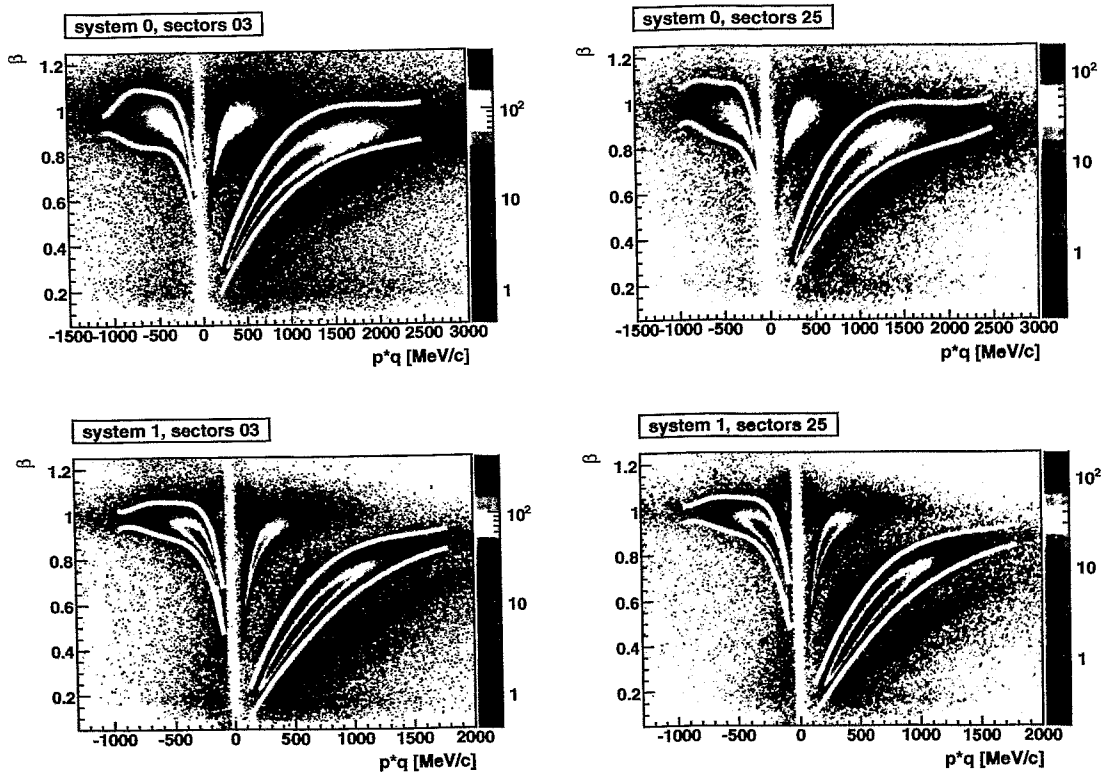


Figure 4.7: Distribution of velocity  $\beta$  vs. momentum multiplied with the particle charge in real data for different sectors and systems (TOF: system1, TOFino: system0). The white lines indicate the applied graphical cut for the identification of  $p$  and  $\pi^-$  (positive and negative momenta, respectively). The early stage of the analysis is kept general, that is why sector 5 (low resolution) is still included in the graphical cut.

To get some confidence about this graphical cut, it is useful to calculate its effi-

ciency  $\mathcal{E}_{grCut}$ . The latter can be defined as

$$\mathcal{E}_{grCut} = \frac{N(\text{graphically identified with correct ID})}{N(\text{with correct ID in simulation})}, \quad (4.2)$$

where  $N$  denotes the number of particles identified in simulation under the conditions stated in the brackets. The result is presented in Fig. 4.8. The efficiency for  $\pi^-$  is above 90% and for  $p$  above 95% for the range of interesting momenta, values that do not bias the further analysis.

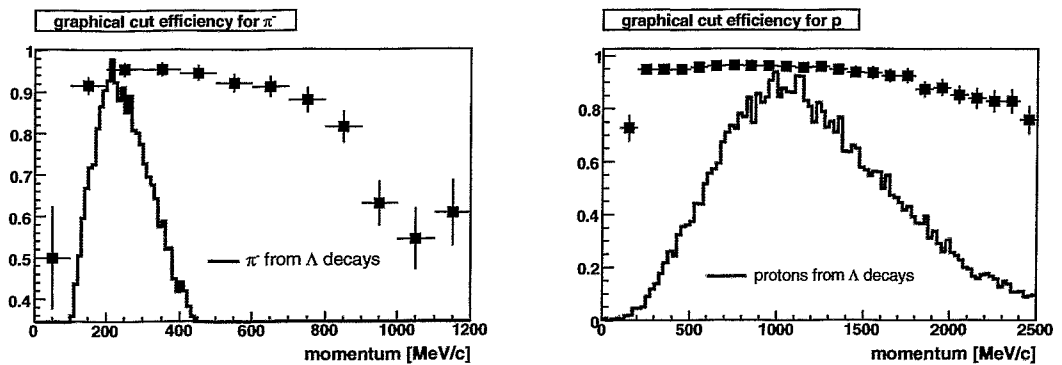


Figure 4.8: Graphical cut efficiency for  $\pi^-$  and  $p$  (black squares). The average values are above 90% for  $\pi^-$  and above 95% for protons in the region where the momenta of the decay products lie, depicted by red histograms with arbitrary scaling.

## 4.4 Particle Correlations and Signal Enhancement

Once  $p$  and  $\pi^-$  are identified, the next step is to correlate them into pairs and calculate the invariant mass of every combination (see Eq. (4.1)). Such an invariant mass distribution is depicted in Fig. 4.9, with the low limit being the sum of the  $p$  and  $\pi^-$  masses. The masses of the particles are taken from the Particle Data Group booklet and not from the reconstructed mass distribution, excluding this way the effect of the time of flight calibration and flight path determination on the particle mass calculation.

Comparing the momentum (see Fig. 4.10) and the opening angle distributions (see Fig. 4.11) for simulated and experimental data, the steeper shape in the latter case can be attributed to the  $\pi^-$  momentum difference. However, the displayed spectra are not conclusive, as they are not corrected for efficiency. Figs. 4.10 and 4.11 are only meant to give a hint about the different shapes of the invariant mass distributions at the early stage of the analysis.

In the smooth invariant mass distribution the  $\Lambda$  signal is buried under a huge combinatoric background. In order to disentangle it, a series of conditions or "cuts"

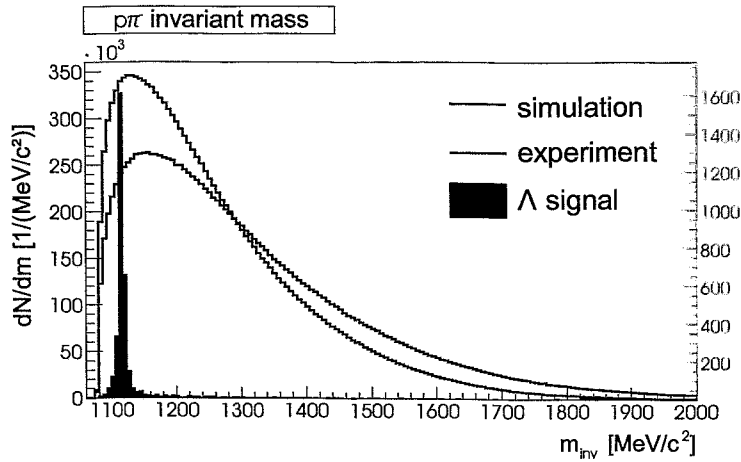


Figure 4.9: Distribution of  $p\pi^-$  invariant mass for all pair combinations in simulation ( $34 \cdot 10^6$  events) and experiment ( $131 \cdot 10^6$  events). The two histograms are normalized to the same integral and are not efficiency corrected. In red depicted is the  $\Lambda$  signal contained in the simulation with its corresponding axis on the right.

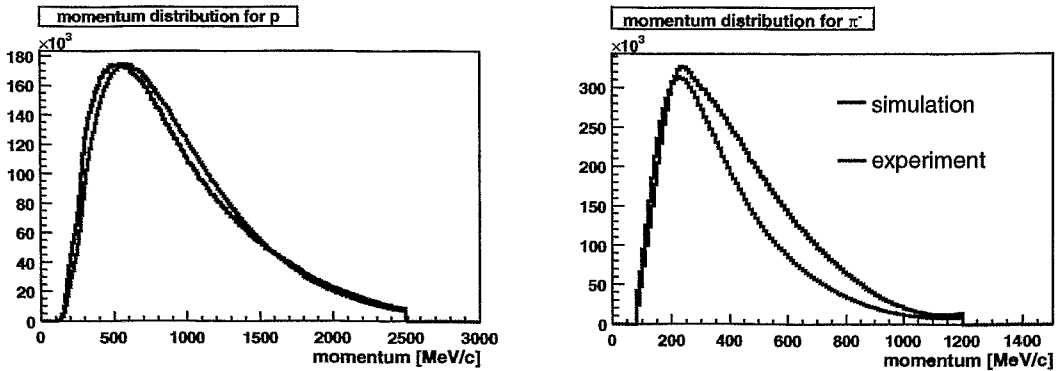


Figure 4.10: Momentum distributions of all  $p$  and  $\pi^-$  in the events for simulation and experiment (not efficiency corrected). The unit of the y-axis is counts [a.u.].

have to be applied to the data. Several variables can be used to enhance the signal of an off-vertex decay, either on the pair properties or on the individual tracks; among them are:

- ⇒ the distance of the secondary vertex ( $\Lambda$  decay point) from the primary vertex,  $|\vec{w}_{SV} - \vec{w}_{PV}|$ ,
- ⇒ the distance  $d$  between the  $p$  and  $\pi^-$  tracks at the secondary vertex,
- ⇒ the distance  $s$  of the sum momentum vector from the primary vertex,

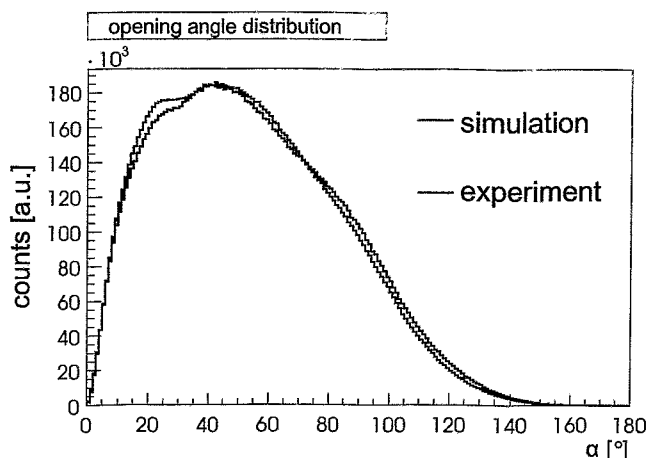
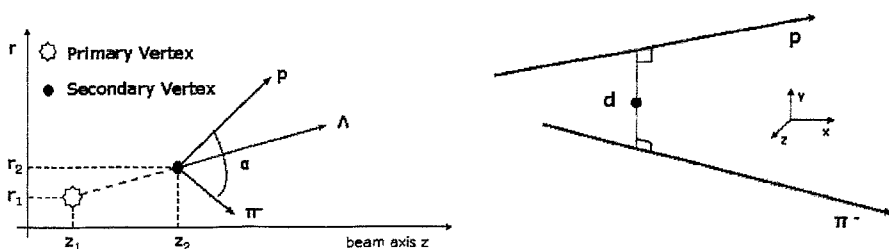
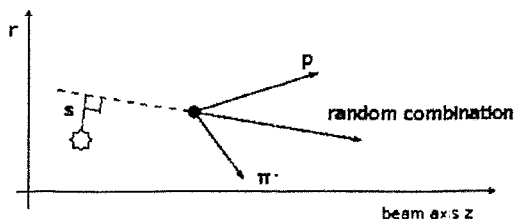


Figure 4.11: Opening angle distribution for  $p\pi^-$  pairs in simulation and experiment without efficiency corrections (sectors 0, 2, 3).

as well as single  $p$  and  $\pi^-$  track properties, like  $\chi^2$  values from the MDC track segment fits or the Runge-Kutta momentum reconstruction. A visualization of the pair variables in three dimensions is attempted in Fig. 4.12. Their way of calculating is explained in Appendices B and C.



(a) Distance between secondary and primary vertex. (b) Distance  $d$  between  $p$  and  $\pi^-$  tracks.



(c) Distance  $s$  of a sum momentum vector from the target.

Figure 4.12: Variables used for  $\Lambda$  signal enhancement.

## 4.5 Signal-to-Background Studies

A systematic study of the signal-to-background ratio as a function of the aforementioned variables can suggest the right values of the cuts for the experimental data.  $\Lambda$  secondary vertices can extend up to several centimeters away from the creation point (see Fig. 4.13). A large fraction of  $\Lambda$  decays at the target and in its vicinity, leading to a signal that is almost impossible to reconstruct because of the large amount of co-produced uncorrelated  $p\pi^-$  pairs from other physical sources. To facilitate the analysis, it is necessary to move far from the primary vertex and reconstruct particles that originate from off-vertex decays.

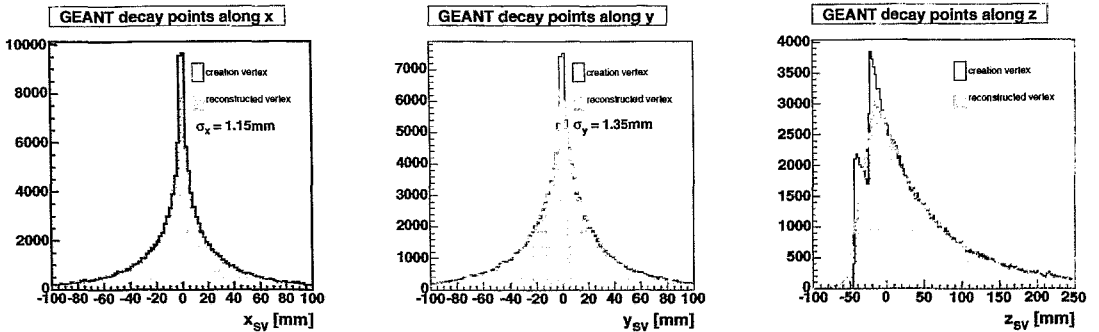


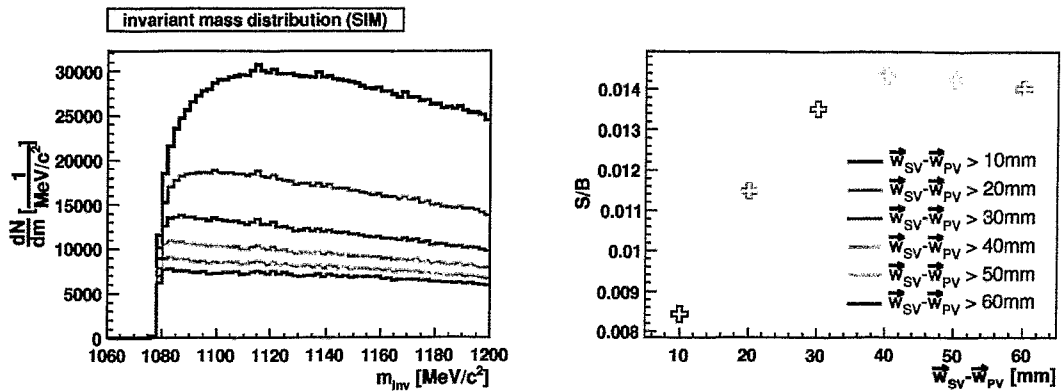
Figure 4.13: The black distribution represents the  $\Lambda$  decay points along the  $x$ ,  $y$  and  $z$  axes. Along the  $z$  axis (beam direction) the two targets can be seen. In red colour depicted are the  $\Lambda$  secondary vertices, which have been reconstructed by the HGeant hit points at the MDC detectors. This is the optimal primary vertex resolution, as there is no reconstruction accuracy involved. Multiple scattering is responsible for the poor resolution of the two targets. The units of the  $y$ -axes are counts [a.u.].

The signal-to-background ratio  $S/B$  as a function of the off-vertex distance is shown in Fig. 4.14. The statistics sample used is  $34 \cdot 10^6$  simulated events, containing the decay products of 3329  $\Lambda$  particles. These  $p$  and  $\pi^-$  have hit sectors 0, 2 or 3, have both inner and outer MDC segments fitted ( $\chi_{seg}^2 > 0$ ) and the Runge-Kutta method has calculated a momentum for the tracks ( $\chi_{RK}^2 > 0$ ).

For coarse steps of 10 mm the efficiency of this condition is calculated and depicted in Tab. 4.2. Studies of the distance projection on cylindrical coordinates  $r$  and  $z$  are also presented, so that the most sensitive variable can be selected. From the values of  $S/B$ , it seems that the  $z$  coordinate (see rightmost column of Tab. 4.1(c)) has increased the significance of the signal more than the others. In order to keep the efficiency reasonably high (43.7%) and to let space for additional conditions, the value  $z_{SV} - z_{PV} > 30 \text{ mm}^*$  is selected as a starting point.

This condition alone is not sufficient to make the signal emerge clearly from the background. An additional helpful quantity is the distance  $d$  between the  $p$  and

\*PV stands for primary vertex and SV for secondary vertex.



(a) Invariant mass distribution and S/B ratio as a function of the off-vertex distance.

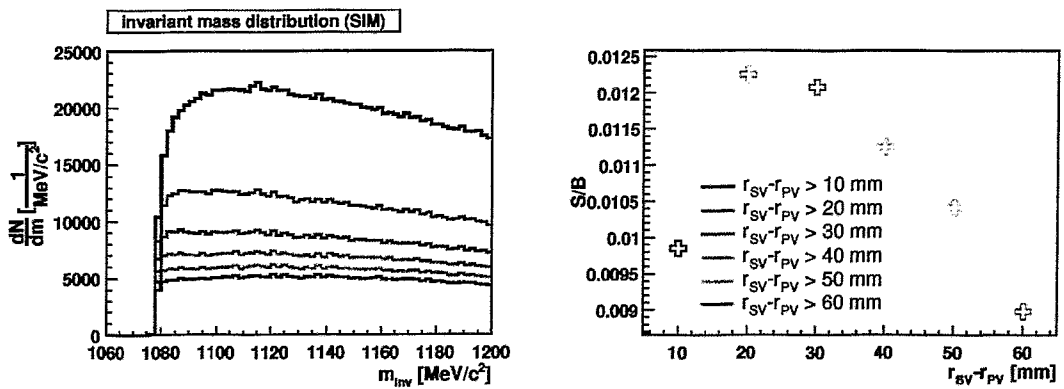
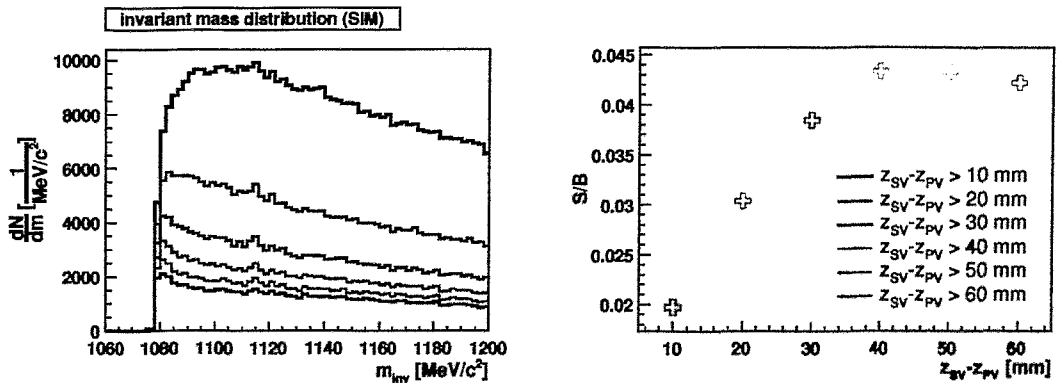
(b) Invariant mass distribution and S/B ratio as a function of the distance projection on  $r$ .(c) Invariant mass distribution and S/B ratio as a function of the distance projection on  $z$ .

Figure 4.14: Invariant mass distribution (left column) and S/B ratio (right column) as a function of the varying off-vertex distance and the projections of this quantity on cylindrical coordinates  $r$  and  $z$ .

(a)  $S/B$  ratio for the distance between primary and secondary vertex.

$ \vec{w}_{SV} - \vec{w}_{PV} $ [mm]	# $\Lambda$	cut efficiency (%)	$S/B (\times 10^{-2})$
–	3329	100.0	–
10	2971	89.2	0.80
20	2515	75.5	1.15
30	2120	63.7	1.35
40	1795	53.9	1.43
50	1527	45.9	1.43
60	1314	39.5	1.40

(b)  $S/B$  ratio for the distance projection on the  $r$  coordinate.

$r_{SV} - r_{PV}$ [mm]	# $\Lambda$	cut efficiency (%)	$S/B (\times 10^{-2})$
–	3329	100.0	–
10	2571	77.2	1.00
20	1894	56.9	1.23
30	1416	42.5	1.21
40	1088	32.7	1.13
50	861	25.9	1.04
60	676	20.3	0.90

(c)  $S/B$  ratio for the distance projection on the  $z$  coordinate.

$z_{SV} - z_{PV}$ [mm]	# $\Lambda$	cut efficiency (%)	$S/B (\times 10^{-2})$
–	3329	100.0	–
10	2208	66.3	1.97
20	1796	53.9	3.04
30	1454	43.7	3.85
40	1188	35.7	4.34
50	961	28.9	4.33
60	775	23.3	4.22

Table 4.2:  $S/B$  ratio and corresponding efficiency for the off-vertex distance. The projection on the  $z$  axis seems to be the most sensitive variable for the  $\Lambda$  signal enhancement.

$\pi^-$  tracks before the magnet. Keeping the condition  $z_{SV} - z_{PV} > 30$  mm, the same study like before is repeated, this time reducing the variable  $d$  in steps of 10 mm (see Fig. 4.15 and Tab. 4.3). The  $\Lambda$  signal has started poking out of the background.

Keeping  $d < 12$  mm and  $z_{SV} - z_{PV} > 30$  mm, the next study concerns the distance  $s$  of the sum momentum vector from the primary vertex. In case of a  $\Lambda$  decay the sum vector of  $p$  and  $\pi^-$  should originate from the vicinity of the target. The

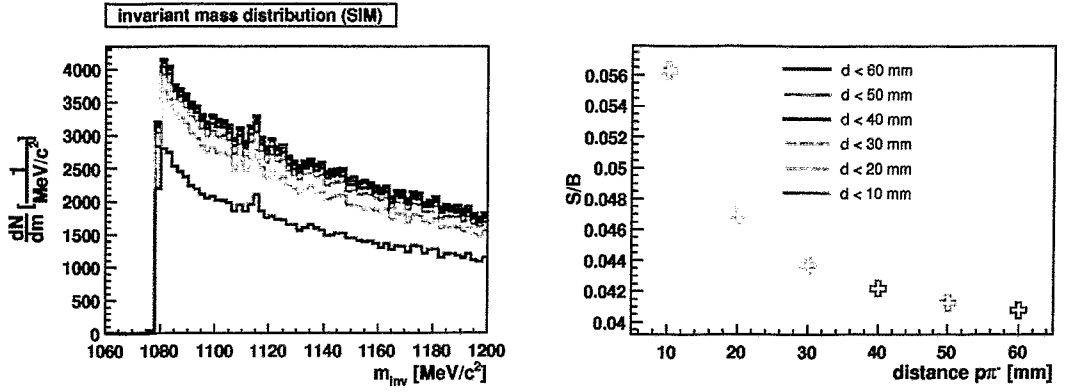


Figure 4.15: Invariant mass distribution and  $S/B$  ratio as a function of the  $p\pi^-$  distance  $d$  with the condition  $z_{SV} - z_{PV} > 30$  mm. As  $d$  decreases, the signal increases with respect to the background, since uncorrelated  $p\pi^-$  pairs with large distance between them are rejected.

distance $d$ [mm]	# $\Lambda$	cut efficiency (%)	$S/B (\times 10^{-2})$
60	1439	43.2	4.07
50	1436	43.1	4.13
40	1432	43.0	4.22
30	1419	42.6	4.37
20	1373	41.2	4.70
10	1168	35.1	5.63

Table 4.3:  $S/B$  ratio and corresponding efficiency for the  $p\pi^-$  distance  $d$  with the condition  $z_{SV} - z_{PV} > 30$  mm.

reduction of this value should increase the significance of the  $\Lambda$  signal. However, Fig. 4.16 and Tab. 4.4 show a rather flat tendency. This variable is inappropriate and insensitive for this analysis; a very loose upper value of  $s < 150$  mm is selected.

impact parameter $s$ [mm]	# $\Lambda$	cut efficiency (%)	$S/B (\times 10^{-2})$
180	1246	37.4	5.35
150	1229	36.9	5.43
120	1189	35.7	5.43
90	1116	33.5	5.45
60	942	28.3	5.48
30	592	17.8	5.40

Table 4.4:  $S/B$  ratio and corresponding efficiency for the impact parameter  $s$  with the conditions  $d < 12$  mm and  $z_{SV} - z_{PV} > 30$  mm.

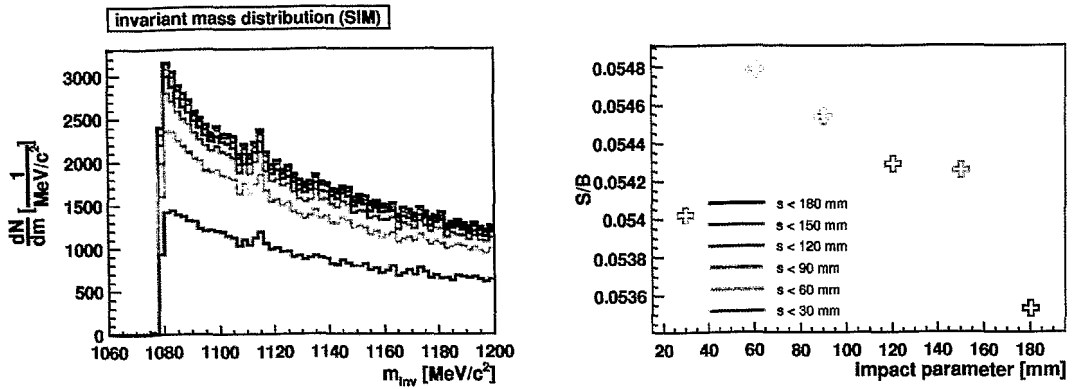


Figure 4.16: Invariant mass distribution and S/B ratio as a function of impact parameter  $s$  with the conditions  $d < 12$  mm and  $z_{SV} - z_{PV} > 30$  mm.

The reason for this behaviour is explained in Fig. 4.17. In the left pad, after the off-vertex condition is applied (marked in red), the distribution of the  $p\pi^-$  distance  $d$  still has a low average value, while the distribution of the impact parameter  $s$  is a lot flatter. Consequently, the reduction of  $s$  does not bring the desirable result on the S/B ratio.

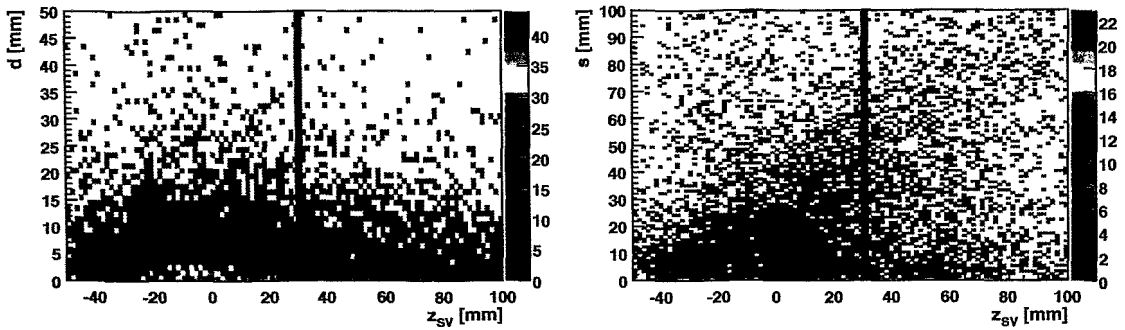


Figure 4.17: Correlation of off-vertex distance cut along the  $z$  coordinate with the parameters  $d$  and  $s$ . Only pairs of  $\Lambda$  decay products are included in the figures.

To further increase the S/B ratio, it is useful to demonstrate the effect of various  $\chi^2$  solely on the single  $p$  and  $\pi^-$  tracks. A certain upper limit should be applied to these values, in order to discard badly reconstructed trajectories. Keeping the previous cuts at the selected values, the S/B ratio is once again displayed for three  $\chi^2$  values, independently from each other: the inner MDC segment  $\chi^2$ , the outer MDC segment  $\chi^2$  and finally the  $\chi^2_{RK}$  (see Figs. 4.18, 4.19, 4.20 and Tabs. 4.5, 4.6, 4.7) from the Runge-Kutta momentum reconstruction. Finally, a combination of these conditions is chosen for the further improvement of the signal quality.

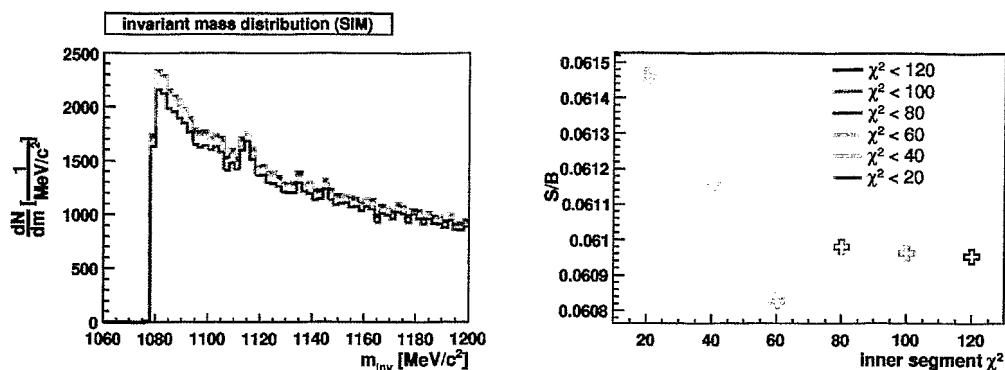


Figure 4.18: Invariant mass distribution and  $S/B$  ratio as a function of inner segment  $\chi^2$  with the conditions  $s < 150$  mm,  $d < 12$  mm and  $z_{SV} - z_{PV} > 30$  mm.

inner segment $\chi^2$	# $\Lambda$	cut efficiency (%)	$S/B (\times 10^{-2})$
120	970	29.1	6.10
100	970	29.1	6.10
80	970	29.1	6.10
60	966	29.0	6.08
40	947	28.4	6.12
20	877	26.3	6.15

Table 4.5:  $S/B$  ratio for the inner segment  $\chi_{seg}^2$  with the conditions  $s < 150$  mm,  $d < 12$  mm and  $z_{SV} - z_{PV} > 30$  mm.

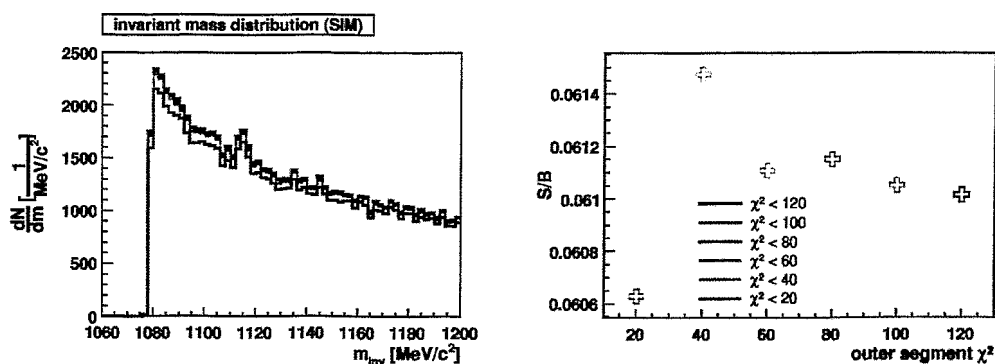


Figure 4.19: Invariant mass distribution and  $S/B$  ratio as a function of outer segment  $\chi^2$  with the conditions  $s < 150$  mm,  $d < 12$  mm and  $z_{SV} - z_{PV} > 30$  mm.

In all three cases, the  $S/B$  ratio and the efficiency are only slightly influenced by the reduction of the  $\chi^2$  variables. The final selection of the simulation cuts in the present analysis is:

outer segment $\chi^2$	# $\Lambda$	cut efficiency (%)	S/B ( $\times 10^{-2}$ )
120	970	29.1	6.10
100	970	29.1	6.11
80	965	29.0	6.12
60	958	28.8	6.11
40	943	28.3	6.15
20	859	25.8	6.06

Table 4.6: S/B ratio for the outer segment  $\chi_{seg}^2$  with the conditions  $s < 150$  mm,  $d < 12$  mm and  $z_{SV} - z_{PV} > 30$  mm.

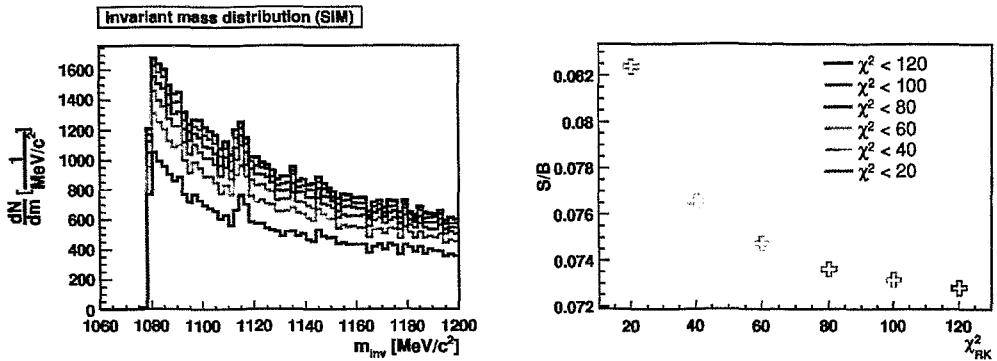


Figure 4.20: Invariant mass distribution and S/B ratio as a function of  $\chi_{RK}^2$  with the conditions  $s < 150$  mm,  $d < 12$  mm and  $z_{SV} - z_{PV} > 30$  mm.

$\chi_{RK}^2$	# $\Lambda$	cut efficiency (%)	S/B ( $\times 10^{-2}$ )
120	713	21.4	7.28
100	683	20.5	7.32
80	649	19.5	7.36
60	606	18.2	7.48
40	542	16.3	7.66
20	444	13.3	8.24

Table 4.7: S/B ratio and corresponding efficiency for  $\chi_{RK}^2$  with the conditions  $s < 150$  mm,  $d < 12$  mm and  $z_{SV} - z_{PV} > 30$  mm.

- ⇒  $z_{SV} - z_{PV} > 30$  mm,
- ⇒  $d < 12$  mm,
- ⇒  $s < 150$  mm,

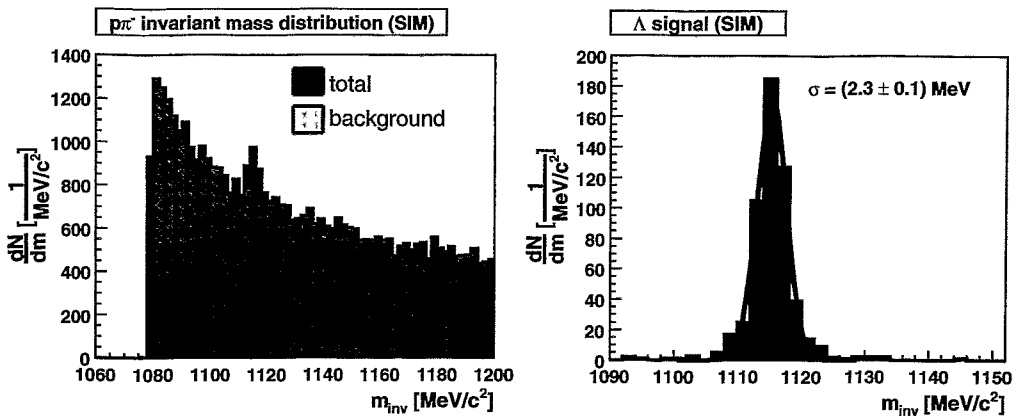


Figure 4.21: Simulated invariant mass distribution after application of cuts. The background from uncorrelated  $p\pi^-$  pairs is the cross-hatched area. On the right pad, the pure  $\Lambda$  signal is plotted and fitted with a Gaussian.

⇒ inner  $\chi_{seg}^2 > 0^*$  and  $< 50$

⇒ outer  $\chi_{seg}^2 > 0$  and  $< 50$ ,

⇒  $\chi_{RK}^2 > 0$  and  $< 50$ .

The simulated invariant mass distribution clearly reveals the  $\Lambda$  peak (see Fig. 4.21), which means that the cuts are now appropriate to be applied on the real data.

## 4.6 The $\Lambda$ Signal in Real Data

Following the steps of the previous analysis of simulated events, the  $p\pi^-$  invariant mass is calculated for experimental data. The statistics comprise about  $131 \cdot 10^6$  events (LVL1 and LVL2) and the graphical cuts for the  $p$ ,  $\pi^-$  identification remain like in simulation. The black distribution of Fig. 4.22 is the invariant mass distribution with the conditions on the inner and outer segment  $\chi_{seg}^2 > 0$  and  $\chi_{RK}^2 > 0$ , while the green curve includes the simulation enhancement cuts. In contrast to the simulation, the peak in the real data is present but not pronounced enough. This is expected, since the cutting power of the enhancement conditions in experiment differs from simulation. This means that the cuts for the  $\Lambda$  reconstruction need to be adapted in real data, in order to suppress the background more effectively.

The set of cuts that finally leads to the extraction of the signal are summarized in Tab. 4.8 and their effect on the experimental data is presented in Fig. 4.23. On the left panel the invariant mass distribution is not smooth any more but allows a

\*A  $\chi^2$  value cannot be negative by definition. In the Hydra analysis framework, we set  $\chi_{seg}^2 = -1$  as a flag to indicate that the corresponding MDC segment has not been successfully fitted.

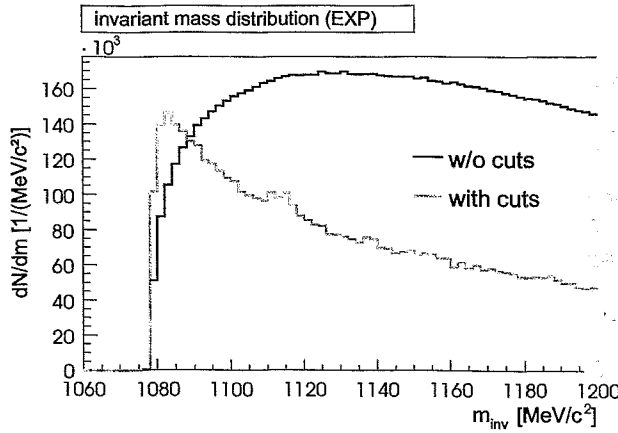


Figure 4.22: Experimental invariant mass distribution without (black) and with the enhancement cuts (green). The lower histogram has its corresponding axis on the right. The  $\Lambda$  peak is visible.

variable	simulation	experiment
$z_{sv} - z_{pv}$ [mm]	$> 30$	$> 40$
$d$ [mm]	$< 12$	$< 12$
$s$ [mm]	$< 150$	$< 150$
inner $\chi_{seg}^2$	$> 0$ and $< 50$	$> 0$ and $< 40$
outer $\chi_{seg}^2$	$> 0$ and $< 50$	$> 0$ and $< 40$
$\chi_{RK}^2$	$> 0$ and $< 50$	$> 0$ and $< 40$

Table 4.8: Summary of enhancement conditions applied in simulation and experimental data.

clear  $\Lambda$  peak to be seen. The background on the two sides of the peak is fitted with a third order polynomial function and then subtracted from the total distribution. The result appears on the right panel of Fig. 4.23. The signal is fitted with a Gaussian, in order to estimate the number of particles. The integral of the fit within a  $2\sigma_{\text{Gauss}}$  limit gives

$$N_{\Lambda} = (1117 \pm 124(\text{stat.}) \pm 27(\text{syst.})) \Lambda. \quad (4.3)$$

The statistical error is estimated by dividing the value of the signal with its significance ( $S \approx 9$ ), while the systematic error is the result of alternative fitting functions and fitting limits for the background description.

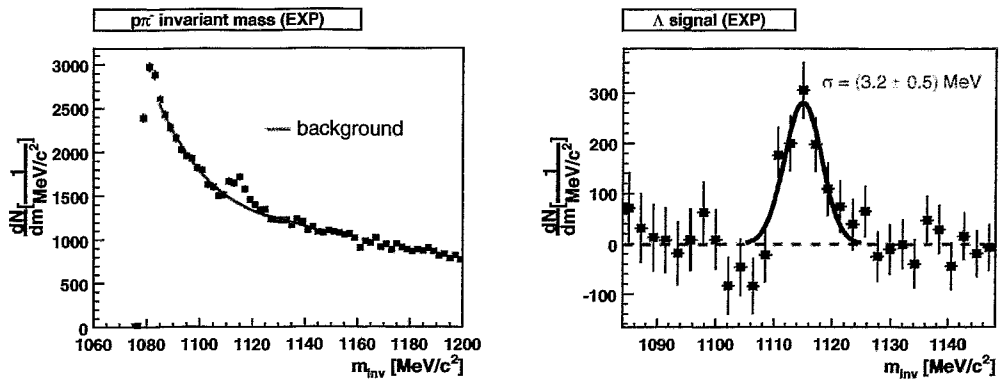


Figure 4.23: Extraction of the experimental signal. On the left the  $\Lambda$  signal is poking out of the background. The background is fitted with a third order polynomial function (green line). After its subtraction from the total distribution, the net  $\Lambda$  contribution is depicted on the right pad of the picture. The peak is fitted with a Gaussian function (blue), whose integral estimates the number of particles. The width of the peak is somewhat larger than the one in simulated data, as expected (see Fig. 4.21).

# 5 The $\Lambda$ Cross Section

## 5.1 Data Corrections

Aim of this analysis is the determination of the production cross section for  $\Lambda$  hyperons. The number of  $\Lambda$  extracted from the data is not sufficient (see page 72) to allow further studies of phase space distributions, such as transverse momentum or rapidity distributions. The total production cross section  $\sigma_\Lambda$  can be estimated from the equation

$$\sigma_\Lambda = \mathcal{M}_\Lambda \cdot \sigma_{geom(C+C)}, \quad (5.1)$$

where  $\mathcal{M}_\Lambda$  is the  $\Lambda$  multiplicity(yield) and  $\sigma_{geom(C+C)}$  the geometrical cross section of the reaction. The latter can be calculated as

$$\sigma_{geom(C+C)} = \pi r_0^2 (A_P^{1/3} + A_T^{1/3})^2 = \pi (1.2 fm)^2 (12^{1/3} + 12^{1/3})^2 = 948 \text{ mb}, \quad (5.2)$$

with  $A_P$  and  $A_T$  being the atomic number of the projectile and the target (for C+C  $A_P = A_T = 12$ ) and  $r_0$  the nucleon radius.  $\mathcal{M}_\Lambda$  can be deduced by knowing the total number of particles  $N_\Lambda^{tot}$  produced in a set of events  $N_{events}$  by

$$\mathcal{M}_\Lambda = \frac{N_\Lambda^{tot}}{N_{events}}. \quad (5.3)$$

What needs to be estimated then is  $N_\Lambda^{tot}$ . A series of corrections are necessary to compensate for all the factors that eventually altered this number at the different stages of the analysis. These correction factors are:

- ⇒ geometrical acceptance,
- ⇒ reconstruction efficiency of the tracking algorithm,
- ⇒ graphical cut identification efficiency,
- ⇒ geometrical cut efficiency for the signal enhancement,
- ⇒ branching ratio of the  $\Lambda$  decay,
- ⇒ lepton trigger efficiency,
- ⇒ centrality trigger (minimum bias).

## 5.2 Geometrical Acceptance and Total Reconstruction Efficiency

Because the number of  $\Lambda$  hyperons found in the data sample is small, the usual technique of correction with two-dimensional  $(p_t, y)$  matrices is not attempted here. Instead, the correction is one-dimensional, i. e. an average multiplication factor. One way for the determination of this factor is to extract it from simulation. To make the process less time consuming,  $10^6$   $\Lambda$  were created with the HADES event generator Pluto [Plu04]. The parameters selection for this simulation was based on recent FOPI results from Al+Al analysis at 1.93 AGeV [Kot06]. The inverse slope parameter  $T$  (temperature) of this experiment for  $\Lambda$  is  $T = (90 \pm 5)$  MeV. Since the C+C system is lighter, an educated guess for the  $\Lambda$  temperature in this system could be 80 MeV. There is no available systematic study for the dependence of temperature as a function of system size for lighter systems at medium energies nor is there a reliable scaling relation.

These  $10^6$   $\Lambda$  hyperons are embedded in  $10^6$  UrQMD events, from which the intrinsic  $\Lambda$  have been removed. The outcome is an enriched file with 1  $\Lambda$ /(UrQMD event) and a realistic track density environment as background description. These events are fully processed with HGeant and Hydra. Furthermore, the graphical cut and the enhancement conditions discussed in section 4.5 are applied. At the end, the number of reconstructed  $\Lambda$  divided by the input number of the  $10^6$  embedded ones gives the total reconstruction efficiency correction for the specified enhancement cuts, including also the geometrical acceptance and the branching ratio correction. A detailed overview of how the different analysis stages influence the number of reconstructed  $\Lambda$  is presented in Tab. 5.1. In the same table two more temperatures

analysis stage	$T = 60$ MeV	$T = 80$ MeV	$T = 100$ MeV
geometry	$(5.01 \pm 0.03)\%$	$(6.41 \pm 0.03)\%$	$(7.49 \pm 0.03)\%$
reconstruction	$(32.68 \pm 0.32)\%$	$(34.84 \pm 0.29)\%$	$(36.01 \pm 0.27)\%$
enhancement cuts	$(3.97 \pm 0.11)\%$	$(4.33 \pm 0.10)\%$	$(4.54 \pm 0.10)\%$
graphical cut	$(88.14 \pm 2.63)\%$	$(88.67 \pm 2.24)\%$	$(88.68 \pm 2.02)\%$
total efficiency ( $\mathcal{E}_{tot}$ )	$(0.1122 \pm 0.0033)\%$	$(0.1573 \pm 0.0040)\%$	$(0.1927 \pm 0.0044)\%$

Table 5.1: Geometrical acceptance and efficiencies at different stages of the analysis for three different temperatures  $T$ . The total efficiency includes all the previous steps (except the gray shaded line), plus the branching ratio of the  $\Lambda$  decay into  $p\pi^-$  (63.8%). Only sectors 0,2,3 are included.

$T = 60$  MeV and  $T = 100$  MeV are considered for deducing systematic errors on the acceptance, arising from the assumed  $T$  of the simulated fireball. A variation in temperature of the order of 20 MeV can lead to a 20% difference in geometrical acceptance with consequences for the total efficiency.

Starting with  $10^6$   $\Lambda$  hyperons, 63.9% of them decay into a  $p\pi^-$  pair (see Tab. 4.1).

From these pairs 6.41% cross all the detectors of the setup in HGeant, i. e. both  $p$  and  $\pi^-$  leave hits on all four MDC modules in the same sector, as well as on the META detectors. Of the pairs within the geometrical acceptance, 34.84% are reconstructed by the tracking software, meaning that the algorithm found hits from  $p$  and  $\pi^-$  tracks in all involved MDC and TOF detectors in the respective sector, it managed to fit the MDC hits into track segments ( $\chi_{seg}^2 > 0$ ) and the segments into track candidates, and a momentum value is attributed to them by the Runge-Kutta procedure ( $\chi_{RK}^2 > 0$ ). When the enhancement cuts are applied, this reconstruction efficiency drops to 4.33%. Finally, the graphical cut efficiency is estimated after applying the enhancement conditions. The analysis is run twice, once using the true particle ID from HGeant for the  $p\pi^-$  identification and a second time using the graphical cut ID. Dividing the number of  $\Lambda$  from the two methods, the graphical cut efficiency turns out to be around 88%.

The total reconstruction efficiency used for the correction of the data in the current analysis is

$$\mathcal{E}_{tot} = (0.1573 \pm 0.0040)\%, \quad (5.4)$$

a small value determined on one hand by the restricted geometrical acceptance of the  $p\pi^-$  pairs in three sectors and on the other hand by the limited reconstruction efficiency of secondary vertices away from the targets, imposed by the need of strict cuts.

An explanation can be offered in the cylindrical coordinate representation of the laboratory system. The distribution of the  $z$  coordinate of the  $p$  and  $\pi^-$  tracks (inner segment) is broader for those particles that originate from a  $\Lambda$  decay, compared to the primary ones (see Figs. 5.1, 5.2). In most of the  $\Lambda$  hyperon decays, the

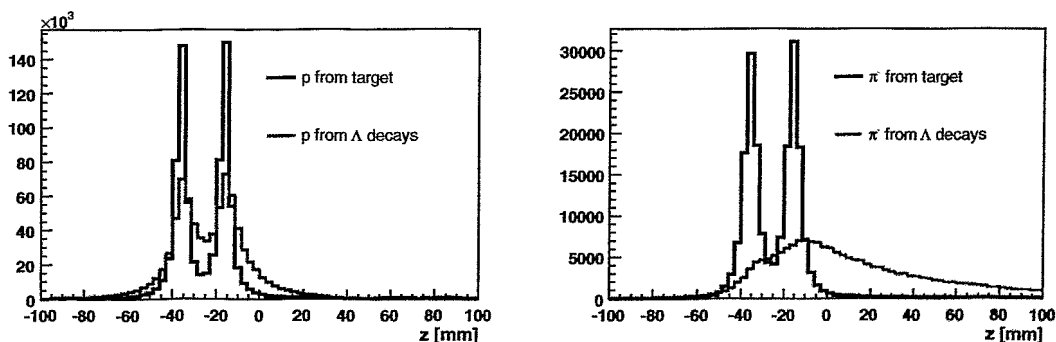


Figure 5.1: Distribution of the  $z$  coordinate for  $p$  and  $\pi^-$  tracks (units in counts [a.u.]). The ones coming from a  $\Lambda$  decay smear out the distribution in a way that is depicted in Fig. 5.2.

largest part of momentum is transferred to the proton, which keeps roughly the direction of its parent. The effect is a lot stronger in the  $\pi^-$  case, as the momentum transfer from the  $\Lambda$  is usually smaller. The  $\pi^-$  track loses memory of the initial direction of the  $\Lambda$  vector and as a consequence, the two targets are smeared out in the

$z$  distribution. The tracking algorithm used in this analysis is focused on the reconstruction of  $e^+e^-$  pairs that originate from vector meson decays inside the fireball and uses the target position information in the segment fits. This means that it has the ability to reconstruct tracks within a certain region around the two targets.

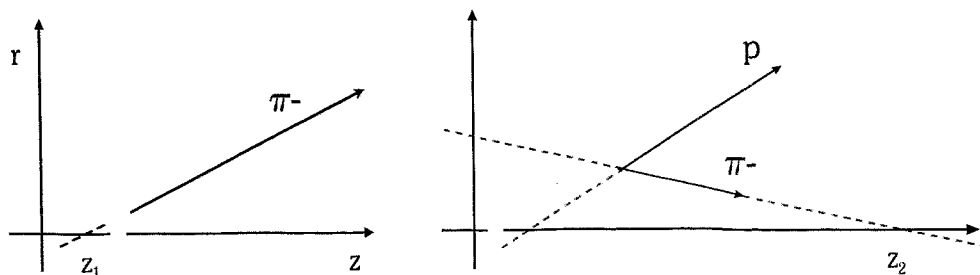


Figure 5.2: Reconstruction difference along the  $z$  axis for particles with and without  $\Lambda$  parent. One of the decay particles might lose memory of the initial direction of the  $\Lambda$  vector and in the cylindrical coordinates it looks as if it comes far from the target.

The tracking efficiency worsens close and further than the border of the region with consequences for the reconstruction ability of the two particles. The folding of these two distributions is reflected on the  $\Lambda$  efficiency.

### 5.3 Reconstruction Efficiency in Experiment

The enhancement cuts in simulation have been adjusted in such a way that they reject the same percentage of pairs as in the experimental data (see Tab. 5.2). The

variable	simulation	experiment
$z_{sv} - z_{pv}$ [mm]	> 27	> 40
distance $d$ [mm]	< 9.5	< 12
impact parameter $s$ [mm]	< 105	< 150
inner $\chi_{seg}^2$	> 0 and < 31	> 0 and < 40
outer $\chi_{seg}^2$	> 0 and < 30	> 0 and < 40
$\chi_{RK}^2$	> 0 and < 24	> 0 and < 40

Table 5.2: Adjusted simulation cuts for the experimental data correction.

correction of the experimental data is based on the assumption that the reconstruction efficiency is the same as in simulation. In order to study a possible discrepancy and quantify the effect,  $10^6$   $\Lambda$  particles are processed with HGeant and their decay products are embedded in experimental raw (list mode) data. A special analysis

is applied, in which only the Start and the MDC detectors are included in the reconstruction. The information from the META detector is absent, as well as the momentum calculation. In parallel, the same procedure of analysis is followed for simulation and at the end the two  $\Lambda$  reconstruction efficiencies are compared (see Tab. 5.3), after having applied the off-vertex cuts from Tab. 5.2. The starting value

# $\Lambda$ (off-vertex)	simulation	experiment
within acceptance	$28743 \pm 170$	$22349 \pm 150$
reconstructed	$11139 \pm 106$	$3415 \pm 58$
efficiency	$(38.8 \pm 0.4)\%$	$(15.3 \pm 0.3)\%$

Table 5.3: Comparison of tracking efficiencies between simulation and experiment.

for the  $\Lambda$  particles within the HADES acceptance differs for the two cases (28743 vs. 22349), as some events have been skipped during the merging of the simulated  $\Lambda$  decay products with the real tracks due to drift time inconsistencies. This is not a drawback, since the method provides an efficiency correction of the experimental data relatively to the simulation. At this analysis level, the reconstruction efficiency for decays far from target is 39% and 15% for simulation and experiment respectively. The relative efficiency  $\mathcal{E}_{rel}$  is the ratio of the two figures

$$\mathcal{E}_{rel} = (39.4 \pm 2.8)\% \quad (5.5)$$

meaning that in the experiment, it is possible to reconstruct in average 40% of the  $\Lambda$  particles with displaced decays, compared to the simulation.

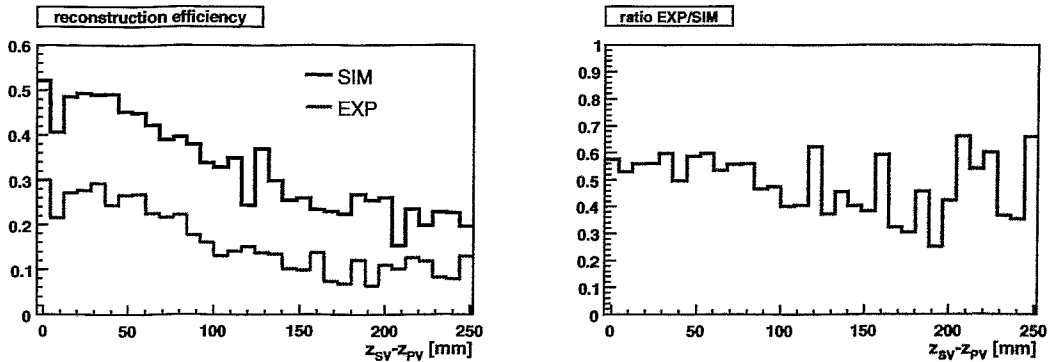


Figure 5.3: Comparison of reconstruction efficiencies between simulation and experiment.

It seems that the track density differs between simulated and real data, in particular in the vicinity of the targets. Background from secondary particles created at objects belonging to the setup and not being included in the simulation might result to the efficiencies of Fig. 5.3. However, further studies are required with the embedding of real tracks in the full HADES setup and a more extended analysis including the META detector.

## 5.4 Trigger Efficiency

The next step is to determine the effect of the trigger conditions on the data. Plotting the experimental invariant mass distribution for events with and without the LVL2 trigger flag, the numbers of  $\Lambda$  in the two cases differ by about 5%, taking into account that the LVL2 trigger concerns 44% of the events. Thus, the impact of the lepton trigger on the data is of minor importance.

The focus will be on correcting for the multiplicity condition (LVL1 trigger). The multiplicity trigger is closely related to the selection of small impact parameters which characterize central collisions, in contrast to the more peripheral ones that result to a lower particle multiplicity. For a small system like C+C, it is difficult to define what a central collision is, however, a multiplicity of equal or higher than 4 ( $\mathcal{M} \geq 4$ ) on the TOF walls has been applied to 85% of the events. The rest 15% has been registered with the condition  $\mathcal{M} \geq 2$ , which imposes almost no bias to the data.

The effect of the LVL1 trigger can be estimated with simulation using a multiplicity filter emulation. A fraction of the statistics ( $6 \cdot 10^5$  UrQMD events, filtered with HGeant) is analyzed with Hydra with the two different conditions,  $\mathcal{M} \geq 4$  and  $\mathcal{M} \geq 2$ , and the number of  $\Lambda$  hyperons is counted. The effect is presented in Tab. 5.4 together with the result of excluding the filter. Indeed, the effect of the  $\mathcal{M} \geq 2$  con-

	no condition	$\mathcal{M} \geq 4$	$\mathcal{M} \geq 2$
# $\Lambda$	2965	2620	2882
efficiency	–	$f4_{\Lambda}^{LVL1} = (88.4 \pm 1.7)\%$	$f2_{\Lambda}^{LVL1} = (97.2 \pm 1.8)\%$
# events	600000	332237	476884

Table 5.4: LVL1 trigger effect on the number of reconstructed  $\Lambda$ .

dition is negligible. The reduction of the  $\Lambda$  number for  $\mathcal{M} \geq 4$  is relatively small too, as  $\Lambda$  particles are mainly produced in central collisions. For the application of these correction factors to the data, their validity in  $4\pi$  has to be assumed.

The total number of  $\Lambda$  hyperons produced in  $131 \cdot 10^6$  real events would then be

$$N_{tot}^{\Lambda} = \frac{N_{\Lambda}}{\mathcal{E}_{tot} \cdot \mathcal{E}_{rel}} \left( \frac{0.85}{f4_{\Lambda}^{LVL1}} + \frac{0.15}{f2_{\Lambda}^{LVL1}} \right). \quad (5.6)$$

The quantities in this relation are known:

- ⇒  $N_{\Lambda} = 1117 \pm 124(\text{stat.}) \pm 27(\text{syst.}),$
- ⇒  $\mathcal{E}_{tot} = (0.1573 \pm 0.0040)\%,$
- ⇒  $\mathcal{E}_{rel} = (39.4 \pm 2.8)\%,$
- ⇒  $f4_{\Lambda}^{LVL1} = (88.4 \pm 1.7)\%,$

$$\Rightarrow f2_{\Lambda}^{LVL1} = (97.2 \pm 1.8)\%.$$

Inserting them in Eq. (5.6), the total number of  $\Lambda$  is

$$N_{tot}^{\Lambda} = 2011120 \pm 238016. \quad (5.7)$$

## 5.5 Minimum Bias Normalization

From Tab. 5.4 it is evident that the total number of events is reduced with the multiplicity condition by a factor  $f$ . What is known in the experiment though, is the number of LVL1 events  $N_{events}^{LVL1}$ , i. e. the events that passed the trigger. Since there is no available measurement of the incoming beam particles, the calculation of  $N_{events}$  requires information from another particle whose multiplicity is known for the specific system and energy, e. g.  $\pi^+$  [Mou06, Ave03]. Let the total number of events be equal to

$$N_{events} = N_{events}^{LVL1} \cdot f. \quad (5.8)$$

Like for  $\mathcal{M}_{\Lambda}$ , the multiplicity  $\mathcal{M}_{\pi^+}$  can be written as

$$\mathcal{M}_{\pi^+} = \frac{N_{\pi^+}}{N_{events}} = \frac{N_{\pi^+}^{LVL1}}{N_{events}^{LVL1} \cdot f} \left( \frac{0.85}{f4_{\pi^+}^{LVL1}} + \frac{0.15}{f2_{\pi^+}^{LVL1}} \right). \quad (5.9)$$

The LVL1 multiplicity  $\mathcal{M}_{\pi^+}^{LVL1} = N_{\pi^+}^{LVL1} / N_{events}^{LVL1}$ , as well as the minimum bias multiplicity  $\mathcal{M}_{\pi^+}$  are known:

$$\Rightarrow \mathcal{M}_{\pi^+}^{LVL1} = 1.15 \pm 0.12(\text{stat.}) \pm 0.12(\text{syst.}),$$

$$\Rightarrow \mathcal{M}_{\pi^+} = 0.79 \pm 0.09(\text{stat.}) \pm 0.08(\text{syst.}).$$

The factors  $f4_{\pi^+}^{LVL1}$  and  $f2_{\pi^+}^{LVL1}$  are deduced from simulation like for the  $\Lambda$  particles using the same number of events as before ( $6 \cdot 10^5$  events) and then counting the  $\pi^+$  (see Tab. 5.5).

	no condition	$\mathcal{M} \geq 4$	$\mathcal{M} \geq 2$
# $\pi^+$	806987	696226	773265
efficiency	—	$f4_{\pi^+}^{LVL1} = (86.3 \pm 0.1)\%$	$f2_{\pi^+}^{LVL1} = (95.8 \pm 0.1)\%$

Table 5.5: LVL1 trigger effect on  $\pi^+$  as deduced from simulation.

From Eq. (5.9), the factor  $f$  is estimated to be

$$f = 1.66 \pm 0.22(\text{stat.}) \pm 0.21(\text{syst.}). \quad (5.10)$$

Now all the quantities needed for the calculation of the  $\Lambda$  cross section are in hand. It should be noted here that the  $\Lambda$  coming from  $\Sigma^0$  decays ( $\Sigma^0 \rightarrow \Lambda\gamma$ , branching ratio

100%) are experimentally indistinguishable from the primary ones. From Eqs. (5.1), (5.3) and (5.8), we calculate the minimum bias  $\Lambda + \Sigma^0$  multiplicity to be

$$\mathcal{M}_{\Lambda+\Sigma^0} = 0.0092 \pm 0.0012(\text{stat.})_{-0.0017}^{+0.0034}(\text{syst.}) \quad (5.11)$$

and the production cross section

$$\sigma_{\Lambda+\Sigma^0} = ( 8.7 \pm 1.1(\text{stat.})_{-1.6}^{+3.2}(\text{syst.}) ) \text{ mb} . \quad (5.12)$$

The systematic errors come from the different inverse slope parameter assumptions (see section 5.2). The latter influence the total reconstruction efficiency. The correction of  $\mathcal{E}_{rel}$  is not affected, as the systematic errors are canceled out both in the simulation efficiency and the experimental one.

## 5.6 Discussion

### 5.6.1 Particle Ratios and Relative Strangeness Content

Particle ratios are thought to deliver information about the degree of chemical equilibration in heavy-ion collisions. In Tab. 5.6 a comparison between the measured strange particle multiplicities and the predicted ones by UrQMD is given. Charged  $\Sigma$  hyperons cannot be measured with the HADES setup, as their decay products contain neutral particles. Thus, for estimating their multiplicity  $\mathcal{M}_{\Sigma^\pm}$  the strangeness balance can be employed:

$$\begin{aligned} N_{\bar{s}} &= N_s \Rightarrow \\ \mathcal{M}_{K^+} + \mathcal{M}_{K^0} &= \mathcal{M}_{\Lambda+\Sigma^0} + \mathcal{M}_{\Sigma^\pm} + \mathcal{M}_{K^-} + \mathcal{M}_{\bar{K}^0} \Rightarrow \\ \mathcal{M}_{\Sigma^\pm} &= \mathcal{M}_{K^+} + \mathcal{M}_{K^0} - \mathcal{M}_{\Lambda+\Sigma^0} - \mathcal{M}_{K^-} - \mathcal{M}_{\bar{K}^0}, \end{aligned} \quad (5.13)$$

where  $N_{\bar{s}}$  and  $N_s$  are the numbers of produced particles containing an  $\bar{s}$  and an  $s$  quark respectively. The multiplicity for  $K^+$  for the same system and energy is  $\mathcal{M}_{K^+} = 0.0053 \pm 0.0005$  [Lau99]\*. Due to the isospin symmetric system one can assume that

$$\mathcal{M}_{K^+} = \mathcal{M}_{K^0}, \quad \mathcal{M}_{K^-} = \mathcal{M}_{\bar{K}^0}. \quad (5.14)$$

The  $K^-$  and  $\bar{K}^0$  have a very small contribution to the strangeness balance ( $\sigma_{K^-} = (0.19 \pm 0.06)$  mb [Lau99]), as they are produced below threshold at these collision energies. The same is valid for multi-strange baryons like  $\Xi$  and  $\Omega$ , which are very rare at these energies and their yields can be neglected. Finally we estimate  $\mathcal{M}_{\Sigma^\pm} = 0.0010 \pm 0.0014(\text{stat.})_{-0.0017}^{+0.0034}(\text{syst.})$ . The error is dominated by the large  $\mathcal{M}_{\Lambda+\Sigma^0}$  uncertainty.

\*HADES has measured the  $K^+$  production cross section as well [Sad06] and the result  $\sigma_{K^+} = (5.9 \pm 1.1(\text{stat.})_{-1.1}^{+1.2}(\text{syst.}))$  mb is in very good agreement with the KaoS measurement.

ratio	UrQMD (v1.3)	measurement
$\mathcal{M}_{K^+}/\mathcal{M}_{\Lambda+\Sigma^0}$	0.72	$0.58 \pm 0.09(\text{stat.})_{-0.71}^{+0.42}(\text{syst.})$
$\mathcal{M}_{\Lambda+\Sigma^0}/\mathcal{M}_{\langle\pi\rangle}$	0.0059	$0.0114 \pm 0.0016(\text{stat.})_{-0.0088}^{+0.0164}(\text{syst.})$
$\mathcal{M}_{\Sigma^\pm}/\mathcal{M}_{\Lambda+\Sigma^0}$	0.40	$0.13 \pm 0.16(\text{stat.})_{-0.06}^{+0.59}(\text{syst.})^*$

Table 5.6: Comparison of particle ratios between UrQMD and experiment for C+C at 2 AGeV and minimum bias collisions.  $\mathcal{M}_{\langle\pi\rangle}$  is the average pion multiplicity and equals  $0.81 \pm 0.04(\text{stat.}) \pm 0.04(\text{syst.})$ . The statistical errors from UrQMD are below 1% and therefore not displayed. The yield marked with the asterisk is not the result of a direct measurement but an estimate of the  $\Sigma^\pm$  multiplicity employing the strangeness balance.

From Tab. 5.6 it becomes clear that the UrQMD predictions differ from the measured values, with most pronounced the discrepancy in the strange baryon ratio  $\mathcal{M}_{\Sigma^\pm}/\mathcal{M}_{\Lambda+\Sigma^0}$ . A similar observation comes from the Ni+Ni FOPI results at 1.93 AGeV [Mer04, Her04], where the strangeness balance seems to be satisfied with the need of only a relatively small number of  $\Sigma^\pm$  hyperons. This could point either to a reduced  $\Sigma^\pm$  yield (compared to the theoretical model predictions) or the possibility that these charged particles are absorbed in the medium and converted into neutral ones.

Having all yields of strange particles available, it is possible to estimate the Wróblewski factor  $\lambda_s$  for C+C at 2 AGeV. This factor is defined as [Cle02]

$$\lambda_s \equiv \frac{2\langle s\bar{s} \rangle}{\langle u\bar{u} \rangle + \langle d\bar{d} \rangle}, \quad (5.15)$$

where the quantities in angular brackets refer to the number of newly created primary valence quark-antiquark pairs, i. e. all quarks that were present in the target and projectile are excluded. The Wróblewski factor is determined at the moment of chemical freeze-out from hadrons and especially hadron resonances before they decay. This ratio is not an easily measurable observable, unless all resonances are reconstructed from the final-state particles. This is possible, since HADES provides a complete picture of the hadronic production [Mou06, Tlu06]. The components of Eq. (5.15) can be analytically written as follows [Wro85]:

$$\begin{aligned} \langle s\bar{s} \rangle &= \mathcal{M}_{K^+} + \mathcal{M}_{K^0} = \mathcal{M}_{\Lambda+\Sigma^0} + \mathcal{M}_{\Sigma^\pm} + \mathcal{M}_{K^-} + \mathcal{M}_{\bar{K}^0}, \\ \langle u\bar{u} \rangle + \langle d\bar{d} \rangle &= \mathcal{M}_{\pi^+} + \mathcal{M}_{\pi^-} + \mathcal{M}_{\pi^0}. \end{aligned} \quad (5.16)$$

In the strangeness term there are also  $\eta$  and  $\phi$  mesons contributing but their yields at 2 AGeV are minor, as can be seen in Fig. 5.5, and therefore they can be neglected in the  $\lambda_s$  estimate. For the same reason the denominator of Eq. (5.15) contains only the pion contribution, as the production of baryon-antibaryon pairs has a higher energy

threshold. The multiplicities of Eq. (5.16) are known:

$$\begin{aligned}
 \mathcal{M}_{K^+} &= \mathcal{M}_{K^0} = 0.0053 \pm 0.0005, \\
 \mathcal{M}_{K^-} &= \mathcal{M}_{\bar{K}^0} = 0.00020 \pm 0.00006, \\
 \mathcal{M}_{\Lambda+\Sigma^0} &= 0.0092 \pm 0.0012(\text{stat.})_{-0.0017}^{+0.0034}(\text{syst.}), \\
 \mathcal{M}_{\Sigma^\pm} &= 0.0010 \pm 0.0015(\text{stat.})_{-0.0017}^{+0.0034}(\text{syst.}), \\
 \mathcal{M}_{\pi^+} &= 0.79 \pm 0.08(\text{stat.}) \pm 0.08(\text{syst.}), \\
 \mathcal{M}_{\pi^-} &= 0.82 \pm 0.08(\text{stat.}) \pm 0.08(\text{syst.}), \\
 \mathcal{M}_{\pi^0} &= \frac{1}{2}(\mathcal{M}_{\pi^+} + \mathcal{M}_{\pi^-}) = 0.81 \pm 0.06(\text{stat.}) \pm 0.06(\text{syst.}).
 \end{aligned}
 \tag{5.17}$$

Inserting the above values in Eqs. (5.16) and (5.15), we estimate the Wróblewski factor for C+C at 2 AGeV to be equal to

$$\lambda_s = 0.0087 \pm 0.0016(\text{stat.})_{-0.0027}^{+0.0074}(\text{syst.}). \tag{5.18}$$

Other existing  $\lambda_s$  values measured by several experiments [Bec01] are compiled in Fig. 5.4 as a function of the available centre-of-mass energy  $\sqrt{s}$  and are displayed together with the HADES result. The attempt to parameterize this dependence with

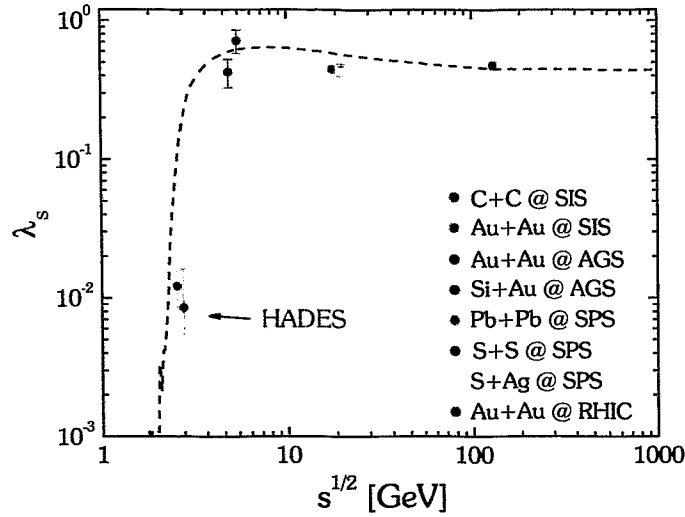


Figure 5.4: The Wróblewski factor  $\lambda_s$  as a function of  $\sqrt{s}$ . The symbols represent a compilation of the available measured data taken from [Bec01]. The HADES point is from Eq. (5.18). The dashed line has been calculated using the freeze-out values of the temperature and the baryon chemical potential with a thermo-statistical model [Cle02].

a statistical model [Cle02] is represented by the dashed line, exhibiting a maximum

around 7-8 GeV. The interpretation of this maximum is a topic of debate, see for example [Cle02, Gaz04].

The total  $\lambda_s$  distribution is the sum of the partial contributions of strange mesons, strange baryons and the hidden strangeness from  $\eta$  and  $\phi$  (see Fig. 5.5). Nevertheless,

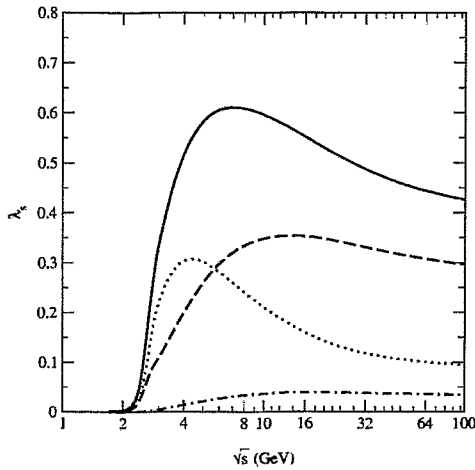


Figure 5.5: Contributions to the Wróblewski factor (solid line) coming from strange baryons (dotted line), strange mesons (dashed line) and hidden strangeness (dash-dotted line). The figure is taken from [Cle02].

it is important to disentangle the partial contributions of  $\lambda_s$ , in order to find out whether the source of the maximum in the distribution is attributed to the strange mesons or the strange baryons, or it is related to the non-strange particles yield behaviour as a function of  $\sqrt{s}$ . In Fig. 5.6, such a individual contribution for the strange baryons is depicted.

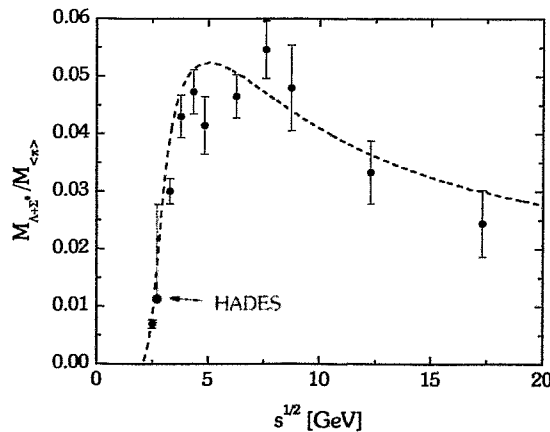


Figure 5.6: The  $(\Lambda + \Sigma^0) / \langle \pi \rangle$  ratio as a function of  $\sqrt{s}$ . The data points are from HADES (see Tab. 5.6) and [Gaz04, Afa02, Ant04, Ahl98, Alb02, Kla03]. The dashed line is a prediction of a statistical model [Whe].

The shape of the  $(\Lambda + \Sigma^0)/\langle\pi\rangle$  ratio indeed exhibits a maximum and resembles the prediction of the statistical model. Moreover, it has been shown that similar ratios with multi-strange particles, like  $\Xi^-/\pi^+$  and  $\Omega^-/\pi^+$ , exhibit their maxima at higher  $\sqrt{s}$  [Cle05]. The existence of the maximum designates the transition from baryon-rich to meson-rich produced matter. How rapid this transition can be is a matter of theoretical debate at the moment. Assisting towards the direction of resolving this, the future facilities at GSI will allow a finer step in beam energies at the region of maximum baryon density.

## 5.6.2 Centrality Dependence

In Fig. 5.7 several measurements of the  $\Lambda + \Sigma^0$  multiplicity at 2 AGeV from various reactions and centrality selections are depicted together with measurements for  $K^+$ . As these particles are produced together, they are expected to demonstrate similar yield behaviour – at least for light collision systems where the  $\Lambda$  absorption via strangeness exchange processes like  $\pi Y \rightarrow K^- N^+$  should not play an important role. The measured multiplicities  $\mathcal{M}$  have been normalized to the mean number of participating nucleons  $\langle A_{\text{part}} \rangle$ . For central collisions the latter has been estimated by calculating the geometrical overlap of the colliding nuclei for an upper limit of the impact parameter  $b_{\text{max}}$ . For minimum bias measurements,  $\langle A_{\text{part}} \rangle$  equals  $(A_T + A_P)/4$ .

The  $\mathcal{M}_{\Lambda + \Sigma^0}$  measurements from left to right are taken from: the current thesis (see Eq. (5.11)), [Jus98], [Her04] and [Chu99], while the  $\mathcal{M}_{K^+}$  ones are from [Lau99], [Men00] and [Ahl00]. In [Ahl00], as only the midrapidity  $dN/dy$  value is provided, in order to extract the total  $K^+$  yield, a rapidity distribution with  $dN/dy = 0.381 \pm 0.015$  and  $\sigma_{\text{gauss}} = 0.43 \pm 0.05$  (FWHM  $\approx 1$  [Men00]) was integrated.

Overlaid in the same figure, the dashed lines correspond to BUU calculations [Bar06, Bar03] (see Appendix A.2) for the same particles, performed for C+C, Cu+Cu, Xe+Xe and Au+Au collisions for various centrality selections. This BUU model uses a momentum and density dependent mean field in which the baryons are propagated. Strange baryons feel only 2/3 of the baryon field and their production processes are treated perturbatively. The  $\Sigma^0$  contribution to the  $\Lambda$  content is 1/3, in contrast with 1/4 in UrQMD. Indeed the behaviour of the two lines is comparable and the neutral hyperon yield is higher than the  $K^+$  yield, as required by the strangeness balance in an isospin symmetric system\*.

However, this alleged yield tendency is not reflected in the measured data. The  $\Lambda$  measurements differ from  $K^+$  in the sense that they seem to exhibit a rather flat distribution or a slightly increasing tendency as a function of  $\langle A_{\text{part}} \rangle$ , if the large errors of the two first points are taken into account. A possible absorption effect of the hyperons would be reflected to an enhanced  $K^-$  yield, however such a scenario is not supported by the experimental results [För03, Men00]. It is obvious that in

<sup>†</sup>Y stands for hyperon.

\*The production threshold for  $\Sigma$  is higher than the  $\Lambda$  one, since  $\Sigma$  is heavier.

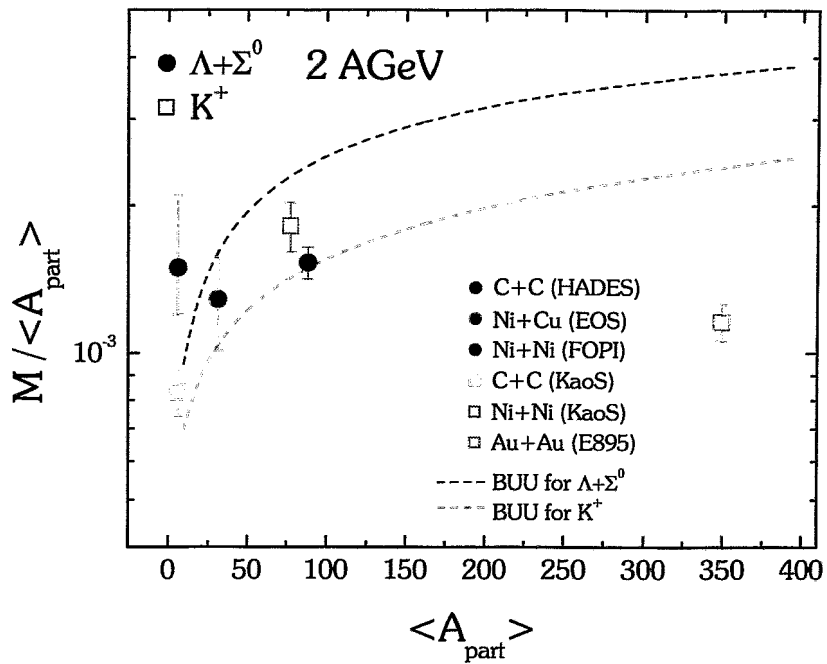


Figure 5.7: Measured multiplicities  $M$  normalized to the mean number of participants  $\langle A_{part} \rangle$  as a function of  $\langle A_{part} \rangle$  for  $\Lambda + \Sigma^0$  (full symbols) and  $K^+$  (empty symbols) at kinetic beam energy 2 AGeV. The dashed lines are BUU calculations from H.-W. Barz. The data points are cited in the text.

order to resolve the puzzle and complete the picture of strangeness production, the charged  $\Sigma^\pm$  yields need to be measured.

### 5.6.3 Beam Energy Dependence

Plotting the  $\Lambda + \Sigma^0$  yield normalized to  $\langle A_{\text{part}} \rangle$  as a function of kinetic beam energy, we get an impression of the  $\Lambda + \Sigma^0$  excitation function. Such a data compilation for elementary p+p and heavy-ion reactions appears in Fig. 5.8. The proton data come from [Gaz96] and the references therein. The A+A data are taken from [Ani84, Her04, Jus98, Pin02, Ant04] and the current thesis. The yields per par-

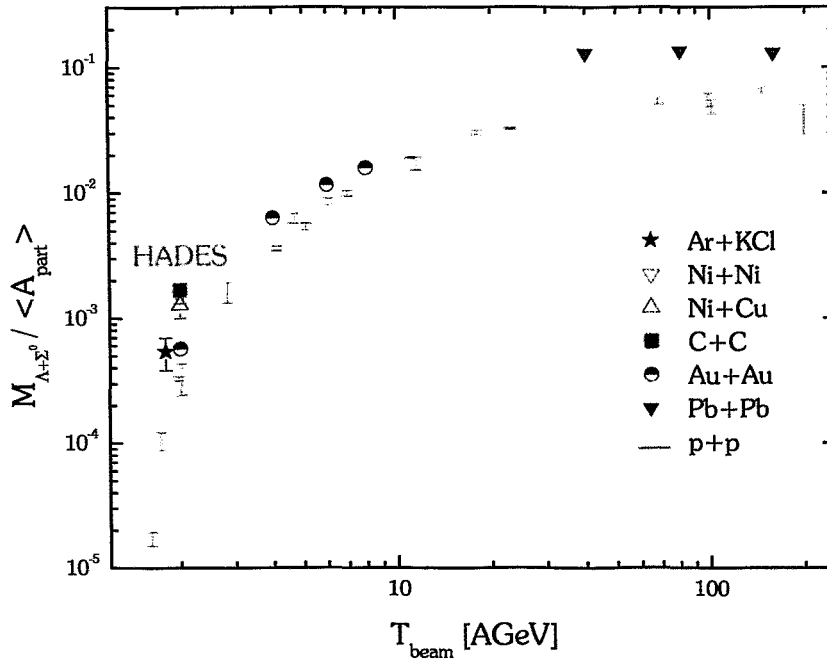


Figure 5.8:  $\Lambda + \Sigma^0$  multiplicity per mean number of participant  $\langle A_{\text{part}} \rangle$  for p+p and A+A collisions as a function of kinetic beam energy. For compiling the Pb+Pb data [Ant04] from the NA49 collaboration the  $\Lambda$  multiplicity has been divided with the mean number of wounded nucleons  $\langle N_w \rangle$  as described in the publication. Note that not all existing measurements are included in the figure, especially at high energies.

ticipating nucleon are larger in A+A collisions than in p+p collisions for all beam energies. Similar behaviour is observed for the excitation function of  $K^+$  [Sen99]. The difference between A+A and p+p data can be attributed to the increase of effective beam energy in A+A collisions, i. e. the available energy in a nucleon pair is higher than in the free p+p reaction. What also becomes evident is the lack of measurements between 10 and 40 AGeV. This is the beam energy gap that the future GSI project FAIR is going to cover.

## 6 Summary

The results of the current thesis concern two fronts. Hardwarewise, the conditions under which the third plane of HADES drift chambers operate are studied. Malfunction symptoms, like high voltage trips in one of them led to investigations concerning the operational stability that relates to the wire tension inside the modules. The wire deflections were simulated under various orientations and gravity vectors with the outcome of this study leading to the conclusion that such symptoms could not have been caused by tension loss. During the examination of the interior of the module white filaments were discovered being spun across large areas of an anode layer. X-ray and infrared spectroscopy methods implied that cellulose containing tissue material might have been the origin of these structures. It is unlikely, though, that the creation of such filaments is related to aging effects. This claim is supported not only by the aging tests performed on the modules but also by the absence of similar symptoms in other chambers.

On the other hand, the HADES experiment has had a series of physics runs with a variety of beam projectiles and energies over the last years. The data collected for the study of the C+C system at the beam kinetic energy of 2 AGeV were analyzed and the signal of the  $\Lambda$  hyperons was successfully reconstructed for the first time at this system and energy. The possibility to use the existing analysis software, originally developed for the reconstruction of the  $e^+e^-$  decays of vector mesons, was investigated and its use for the specific purpose of studying the  $\Lambda$  production turns out to be sufficient. However, the restricted geometrical acceptance in which high resolution tracking took place at the specific run, together with the small reconstruction efficiency of the algorithm for the  $\Lambda$  probe, imposed by the strict geometrical conditions applied for the signal reconstruction, make this investigation fairly CPU time-consuming.

Due to the low reconstructed statistics, it is not yet possible to extract information on phase space distributions. Instead, the total production cross section is estimated by multiplying the  $\Lambda$  yield with the geometrical cross section of the reaction and is found to be

$$\sigma_{\Lambda+\Sigma^0} = ( 8.7 \pm 1.1(\text{stat.})_{-1.6}^{+3.2}(\text{syst.}) ) \text{ mb} .$$

Strange particle ratios are compared with the predicted ones from UrQMD. The yields of strange baryons are not properly described by the model, an observation that is in agreement with findings from other experiments. Particularly puzzling is the fact that a  $\Sigma^\pm$  yield, a lot smaller than what the theoretical models predict, is

sufficient to satisfy the strangeness balance. Moreover, the  $\Lambda$  production yield as a function of the mean number of participating nucleons  $\langle A_{\text{part}} \rangle$  hints to hyperon absorption with increasing  $\langle A_{\text{part}} \rangle$  but the question remains why this absorption is not accompanied by a corresponding increase of the  $K^-$  yield. Thus, further investigations are necessary, both in the theoretical and the experimental front. An opportunity to do so are the upcoming experiments planned for HADES. The detector setup is now complete and the replacement of the TOFINO walls with RPC detectors will allow runs with heavier nuclei and better resolution in the low polar angles.

# Appendix A      Models for the Description of Heavy-ion Collisions

The theoretical models used nowadays to study intermediate-energy and relativistic heavy-ion collisions can be roughly divided into two groups: macroscopic models based on nuclear fluid dynamics and microscopic models based on kinetic transport theory. Macroscopic models describe the nuclear interactions by using hydrodynamic equations and assume local equilibrium. These models are mainly applicable for central collisions of heavy nuclei where the system has many degrees of freedom and the mean free path of the nucleons is short compared to the spatial dimension and gradients of the system. The great advantage of these models is that basic nuclear matter features, e. g. EOS supplemented by dissipative effects (viscosity, thermoconductivity), are used directly as input. However, relativistic heavy-ion collisions involve many quantum and non-equilibrium effects, particle production, fragment formation etc., and a more detailed description of these phenomena in can be obtained by microscopic dynamics.

A microscopic dynamics description of heavy-ion collisions is usually based on transport theory. Here the propagation of individual particles is simulated. The main ingredients in this description are the cross sections, the two-body potentials and the decay widths. Since the particles propagate in hot and dense matter, their properties might change significantly. Consequently, properties like effective masses, effective momenta, in-medium cross sections and decay widths should be calculated for the actual local situation in which the particle propagates. Furthermore, heavy-ion collisions demonstrate different features at different energies. At low energies, because of Pauli blocking of two body-collisions, a suitable approach is the mean-field theory, such as the time-dependent Hartree-Fock theory. At higher energies, the reaction dynamics at the initial stage is mainly governed by two-body collisions and particle production becomes increasingly important. For this purpose, various models have been developed which address specific features of selected energies. Some of these models of relevance for SIS energies are described below.

## A.1 BUU-type models

At energies in the 1 AGeV range and for the expansion stage of relativistic heavy-ion collisions, the effects of mean-field, two-body collisions and the Pauli principle are important and needed to be included. This leads to the use of the so-called Vlasov-Uehling-Uhlenbeck (VUU) or Boltzmann-Uehling-Uhlenbeck (BUU) equation

$$\left( \frac{\partial}{\partial t} + (\nabla_{\vec{p}} H) \nabla_{\vec{r}} - (\nabla_{\vec{r}} H) \nabla_{\vec{p}} \right) f_i(\vec{r}, \vec{p}, t) = I_{col}[f_1, \dots, f_i, \dots, f_M], \quad (\text{A.1})$$

which governs the time evolution of the one-body distribution function  $f_i(\vec{r}, \vec{p}, t)$  in phase space.  $I_{col}$  is the collision integral which accounts for changes in  $f_i$  due to two-particle collisions. At incident energies of 1-2 AGeV the colliding system contains not only nucleons but also  $\pi$ ,  $\eta$ , K and  $\Delta$  particles, as well as higher baryon resonances (N(1440), N(1520), N(1535)). Also strange baryons like  $\Lambda(1116)$ ,  $\Lambda(1405)$  and  $\Sigma$  are of importance for studying strangeness degrees of freedom. Therefore, distribution functions  $f$  and evolution equations need to be introduced for each type of particles and their coupling as well.

The BUU equation is usually solved by the test-particle method. Here the continuous one-body distribution function  $f$  at  $t = 0$  is represented by an ensemble of  $m \cdot (A_p + A_t)$  point-like particles, where  $A_p$  and  $A_t$  denote the number of nucleons contained in the projectile and the target, respectively. The left part of the BUU equation can be regarded as the transport equation for a distribution of classical particles whose propagation in the mean-field is given by Hamilton's equations of motion:

$$\dot{\vec{p}}_i = -\frac{\partial \langle H \rangle}{\partial \vec{r}_i}, \quad \dot{\vec{r}}_i = \frac{\partial \langle H \rangle}{\partial \vec{p}_i}, \quad (\text{A.2})$$

where  $\langle H \rangle = \sum_i \frac{p_i^2}{2m_i} + \frac{1}{2} \sum_{i \neq j} V_{ij}$ .

The two-body collisions (the right part of the equation or the Uehling-Uhlenbeck part) are treated by Monte-Carlo procedures. BUU type models succeeded in the description of several one-body observables and collective flow and particle production. However, phenomena like fragment formation and two-particle correlations in relativistic heavy-ion collisions cannot be calculated in the framework of BUU type models, since they are intimately connected to many-body correlations of particles and fluctuations.

## A.2 QMD models

To solve these problems one considers N-particle correlations and N-particle distributions explicitly. This can be done within an approach, which is called Quantum Molecular Dynamics (QMD) [Bas98]. In the QMD model each particle  $i$  is repre-

sented by a Gaussian wave packet in both space and momentum. From these packets the total N-particle distribution function results by superposition

$$f(\vec{r}, \vec{p}, t) = \sum_i^N f_i(\vec{r}_i, \vec{p}_i, t). \quad (\text{A.3})$$

The centre of momentum of each Gaussian  $f_i(\vec{r}_i, \vec{p}_i, t)$  is propagated under the influence of a potential according to the classical Hamiltonian equations of motion. Hard nucleon-nucleon collisions are included in QMD models by employing a collision term. Two particles collide if their minimum distance  $d$  in their centre of mass frame fulfils the requirement

$$d \leq d_0 = \sqrt{\frac{\sigma_{tot}}{\pi}}, \quad (\text{A.4})$$

where the cross section is assumed to be the free cross section of the regarded collision type (N-N, N- $\Delta$ , N- $\pi$ ,...). In addition, the Pauli blocking of particles is taken into account by checking the phase space densities in the final states of a two-body collision. Meson creation and absorption can be treated via resonance processes or inelastic  $2 \leftrightarrow 3$  collisions; rescattering can happen at every hadron species.

Isospin can be treated explicitly leading to the so-called **Isospin Quantum Molecular Dynamics (IQMD)** model. Also, relativistic effects are expected to become important in heavy-ion collisions at high energies. In the usual microscopic transport models like BUU and QMD, the kinematics is already relativistic but the interactions are usually treated non-relativistically, which breaks the Lorentz covariance. The frame dependence of the transport model has been addressed in the **Relativistic Quantum Molecular Dynamics (RQMD)** and **Ultra relativistic Quantum Molecular Dynamics (UrQMD)** models by the use of Hamiltonian dynamics constrained by Poincaré invariance. The meson-exchange nature of nucleon-nucleon interactions, by which the nucleon mean-field potential can be separated into different Lorentz components (e.g. scalar and vector potentials) has been included in the **Relativistic BUU** approach (RBUU) and **Hadron String Dynamics (HSD)** approach.

## Appendix B Calculation of Distance between two Trajectories

We first consider two trajectories represented by straight infinite lines  $\mathcal{L}1$ ,  $\mathcal{L}2$  (see Fig. B.1):

$$\begin{aligned}\mathcal{L}1 : \vec{P}(s) &= \vec{P}_0 + s(\vec{P}_1 - \vec{P}_0) = \vec{P}_0 + s\vec{u}, \\ \mathcal{L}2 : \vec{Q}(t) &= \vec{Q}_0 + t(\vec{Q}_1 - \vec{Q}_0) = \vec{Q}_0 + t\vec{v}.\end{aligned}\tag{B.1}$$

Let  $\vec{w}(s, t) = \vec{P}(s) - \vec{Q}(t)$  be a vector between points on the two lines. We want to find the  $\vec{w}(s, t)$  that has a minimum length for all  $s$  and  $t$ . In any n-dimensional

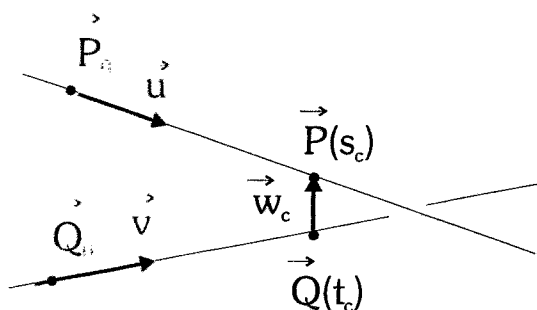


Figure B.1: Distance vector  $\vec{w}_c$  between two lines.

space, the two lines  $\mathcal{L}1$  and  $\mathcal{L}2$  are closest at unique points  $\vec{P}(s_c)$  and  $\vec{Q}(t_c)$  for which  $\vec{w}(s_c, t_c)$  attains its minimum length. Also, if  $\mathcal{L}1$  and  $\mathcal{L}2$  are not parallel, then the line segment  $\vec{P}(s_c)\vec{Q}(t_c)$  joining the closest points is uniquely perpendicular to both lines at the same time. No other segment between  $\mathcal{L}1$  and  $\mathcal{L}2$  has this property. That is, the vector  $\vec{w}_c = \vec{w}(s_c, t_c)$  is uniquely perpendicular to the line direction vectors  $\vec{u}$  and  $\vec{v}$ , and this is equivalent to it satisfying the two equations:

$$\begin{aligned}\vec{u} \cdot \vec{w}_c &= 0, \\ \vec{v} \cdot \vec{w}_c &= 0.\end{aligned}\tag{B.2}$$

We can solve these two equations by substituting

$$\vec{w}_c = \vec{P}(s_c) - \vec{Q}(t_c) = \vec{w}_0 + s_c \vec{u} - t_c \vec{v}, \quad (\text{B.3})$$

where  $\vec{w}_0 = \vec{P}_0 - \vec{Q}_0$ , into each one to get two simultaneous linear equations:

$$\begin{aligned} (\vec{u} \cdot \vec{u})s_c - (\vec{u} \cdot \vec{v})t_c &= -\vec{u} \cdot \vec{w}_0, \\ (\vec{v} \cdot \vec{u})s_c - (\vec{v} \cdot \vec{v})t_c &= -\vec{v} \cdot \vec{w}_0. \end{aligned} \quad (\text{B.4})$$

Then, letting

$$\begin{aligned} a &= \vec{u} \cdot \vec{u}, \quad b = \vec{u} \cdot \vec{v}, \\ c &= \vec{v} \cdot \vec{v}, \quad d = \vec{u} \cdot \vec{w}_0 \quad \text{and} \quad e = \vec{v} \cdot \vec{w}_0, \end{aligned} \quad (\text{B.5})$$

we solve for  $s_c$  and  $t_c$  as:

$$s_c = \frac{be - cd}{ac - b^2} \quad \text{and} \quad t_c = \frac{ae - bd}{ac - b^2} \quad (\text{B.6})$$

whenever the denominator  $ac - b^2$  is nonzero. Note that

$$ac - b^2 = |\vec{u}|^2 |\vec{v}|^2 - (|\vec{u}| |\vec{v}| \cos q)^2 = (|\vec{u}| |\vec{v}| \sin q)^2 \geq 0 \quad (\text{B.7})$$

is always nonnegative. When  $ac - b^2 = 0$ , the two equations are dependant, the two lines are parallel and the distance between the lines is constant. We can solve for this parallel distance of separation by fixing the value of one parameter and using either equation to solve for the other. Selecting  $s_c = 0$ , we get  $t_c = d/b = e/c$ .

Having solved for  $s_c$  and  $t_c$ , we have the points  $\vec{P}(s_c)$  and  $\vec{Q}(t_c)$  where the two lines  $\mathcal{L}1$  and  $\mathcal{L}2$  are closest. Then the distance between them is given by:

$$d(\mathcal{L}1, \mathcal{L}2) = |\vec{P}(s_c) - \vec{Q}(t_c)| = \left| (\vec{P}_0 - \vec{Q}_0) + \frac{(be - cd)\vec{u} - (ae - bd)\vec{v}}{ac - b^2} \right|. \quad (\text{B.8})$$

In the  $\Lambda$  analysis, the two lines are the  $p$  and  $\pi^-$  tracks. Combinations of parallel lines are rejected. The secondary vertex  $\vec{s}\vec{v}$  is defined as the middle point of  $\vec{w}_c$ , called the point of closest approach (PCA) and it is calculated as:

$$\vec{s}\vec{v} = \vec{Q}_0 + t_c \vec{v} + 0.5 \vec{w}_c. \quad (\text{B.9})$$

## Appendix C      Calculation of Distance from a Point to a Trajectory

Consider a particle trajectory represented by a straight line in three-dimensional space with position vector  $\vec{a}$  and direction vector  $\vec{v}$  and let  $\vec{p}$  be the position vector of an arbitrary point in space. We want to compute the distance from the point  $\vec{p}$  to the line. Let us call  $\theta$  the angle between  $\vec{v}$  and  $\vec{p} - \vec{a}$ . Fig. C.1 illustrates the situation. Thus, the formula for the distance is given by

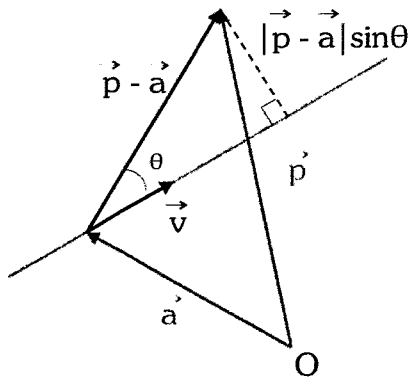


Figure C.1: Distance from a point O to a line.

$$s = \frac{|(\vec{p} - \vec{a}) \times \vec{v}|}{|\vec{v}|}. \quad (\text{C.1})$$

In the  $\Lambda$  analysis, the point O is the primary vertex and the line is the sum momentum vector of a  $p\pi^-$  combination.

# Bibliography

- [Abr64] M. Abramowitz and I. A. Stegun, *Handbook of Mathematical Functions*, Dover Publications, New York, 1964.
- [Afa02] S. V. Afanasiev et al., *Phys. Rev.* **C66** (2002), 054902.
- [Ahl98] L. Ahle et al., *Phys. Rev.* **C57** (1998), 466.
- [Ahl00] L. Ahle, *Phys. Lett.* **B476** (2000), 1.
- [Aic85] J. Aichelin and C. M. Ko, *Phys. Rev. Lett.* **55** (1985), 2661.
- [Alb02] S. Albergo et al., *Phys. Rev. Lett.* **88** (2002), 062301.
- [Alt06] C. Alt et al., To appear in the proceedings of 18th International Conference on Ultrarelativistic Nucleus-Nucleus Collisions: Quark Matter 2005, Budapest, Hungary (2006).
- [Ani84] M. Anikina et al., *Z. Phys.* **C25** (1984), 1.
- [Ant04] T. Anticic et al., *Phys. Rev. Lett.* **93** (2004), 022302.
- [Ave03] R. Aeverbeck et al., *Phys. Rev. Lett.* **68** (2003), 024903.
- [Bal04] A. Balanda et al., *Nucl. Instr. and Meth.* **A531** (2004), 445.
- [Bar03] H. W. Barz and L. Naumann, *Phys. Rev.* **C68** (2003), 041901.
- [Bar06] H. W. Barz, Private communication (2006).
- [Bas98] S. A. Bass et al., *Prog. Part. Nucl. Phys.* **41** (1998), 225.
- [Bec01] F. Becattini, J. Cleymans, A. Keranen, E. Suhonen and K. Redlich, *Phys. Rev.* **C64** (2001), 024901.
- [Ber01] E. Berdermann et al., Proc. of the 7th Int. Conf. on New Diamond Science Technology, Diamond and Related Materials, Hong Kong **10** (2001), 1770.
- [Blu93] W. Blum and L. Rolandi, *Particle detection with drift chambers*, Springer Verlag Berlin, 1993.
- [Bor78] A. Borghesi et al., *Nucl. Instr. and Meth.* **A153** (1978), 379.

- [Bou94] R. Bouclier et al., Nucl. Instr. and Meth. **A350** (1994), 464.
- [Bra95] P. Braun-Munzinger, J. Stachel, J. P. Wessels and N. Xu, Phys. Lett. **B344** (1995), 43.
- [Bra96] P. Braun-Munzinger, J. Stachel, J. P. Wessels, N. Xu, Phys. Lett. **B365** (1996), 1.
- [Bra98] P. Braun-Munzinger and J. Stachel, Nucl. Phys. **A638** (1998), 3.
- [Bra99] P. Braun-Munzinger, I. Heppe and J. Stachel, Phys. Lett. **B465** (1999), 15.
- [Bra00] E. L. Bratkovskaya et al., Nucl. Phys. **A675** (2000), 661.
- [Bra02] P. Braun-Munzinger and J. Stachel, J. Phys. **G28** (2002), 1971.
- [Bre99] T. Bretz, *Magnetfeldeigenschaften des Spektrometers HADES*, Technische Universität München, 1999, Diploma thesis.
- [Bug81] L. Bugge and J. Myrheim, Nucl. Instr. and Meth. **179** (1981), 365.
- [Bur73] K. B. Burns et al., Nucl. Instr. and Meth. **A106** (1973), 171.
- [Böh99] M. Böhmer, *Das Auslesesystem für den Ringabbildenden Cherenkov detektor im HADES Spektrometer*, Technische Universität München, 1999, Diploma thesis.
- [Car88] D. Carlsmith et al., Nucl. Instr. and Meth. **A364** (1988), 550.
- [Cav75] M. Cavalli-Sforza et al., Nucl. Instr. and Meth. **A124** (1975), 73.
- [Che37] P. A. Cherenkov, Phys. Rev. **52** (1937), 378.
- [Chu99] P. Chung, J. Phys. G: Nucl. Part. Phys. **25** (1999), 255.
- [Chu02] P. Chung, J. Phys. **G28** (2002), 1567.
- [Cle02] J. Cleymans, J. Phys. **G28** (2002), 1575.
- [Cle05] J. Cleymans, H. Oeschler, K. Redlich and S. Wheaton, Phys. Lett. **B615** (2005), 50.
- [Cro00] P. Crochet et al., Phys. Lett. **B486** (2000), 6.
- [Dev02] A. Devismes, J. Phys. **G28** (2002), 1591.
- [Día03] D. G. Díaz, *Preliminary result for an RPC prototype in HADES*, Kollaborationstreffen XII, GSI, Darmstadt, 2003.
- [Dur95] L.S. Durkin et al., IEEE Trans. Nucl. Sci. **42**, No. 4 (1995).
- [Ebe05] T. Eberl et al., Nucl. Phys. **A752** (2005), 433.

- [Fei04] E. D. Feigelson et al., *Astrophys. J.* **611** (2004), 1107.
- [Fon01] P. Fonte, *Nucl. Instr. and Meth. A* (2001), no. 478, 170.
- [För03] A. Förster et al., *Phys. Lett.* **B91** (2003), 152301.
- [Gar98] C. Garabatos et al., *Nucl. Instr. and Meth.* **A412** (1998), 38.
- [Gar00] Garfield, Simulation of gaseous detectors, <http://www.cern.ch/garfield>, 2000.
- [Gas85] A. P. Gasparyan, *Prog. Part. Nucl. Phys.* **53** (1985), 149.
- [Gaz96] M. Gazdzicki and D. Röhrich, *Z. Phys.* **C71** (1996), 55.
- [Gaz04] M. Gazdzicki, *J. Phys. G: Nucl. Part. Phys.* **30** (2004), S701.
- [Gea04] GEANT, <http://consult.cern.ch/writeup/geant>, 2004.
- [Gel68] M. Gell-Mann, R. J. Oakes and B. Renner, *Phys. Rev.* **175** (1968), 2195.
- [Gle85] N. K. Glendenning, *Astrophys. J.* **293** (1985), 1470.
- [God02] A. Godi et al., *Nucl. Instr. and Meth.* **A494** (2002), 14.
- [Har81] J. W. Harris et al., *Phys. Rev. Lett.* **47** (1981), 229.
- [Her04] N. Herrmann and K. Wisniewski, *Acta Phys. Polon.* **B35** (2004), 1091.
- [Hyd04] HYDRA, Dedicated HADES analysis software package; <http://www-hades.gsi.de/docs/hydra/classDocumentation/dev/ClassIndex.html>, 2004.
- [Jin94] X. Jin and R. J. Furnstahl, *Phys. Rev.* **C49** (1994), 1190.
- [Jus98] M. Justice et al., *Phys. Lett.* **B440** (1998), 12.
- [Kan04] K. Kanaki et al., *IEEE Trans. Nucl. Sci.* **51** (2004), 939.
- [Kla03] J. L. Klay et al., *Phys. Rev.* **C68** (2003), 054905.
- [Kot06] R. Kotte, Private communication (2006).
- [Kow04] P. Kowina et al., *Eur. Phys. J.* **A22** (2004), 293.
- [Lam02] M. A. C. Lamont, *J. Phys.* **G28** (2002), 1721.
- [Lau99] F. Laue et al., *Phys. Rev. Lett.* **82** (1999), 1640.
- [Leh99] J. Lehnert et al., *Nucl. Instr. and Meth.* **A433** (1999), 268.

- [Leh00] J. Lehnert, *Echtzeit-Mustererkennung zum Elektronennachweis mit einem RICH-Detektor in relativistischen Schwerionenkollisionen*, Ph.D. thesis, Justus-Liebig-Universität Gießen, 2000.
- [Leh03] J. Lehnert et al., Nucl. Instr. and Meth. **A502** (2003), 261.
- [Lin01] E. Lins, *Entwicklung eines Auslese- und Triggersystems zur Leptonenidentifizierung mit dem HADES-Flugzeitdetektor*, Ph.D. thesis, Justus-Liebig-Universität Gießen, 2001.
- [Lip00] C. Lippmann, *Aufbau und Inbetriebnahme eines Gasqualitätsmonitors für die HADES-Driftkammern*, Johann Wolfgang Goethe-Universität, 2000, Diploma thesis.
- [Lop04] X. Lopez, Prog. Part. Nucl. Phys. **53** (2004), 149.
- [Lut92] M. Lutz, S. Klimt, W. Weise, Nucl. Phys. **A542** (1992), 521.
- [Mao91] D. Maoz et al., Astrophys. J. Lett. (1991), IASSNS-AST-91-52.
- [Men00] M. Menzel et al., Phys. Lett. **B495** (2000), 26.
- [Mer04] M. Merschmeyer, *Production and Flow of Neutral Strange Particles in Ni+Ni collisions at 1.93 AGeV*, Ph.D. thesis, Ruprecht-Karls Universität, Heidelberg, 2004.
- [Mer05] M. Merschmeyer, J. Phys. **G31** (2005), S1147.
- [Mou06] J. Mousa, Private communication (2006).
- [Odz98] V. B. Odzhaev, I. P. Kozlov, V. N. Popok, D. V. Sviridov, *Ion implantation of polymers*, Belgosuniversitet Minsk, 1998, page 197.
- [Ope01] Vector Fields Opera, 2001, Commercial program for electromagnetic design.
- [PDG] Particle Data Group Booklet, 2006.
- [Pet00] M. Petri, *Entwicklung eines kombinierten Auslese- und Echtzeit-Triggersystems zum Nachweis von Elektronen/Positronen-Signaturen in einem elektromagnetischen Schauerdetektor*, Ph.D. thesis, Justus Liebig-Universität Gießen, 2000.
- [Pie05] W. Pietsch, M. Freyberg and F. Haberl, Astron. Astrophys. **434** (2005), 483.
- [Pin02] C. Pinkenburg et al., Nucl. Phys. **A698** (2002), 495.
- [Plu04] PLUTO, Pluto++, A Monte Carlo simulation tool for hadronic physics; <http://www-hades.gsi.de/computing/pluto/html/PlutoIndex.html>, 2004.

- 
- [Por97] R. Porter et al., *Phys. Rev. Lett.* **79** (1997), 1229.
- [pro01] HADES proposal, [http://www-hades.gsi.de/internal/May2001/proposal\\_fin.pdf](http://www-hades.gsi.de/internal/May2001/proposal_fin.pdf).
- [Prz06] W. Przygoda et al., *Acta Phys. Polon.* **B37** (2006), 139.
- [Rap00] R. Rapp and J. Wambach, *Adv. Nucl. Phys.* **25** (2000), 1.
- [Rus06] A. Rustamov, *Exclusive  $\eta$  meson reconstruction in pp collisions with the HADES spectrometer*, Ph.D. thesis, Technische Universität Darmstadt, 2006.
- [Sad06] A. Sadovsky, *Investigation of charged kaon production in C+C collisions at 2 AGeV*, Ph.D. thesis, Technische Universität Dresden, 2006.
- [San03] M. Sanchez-García, *Momentum reconstruction and pion production analysis in the HADES spectrometer at GSI*, Ph.D. thesis, Universidade de Santiago de Compostela, 2003.
- [Sau77] F. Sauli, *Principles of Operation of Multiwire Proportional and Drift Chambers*, 1977.
- [Sen99] P. Senger and H. Ströbele, *J. Phys. G: Nucl. Phys. Part.* **25** (1999), R59.
- [Sew99] S. Sewerin et al., *Phys. Rev. Lett.* **83** (1999), 682.
- [Sho00] *HADES Shower Homepage*, <http://zjf-www.if.uj.edu.pl/psj/hades-doc>, 2000.
- [Sim05] F. Simon, *J. Phys.* **G31** (2005), S1065.
- [Ste80] R. Stephenson et al., *Nucl. Instr. and Meth.* **A171** (1980), 337.
- [Stu01] C. Sturm et al., *Phys. Rev. Lett.* **86** (2001), 39.
- [Stö86] H. Stöcker and W. Greiner, *Phys. Rept.* **137** (1986), 277.
- [Tak05] J. Takahashi, *J. Phys.* **G31** (2005), S1061.
- [Tlu06] P. Tlustý, Private communication (2006).
- [TOF00] *HADES TOF Homepage*, <http://pfmac.lns.infn.it/~hades/index.html>, 2000.
- [Toi03] A. Toia et al., *Nucl. Instr. and Meth.* **A502** (2003), 270.
- [Toi04] A. Toia, *Performance of the HADES Spectrometer for Dilepton Identification in the Reaction C+C at 1-2 AGeV*, Ph.D. thesis, Justus Liebig-Universität Gießen, 2004.

- [Tra01] M. Traxler, *Real-Time Dilepton Selection for the HADES Spectrometer*, Ph.D. thesis, Justus Liebig-Universität Gießen, 2001.
- [Van05] G. Van Buren, *J. Phys.* **G31** (2005), S1127.
- [Vau04] S. Vaughan et al., *Mon. Not. Roy. Astron. Soc.* **351** (2004), 193.
- [Web01] F. Weber, *J. Phys.* **G27** (2001), 465.
- [Web06a] F. Weber, A. Hogueiros, R.P. Nogueiros and P. Rosenfield, *Proceedings of International Workshop on Astronomy and Relativistic Astrophysics (IWARA), Natal, Brazil (2006)*, e-Print Archive : astro-ph/0604422.
- [Web06b] F. Weber, A. Torres i Cuadrat, A. Ho and P. Rosenfield, *PoS JHW2005* (2006), 18, e-Print Archive : astro-ph/0602047.
- [Whe] S. Wheaton and J. Cleymans, *THERMUS – A Thermal Model Package for ROOT*, hep-ph/0407174.
- [Wis00] K. Wisniewski et al., *Eur. Phys. J.* **A625** (2000), 515.
- [Wro85] A. Wroblewski, *Acta Phys. Pol.* **B16** (1985), 379.
- [Wüs05] J. Wüstenfeld, *Auslese und Qualitätskontrolle der HADES-Driftkammern*, Ph.D. thesis, Johann Wolfgang Goethe-Universität Frankfurt a.M., 2005.
- [Yag02] N. Yagisawa, T. Hatsuda and A. Hayashigaki, *Nucl. Phys.* **A699** (2002), 665.
- [Zei99] K. Zeitelhack et al., *Nucl. Instr. and Meth.* **A433** (1999), 201.
- [Zsc02] S. Zschocke, B. Kämpfer and O. Pavlenko, *Proceedings of XL International Winter Meeting on Nuclear Physics, Bormio, Italy (2002)*.
- [Zum05] P. Zumbruch, *Untersuchung zur Produktion von Pionen und Pion-Pion-Korrelationen in C+C Reaktionen am HADES-Detektor bei einer Strahlenergie von 2 GeV pro Nukleon*, Ph.D. thesis, Technische Universität Darmstadt, 2005.

# Acknowledgements

I would like to thank my advisor Prof. Dr. E. Grosse for giving me the opportunity to accomplish a work of such a scale by offering me a position in the Institute of Nuclear and Hadronic Physics of Forschungszentrum Rossendorf. I would also like to thank my group leader Prof. Dr. B. Kämpfer for his useful advice, suggestions and comments assisting my effort, as well as for his critical view on the painful process of writing my thesis.

Special thanks go to my colleague Dr. L. Naumann for his patient supervision of my hardware work, for promoting me scientifically, for his thoughtfulness concerning my first-authorship publication and his critical comments on my manuscript. At this point I should also acknowledge the help of all the people in the FZR detector lab, in particular Dipl.-Ing. M. Sobiella and J. Hutsch, for introducing me to the challenging procedure of constructing a large scale drift chamber.

Special thanks also go to my colleague Dr. R. Kotte for his invaluable assistance with the  $\Lambda$  analysis, for patiently listening, quickly understanding my problems and placing his experience at my disposal.

Lots of thanks are for my closest colleague, Dipl.-Phys. A. Sadovsky for supporting my first steps in setting up the frame of my analysis and helping me improve my understanding of programming.

I am greatly indebted to Dr. J. Markert. Without his assistance and motivation the technical part of the analysis would not have come to an end.

Moreover I would like to acknowledge the Munich group for allowing me to work on their cluster, in particular Dr. T. Eberl for helping me write my first reconstructor. Thanks to the Cyprus group for their cluster too and to Dr. J. Mousa for his quick response to my requests.

There have been a lot of other people that assisted me over the past years. In random order these people are Dr. L. Fabbietti, Dr. P. Zumbruch., Dr. J. Bielik, M. Sudol, Dr. J. Wüstenfeld, Dr. habil. F. Dohrmann, Dr. J. Otwinowski, Dr. M. Jaskula, Dr. R. Holzmann, B. Bannier, Dr. C. Müntz, Dr. C. Sturm, Dr. H. Agakichiev, Dr. C. Garabatos, Dr. H.-W. Barz, Dr. S. Zschocke, Dr. R. Dressler, K. Heidel.

Ευχαριστώ τους γονείς μου για την υπομονή και τη διακριτικότητα που έδειξαν όλα αυτά τα χρόνια που είμαι μακριά τους, παρά το ότι το όλο επιχείρημα κόστισε περισσότερο χρόνο και νεύρα από ό,τι υπολόγιζα, τις υπέροχες φίλες μου στην Αθήνα που με τα μηνύματά τους και αρκετές φορές τις επισκέψεις τους μου κράτησαν συντροφιά και μου θύμιζαν την πατρίδα μου, καθώς και τους υπέροχους φίλους που απέκτησα στην Ευρώπη και που μετέτρεψαν την διαμονή μου στο εξωτερικό σε μια αξέχαστη εμπειρία.